UNIVERSITY OF OKLAHOMA

GRADUATE COLLEGE

A MICROSCOPIC CHARACTERIZATION OF WETTABILITY IN SHALE KEROGEN WITH VARYING MATURITY LEVELS AND ITS ROLE IN GOVERNING FLUID DISTRIBUTION

A DISSERTATION

SUBMITTED TO THE GRADUATE FACULTY

in partial fulfillment of the requirements for the

Degree of

DOCTOR OF PHILOSOPHY

By

YINAN HU
Norman, Oklahoma
2014

A MICROSCOPIC CHARACTERIZATION OF WETTABILITY IN SHALE KEROGEN WITH VARYING MATURITY LEVELS AND ITS ROLE IN GOVERNING FLUID DISTRIBUTION

A DISSERTATION APPROVED FOR THE
MEWBOURNE SCHOOL OF PETROLEUM AND GEOLOGICAL ENGINEERING

BY

_____
Dr. Deepak Devegowda, Chair

_____
Dr. Faruk Civan

_____
Dr. Chandra S. Rai

_____
Dr. Ahmad Jamili

_____
Dr. Takumi Hawa

This work is dedicated to my parents, Huifang Ying and Wen Hu. They have been my inspiration to continue learning. Their constant source of love, understanding, and patience have given me the drive and strength to overcome all challenges. I love you Mom and Dad.

ACKNOWLEDGEMENTS

Foremost, I would like to express my gratitude to Dr. Deepak Devegowda, under whose supervision I chose this topic and began the thesis. Thanks for the constant encouragement and the academic freedom that he gave to me during the resesarch. His guidance helped me in all the time of research. Without his guidance and perseverance, it would have been impossible to investigate the topic to its present stage.

Besides, I would like to thank Dr. Alberto Striolo and his students, Anh Phan, Tuan Ho and Thu Le. They all taught me how to simulate, and provided tremendous help and technical advices for this research.

In addition, I also want to thank Dr. Faruk Civan and Dr. Richard Sigal. I thank them for their knowledge and wisdom in regards to shale gas research. This research would not be where it is today without their expertise. Also, I would like to thank the rest of my thesis committee: Dr. Chandra S. Rai, Dr. Ahmad Jamili and Dr. Takumi Hawa for their insightful comments.

The simulation work in this research was conducted with the Oklahoma Supercomputer Center for Education and Research (OSCER). I appreciate their great computing support of this research.

Lastly, I would like to thank my whole families and friends. They have been with me every step of the way, through good and bad times.

TABLE OF CONTENTS

LIST OF TABLES

LIST OF FIGURES

ABSTRACT

Kerogen is defined as the insoluble macromolecular organic matter in sedimentary rocks and is a complex mixture of organic chemical compounds. The process of kerogen maturation is accompanied by the loss of functionalized molecules, leading to a decreased H/C and O/C ratios, as well as a reduction in molecular weight. The degree of thermal maturation is often expressed by the van Krevelen diagram with H/C and O/C ratios as indicators. Even though kerogen pores are widely viewed as hydrocarbon-wetting, some recent experimental work indicates the existence of water in kerogen. It then becomes necessary to evaluate the wettability characteristics of kerogen and to determine the governing factors controlling kerogen pore surface wettability.

Addressing these concerns is very essential because wettability is directly related to the dynamics of fluids and is likely to be extremely relevant to developing models for reserves estimates and multiphase flow. Additionally it may provide some answers to the common observation of low recovery of hydraulic fracture water.

In this study, pore-scale molecular dynamics simulations are used to understand the relationships between kerogen maturity and its wettability. The modeling approach adopted here includes a proper description of the kerogen pore systems with differing levels of thermal maturity, surface roughness, tortuous paths, and porous nature. Three kerogen models, namely activated kerogen, kerogen free of activated sites and the graphite slit pore are considered in this study. This work examines the sensitivity of the storage of pure water, brine water and a mixture of water and hydrocarbon to pore size, degree of kerogen maturity and pore wall roughness. A quantitative analysis to discuss the dependence of kerogen wettability on maturity degree is also presented.

The results indicate that the kerogen models constructed in this study more accurately represent organic pores in comparison to widely used planar graphite slit-pore systems. Confinement of water in kerogen pores is shown to lead to water entrapment and phase changes of water in comparison to its bulk properties. Fluid adsorption on the kerogen surface is observed to be multi-layer, instead of monolayer assumed in the Langmuir adsorption theory. Lastly, the results demonstrate that kerogen maturity governs wettability of organic kerogen pores. Kerogen of intermediate maturity is shown to be characterized by heterogeneous wettability and may lead to trapping of water in organic pores.

CHAPTER 1

INTRODUCTION

This chapter provides an introduction and a literature review of topics related to shale characterization, petrophysical characterization and modeling including hydraulic fracturing, the microstructure of shales, shale gas-in-place estimates and the evaluation of kerogen.

According to an assessment published by the US Energy Information Administration (EIA) in 2013, shale plays have contributed to a growth in world oil reserves by 11% and in gas reserves by 47%. In the United States, organic-rich shale plays are vital to domestic energy supply and currently constitute the most productive oil and gas fields. From 2000 to 2012, shale oil output increased from 0.2 million barrels per day (MMbbl/d) to nearly 2 MMbbl/d, while shale gas production increased from just 0.3 trillion cubic feet (Tcf) to 9.6 Tcf (EIA 2013). The main portion of the shale production in the US is confined to major shale formations of Bakken and Eagle Ford (oil), Barnett, Haynesville, Marcellus (gas).

Current hydrocarbon storage for shale gas-in-place estimates involves the quantification of free, adsorbed, and solution gas quantities stored in micro- and nano-scale pores. (Ambrose 2011). Even though shale formations possess extremely low permeability, technology development in the areas of horizontal well drilling and hydraulic fracturing has enabled economic production and promoted the tremendous growth in shale development activity.

However, there are several issues that remain poorly understood. These include the poor recovery of hydraulic fracture water during well clean-up and kerogen pore wettability and the role of thermal maturity of kerogen in governing kerogen wettability. The purpose of this thesis is to utilize molecular dynamics simulation method to characterize the wettability in shale kerogen as and study the role of the organic matter in governing fluid dynamics. As a fundamental work, the study could possibly provide some insight into the low recovery issue of hydraulic fracture fluid, hydrocarbon in-place estimation and water entrapment and storage in shales.

1.1 Issues in Hydraulic Fracture Treatment

Hydraulic fracturing to stimulate shale wells is routinely employed to enable increased contact with larger reservoir volumes. This technique promotes shale well deliverability by creating a fissure network for hydrocarbons to flow from the reservoir to the well. The creation of hydraulic fractures is accomplished by injecting high pressure fracturing fluids in to the well and through selected perforations in to the formation. For shale wells, these fluids are predominantly fresh water treated with viscosity reducers and with low proppant concentrations. The use of water-based fracturing treatments for shale wells is driven by the low cost and its ability to create larger and more complex fractures (Warpinski et al. 2005, Cipolla et al. 2009), and the potential for less formation damage and easier cleanup (Schein 2005, Palisch et al. 2008).

In practice, there are several interesting and common phenomena observed during fluid flowback. In general, only a small portion of the hydraulic fracture water is recovered during the cleanup phase, although several million gallons of fluids are pumped

into the reservoir. King (2012) shows that this small portion may range from as little as 5% of the water volume used to fracture the rock in Haynesville shale to as much as 50% in the Barnett and Marcellus shales. A very large quantity of water is therefore retained in the reservoir. Additionally, although the make-up of the fracturing fluid is largely fresh water, flowback water shows a high concentration of soluble chloride salts. Especially at later times, the salt concentration can be as high as 80,000 to 100,000 ppm (King 2010) and raises concerns regarding the source of the salt and creates challenges for produced water disposal.

The mechanisms behind these observations are poorly understood. Several theories have been proposed to account for these field phenomena. Depending on the salinity, dessicated clay minerals have been known to adsorb substantial amounts of water that may remain irrecoverable (King 2012). King (2012) also report that induced micro-cracks may trap some water following the release of pressure on the well, while capillary trapping in inorganic pores may also account for some loss of fracture water. The presence of high capillary forces (Sondhi 2011) and heterogeneous wettability characteristics of shales (Elijah 2011) may lead to counter-current imbibition of water when shales are exposed to hydraulic fractured water (Qin 2007). However, these theories lack experimental evidence, and we still do not fully understand the physiochemical process behind these observations. A full understanding of the underlying production mechanisms requires joint efforts from geomechanics and petrophysics, modeling of transport and storage, completions design and drilling.

1. 2 The Microstructure of Shale

Understanding the microstructure of shales is critical to determine gas/oil-in-place estimation and the related storage and transportation mechanisms. Shale formation is made up of inorganic and organic materials. Shale permeability is associated with inorganic matrix where relatively larger pores and fractures exist. The organic material, known as kerogen, is finely dispersed within the inorganic matrix and molecular phenomena such as adsorption occurs within the kerogen (Akkutlu et al. 2011).

Heterogeneity and nano-scale pores are typically found in shale samples. Recent developments of improved imaging techniques employing focused ion beam-Scanning Electron Microscopy (SEM) methods (Curtis et al. 2011, Chalmers et al. 2012) provide visual analysis of the shale microstructure. These indicate that shales are highly heterogeneous and depending on the geological formation, pore volumes may be associated with either the inorganic matrix in plays such as the Haynesville shale or within kerogen material such as Barnett, Woodford, Eagle Ford, Marcellus etc. (Curtis et al. 2010). Other experimental approaches based on Mercury Injection Capillary Pressure (MICP) experiments (Sondergeld et al. 2010) report pore sizes in the order of 2-10 nm for the Barnett shale.

With an even higher resolution than the SEM, Scanning Transmission Electron Microscopy (STEM) technique is able to image the internal structure of kerogen and capture some observations that are not able to be seen using SEM. The study from Curtis et al. (2011) revealed the presence of complex pore networks, sponge-like internal structure, and the existence of large surface areas for adsorptive storage. Figure 1.1 is a STEM image from Curtis et al. (2011) in which pores as small as 2-3 nm in diameter were

observed in the image. At this magnification, the variation in gray scale provided hints of connectivity in the internal structure of kerogen. Such high degree of complexity of shale microstructures and the internal pore structure can potentially have a significant impact as observed in the significant variations in the overall gas storage and permeability estimates in shale.

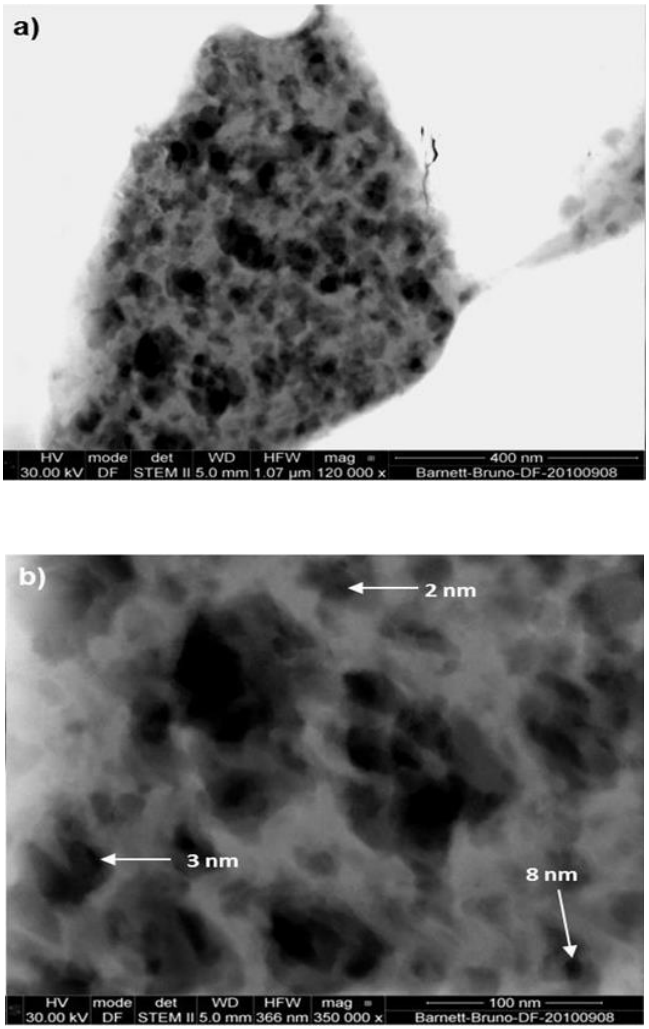

Figure 1.1: a) STEM image of kerogen from the Barnett shale samples. b) Higher magnification image of the porosity in the kerogen revealing some pore diameters (Curtis et al. 2011)

In addition to the presence of heterogeneity and complex pore systems, the wetting characteristics of shales are also critical to quantifying hydrocarbon recovery, estimating the distribution of hydrocarbons and understanding the fate of hydraulic fracture water. Because these shales comprise of organic-rich sediments that were deposited in water-based environments such as deep water marine, lacustrine and deltaic systems, it is likely that shales may have been water-wet initially. Under sufficient overburden and temperature changes leading to thermal maturity, hydrocarbon products are generated, expelled, migrated and/or trapped. These changes may lead to changes in wettability of shales. However, it is possible that water may be present in the organic material of shales.

The accepted view of shale wettability is that the organic pores are hydrocarbon-wetting and the inorganic pore systems are hydrophilic (Elijah 2011). However, the view of kerogen pores being hydrophobic (Passey et al. 2010) is being challenged by some recent studies that provide evidence of the existence of water in kerogen material (Chalmers and Bustin 2010, Ruppert et al. 2013). Chalmers and Bustin (2010) detected moisture contents ranging from 0.5 to 15% at 6 MPa for a suite of organic-rich shales including Devonian, Jurassic, and Cretaceous shales from northeastern British Columbia. By comparing a suite of moisture-equilibrated shales, they also pointed out that the effect of moisture on methane storage capacity is likely to be a function of the distribution of hydrophobic and hydrophilic sorption sites throughout the pore network. Ruppert et al. (2013) combined Small-Angle Neutron Scattering (SANS) and Ultra-Small-Angle Neutron Scattering (USANS) to study the accessibility of pores to methane and water in Barnett Shale samples. In their study, a large percentage of the pores were associated with

the organic components. Their results indicate that most pores were accessible to both water and methane over a wide size range (10 nm to 10 μm) and surprisingly the fine pores (<30 nm) appeared to be much more accessible to water than methane. These recent results demonstrate the need for careful consideration of the heterogeneous wettability of shales and kerogen pore systems.

1.3 Gas-in-place Estimation and Pore Confinement Effect

In the volumetric method, shale gas-in-place calculation involves the quantification of free, physically adsorbed, and dissolved gas quantities (Ambrose 2011). The free gas is usually stored in the inorganic pores and large organic pores. Adsorption is a surface phenomenon and physically occurs on large internal surface area of the kerogen. Dissolved gas may be present in the formation water and the amount of dissolved gas in formation water is not generally considered important (Diaz-Campos 2010).

With pore sizes in nanometer scales in shale formations and with kerogen possessing a major portion of total porosity (Passey et al. 2010), the volumetric equation for the free gas amount calculations required corrections to consider the loss of the pore volume taken up by the adsorbed molecules (Ambrose 2011). Recent studies have demonstrated the important role that adsorbed gas plays in total gas-in-place estimates and have motivated the need for modified gas transportation models (Xiong et al. 2012, Fathi et al. 2012).

The amount of adsorbed gas is also significantly impacted by pore confinement effect. Diaz-Campos (2010) found that gas adsorption and solubility in liquid are enhanced due to dominant pore wall effects. Additionally, critical properties of the fluid

confined to small pores were founded to be influenced by the pore size as well (Sapmanee 2011, Devegowda et al. 2012, Didar 2012; Firincioglu 2013, Travalloni et al. 2013).

In summary, adsorption plays an important role in total storage, and the effect of pore confinement on the adsorption amount and the phase behavior is significant. Combination of these effects can have a potentially significant impact on the storage, transportation, and production of hydrocarbons in shale reservoirs.

1.4. Kerogen Maturation

Kerogen is insoluble macromolecular organic matter and it accounts for the most abundant sedimentary organic matter on Earth. It is known to have the capability of generating hydrocarbons (Rullkötter and Michaelis 1990). Kerogen forms under sufficient geothermal pressures and with geologic time primarily from animal matter (Vandenbroucke et al. 2007). During this continuous evolution, the chemical structure and composition of source rock kerogen change and serves as an indicator of rock maturity. The source of kerogen is responsible for its diverse chemical composition and as such, no single chemical formula can adequately represent these complex organic compounds (Facelli et al. 2011).

As kerogen evolves during maturation, hydrocarbons and functionalized molecules are lost that results in reduction in H/C and O/C atomic ratios and a decrease in molecular weight. The classic van Krevelen diagram (provided in Figure 1.2) effectively illustrates the changes of these ratios and classifies three kerogen types based on the maturation (Vandenbroucke et al. 1993 and Tissot and Welte 1978). The highest yield of oil is associated with kerogen type I (the Green River Oil Shale) with H/C ratio

more than 1.5 and O/C ratio varies from 0.03 to 0.1 depending on the maturity, while type III typically generates gas with a lower H/C (less than 0.8) and a wider O/C range (from 0.03 to 0.3) (Vandenbroucke et al. 2007). For Type II kerogen from Paris Basin Toarcian, Behar and Vandenbroucke (1987) showed that the atomic H/C and O/C ratios were 1.34 and 0.196 respectively at the beginning of diagenesis. These values decreased to a H/C ratio of 1.25 and an O/C ratio 0.089 when catagenesis began and were further reduced to H/C ratio of 0.73 and O/C ratio of 0.026 at the end of catagenesis.

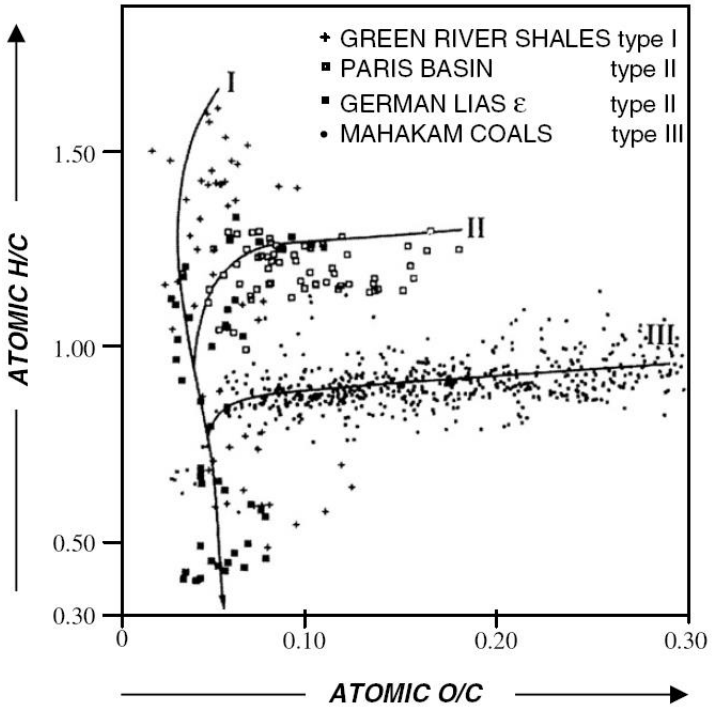

Figure 1.2: The Classic Van Krevelen diagram showing kerogen maturation path associated with different types of kerogen (Vandenbroucke et al 1993 and Tissot and Welte 1978)

Geochemists can evaluate the elemental ratios of H/C and O/C by monitoring the petroleum compounds of source rock released at high temperature. In source rock assessment, Rock Eval pyrolysis technique is an industry standard where a small crushed

kerogen sample is combusted during a programmed temperature heating in an inert atmosphere of helium or nitrogen (McCarthy et al. 2011). This method quantifies the amount of free hydrocarbons in the sample, and the amount of generated hydrocarbons and CO_2 volatilized through thermal cracking. These values reflect the potential of the rock to produce hydrocarbon, and are further used to determine the Hydrogen Index (HI) and the Oxygen Index (OI) which are derived from the ratio of hydrogen to TOC and ratio of CO_2 to TOC respectively. The indices of HI and OI are proportional to the amount of hydrogen and oxygen contained in the kerogen.

In addition to HI and OI indices, Rock Eval pyrolysis also produce a Tmax peak, a pyrolysis oven temperature at which the maximum generation of hydrocarbons is reached during the cracking of the kerogen. The value of Tmax depends on the kerogen type and it is also used a maturity indicator. A higher Tmax means more mature kerogen. Rock Eval pyrolysis technique also determines the production index (PI) which is a ratio of already generated hydrocarbon to potential hydrocarbon. Because some degradable components in kerogen are further converted to free hydrocarbon as kerogen becomes mature, PI increases with kerogen maturation before hydrocarbon expulsion (McCarthy et al. 2011). The method of Rock-Eval is not recommended for kerogen of hydrogen poor and oxygen rich, such as coal, due to incomplete combustion of some refractory organic matter (Crain 2010).

Vitrinite reflectance is another key diagonostic technique indicative of the rock's thermal maturity. This evaluation method measures the amount of light reflected by vitrinite in the source rock and is expressed as the percentage of reflectance in oil, Ro. The value of Ro depends on kerogen type and increases with thermal maturity. Vitrinite

reflectance is widely used as indicators of thermal maturity, especially in shale, and is also used to rank coals. However this technique is not suitable to measure rocks that lack vitrinite. A combined use of different techniques helps refine kerogen type and access maturity, for example plotting Tmax versus HI, HI versus Ro or depth plots of Ro and Tmax.

1.5 Kerogen Modeling

The diverse chemical compositions associated with kerogen are of a consequence of the maturation process and are a function of the source, maturation time, and geologic processes in achieving the final state of the rock. As a result, kerogen has a complex structure, as can be seen from the STEM image in Figure 1.1. Atomic modeling of kerogen is a topic that researchers are always pursuing. Traditionally, the model chosen as a proxy for organic pore systems is the graphene slit pore model with the purpose of determining thermodynamic properties of adsorbed fluids in porous kerogen (Striolo 2003, Severson and Snurr 2007, Diaz-Campos 2010, Didar 2012). Very recently, Liu and Wilcox (2012) considered functional groups positioned on the surface layers of graphite slabs and investigated the influence of these groups on CO_2 adsorption.

Although very informative, graphene slit pore models are deficient in addressing the known complexities of kerogen and their impact on fluid behavior (Hu et al. 2013a, 2013b, 2013c, 2014a, 2014b). Some of these complexities include different surface chemistry components, surface roughness, tortuous paths and porous nature. In this thesis, I built simplified kerogen models that are closer structurally to kerogen in Figure 1.3 for the Green River kerogen (Facelli et al. 2011) than the graphitic slit pore model, with most

structural properties listed above taken into account. Although still an approximation to the real world, a dramatic differences in the distribution of fluid are observed when comparing the kerogen models with the ideal graphene slit model. It was clear that the surface morphology of the pores influenced the results greatly. Hence there is a need to move beyond planar graphene slit-pore systems towards more sophisticated pore systems in molecular dynamics simulations.

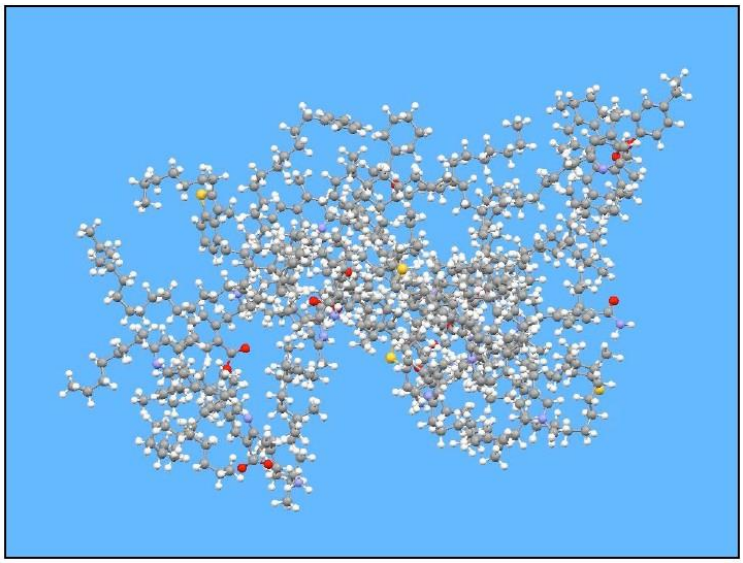

Figure 1.3: Green River kerogen Siskin model.
Colors: C - gray, O - red, N - blue, S -yellow, H - white (Facelli et al. 2011)

1.6 Purposes of the Study

Due to the nanometer-sized scale of shale pores, the extreme conditions of pressure and temperature at the reservoir, utilization of physical experiments to investigate quantifies of interest such as wettability becomes challenging. An alternative approach is to employ molecular dynamics simulations that essentially simulate physical movements of atoms

and molecules following the Newton's equations of motion to conduct virtual experiments.

This thesis uses the latter method to provide fundamental pore-level analyses of the physiochemical processes of fluid inside the shale pores. There are three objectives of this thesis.

1) The first one is to build an easily constructed but relatively realistic kerogen models. For this purpose, two kerogen models are demonstrated. One model, referred to as the activated kerogen model, contains several functional groups on the pore surface, while the other model, the inactive kerogen model contains only carbon. The activated and inactive kerogen models serve to represent a moderately mature kerogen and a highly mature kerogen pore system respectively.

2) The second objective is to study the influence of pore sizes, surface roughness and the degree of kerogen maturity on the behavior of fluid in organic nanopores. The considered fluid includes pure water, brine water with NaCl, and a mixture of water and alkane. By comparing the results of the kerogen models and the smooth graphene slit pores, the study underscores the need for accurate characterization of kerogen pore systems in terms of the pore morphology, level of surface activation and pore size. In addition, the results indicate that kerogen pore systems may create adequate conditions for water entrapment and the surface structure of kerogen could impact the adsorption characteristics traditionally modeled by the Langmuir monolayer adsorption theory.

3) The last goal is to understand the role of kerogen maturity on wettability of organic systems. The contact angle of water droplet and a binary mixture of water and alkane on surfaces with varying degrees of kerogen maturity are characterized. The

results demonstrate that maturity level controls the wettability of organic nanopores and for intermediate maturity such as in liquids-rich shales, organic pore systems may have heterogeneous-wet characteristics.

As a fundamental study, this work may provide some valuable insight into the low recovery of hydraulic fracture water, pore confinement effect on phase behavior, water storage and entrapment, wettability characterization in shale, and may further impact the parameterization of current shale hydrocarbon storage models (Ambrose 2011 and Sigal et al. 2013) and therefore our estimates of hydrocarbon-in-place.

This thesis is therefore organized as follows: The current chapter provides background information related to the theme of the thesis and reviews some of the relevant literature associated with shale microstructure, thermal maturity and wettability. Chapter 2 briefly introduces the molecular dynamics simulation approach. In Chapter 3, detailed modeling of shale kerogen is described. In this chapter, the advantages of the proposed models over the graphene slit pore model are also listed. Chapter 4 studies the surface wettability effect of kerogen, and the wettability is shown to be dependent on kerogen maturity level. Chapters 5 – 7 provide fluid dynamics and emphasize the effect of kerogen maturation in fluid distribution, considering pure water, brine water, and a mixture of water and alkane in the kerogen systems respectively. In addition, Chapter 6 studies the saline water distribution in the premature inorganic proxy as well and the comparison results in organic and inorganic pores could be insightful for the dynamics of hydraulic fracture water in shale nanopores. Lastly, Chapter 8 concludes this thesis and provides some recommendations for future research.

CHAPTER 2

MOLECULAR DYNAMICS SIMULATION APPROACH

Current simulation schemes and interpretation of laboratory experiments generally do not account for pore proximity effects in shale nanopores where strong inter-molecular

interactions become dominant. Consequently, limited-physics simulation and transport models although insightful may not be accurate enough for quantitative analyses. In this circumstance, molecular dynamics simulation is an alternative tool to investigate fluid behavior confined in nanoporous materials.

Molecular dynamics simulation approach is a mechanics based computer simulation method where atoms and molecules interact over a period of time following Newton's equations of motion. The method was originally conceived by theoretical physicist in the late 1950s (Alder and Wainwright, 1957). It becomes enormously popular in recent years due to the availability of high speed and large capacity computers. It is an excellent tool in science and engineering research to determine system structure and thermodynamic properties of large molecules and to examine the dynamics of atomic-level phenomena among several other applications. This computer simulation approach makes it possible to conduct virtual experiments where laboratory experiments are either costly and difficult or even unrealistic. The interested readers are referred to Striolo (2011) and Cole (2013) for details concerning the simulation protocol. This chapter summarizes the basic theory behind the molecular dynamics simulation and reviews the potential fields utilized in this study.

2.1 Basic Theory

Molecular dynamics simulation approach simulates atomic level movements caused by inter- and intra-molecular forces by integrating Newton’s equations of motion. It involves two basic steps: the determination of interacting forces using potential fields, and the tracing of molecular movements by solving Newton's equation of motion. The interacting

force applied on each atom is calculated from the gradient of the potential. The force acting on atom i is provided in Equation 1, where U_i is the potential energy and r_i is related to the atom's position.

$$F_i = -\frac{\partial U_i}{\partial r_i} \quad (1)$$

The second law of Newton describes the force with the rate of change of momentum (Equation 2), where m_i and a_i are the mass and the acceleration of atom i respectively. With Equation 1 and 2, we can determine the trajectory of the system for each time step.

$$F_i = m_i \frac{d^2 r_i}{dt^2} = m_i a_i \quad (2)$$

The possible states of a real system are classified in the corresponding statistical ensemble. In molecular dynamics, three classical types of ensembles are commonly used including the canonical (NVT) ensemble, the microcanonical (NVE) ensemble, and the isothermal-isobaric (NPT) ensemble. N, V, P, T, E represent the number of molecules, volume, pressure, temperature and energy in a system respectively.

1. Canonical (NVT) ensemble describes a system in contact with a heat bath and therefore maintains constant temperature, volume and the number of molecules.

2. Microcanonical (NVE) ensemble is an isolated thermodynamics system that fixes the number of molecules, the volume and the total energy. The total energy is a summation of kinetic energy, potential energy and internal energy.

3. Isothermal-isobaric (NPT) ensemble maintains constant pressure and temperature within a fixed number of molecules, while the volume is allowed to fluctuate.

During the simulation processes of NVT and NPT ensembles, controlling temperature and / or pressure is necessary. The system temperature is adjustable by

scaling the velocities of atoms using a thermostat such as Berendsen and Nosé-Hoover thermostats. Pressure control is usually achieved by changing the size of the simulation box with some most commonly used barostat including Berendsen and Parrinello-Rahman barostats etc.

Periodic boundary condition is usually applied in three dimensions to avoid problems caused by finite size, and make the system effectively infinite. The cubical simulation box is replicated in all simulated direction so that the whole space is fulfilled and the system has no edge. With the periodic boundary condition, we are able to calculate macroscopic properties from fewer particles.

The procedure of a classical molecular dynamics simulation is summarized in Figure 2.1. At initial step, molecules are positioned differently from their expected position with randomly assigned initial velocities. The force applied on each molecule is then calculated based on the potentials in the forcefield. During the simulation, velocities are rescaled by thermostat to achieve the desired temperature. Updated velocities and positions at the next time step are obtained according to numerical integration algorithms based on Equation 1 and 2. The loop in the flowchart is repeated at every time step until either the wanted number of iterations or the system equilibrium is reached. We then analyze the final trajectory of molecules to calculate properties.

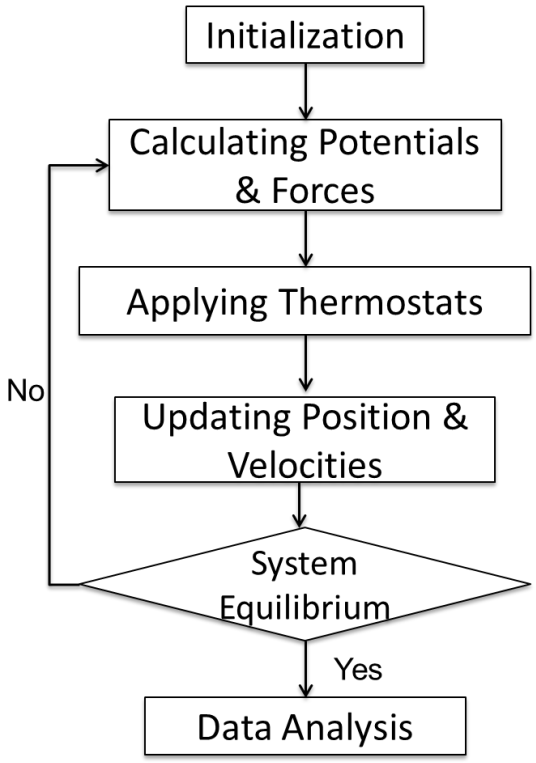

Figure 2.1: General flow chart for classical molecular dynamics simulations

2.2 Potential Fields

Potential fields describe the potential energy among interacting atoms. Parameters in potential fields are empirical and are usually derived from experiments and quantum mechanical calculations. A potential field includes nonbonded and bonded interaction and is expressed in Equation 3. U_{total}, U_{NB}, U_B are total energy, nonbonded energy and bonded energy respectively.

$$U_{total} = U_{NB} + U_B \quad (3)$$

Nonbonded interaction, usually referred to as intermolecular interaction, is energy of attraction or repulsion acting between neighboring particles. The components of nonbonded interaction can be further broken down into two groups including van der Waals and electrostatic potentials (Equation 4). The van der Waals forces are represented

by the 12-6 Lennard-Jones (LJ) potential shown in Equation 5 where the potential well depth, distance of zero intermolecular potential and the particle distance are expressed by ε, σ and r. Electrostatic potentials are generated due to unequal charge distribution over the atoms of a molecule, and they are proportional to partial charge. Coulomb's law calculates the electrostatic interaction and is described in Equation 6 where q_1, q_2 are partial charges, and ϵ_0 is the permittivity of free space.

$$U_{NB} = U_{VW} + U_{el} \tag{4}$$

$$U_{VW}(r) = 4\varepsilon\left[\left(\frac{\sigma}{r}\right)^{12} - \left(\frac{\sigma}{r}\right)^{6}\right] \tag{5}$$

$$U_{el}(r) = \frac{q_1 q_2}{4\pi\epsilon_0 r} \tag{6}$$

Bonded interaction is the energy that holds together the atoms making up a molecule and it is also named intramolecular interaction. There are three primary components of this interaction, as Equation 7 shows. Bond stretching describes a bond between two atoms. The bond energy is modeled based on Hooke's law in Equation 8 where k is the force constant and r0 is the reference bond length. Similar to bond energy, the bond angle bending is modeled with a harmonic potential $u_{angle}(\theta)$, shown in equation 9, where θ, θ_0 and k_θ are the current bond angle, equilibrium bond angle and force constant respectively. Dihedral angle potential involves four atomic positions and it describes the interaction caused by torsional forces in a molecule. Torsional flexibility is usually treated with the cosine expansion model in equation 10 with ϕ is the current dihedral angle, and ci are constants respectively.

$$U_B = U_{bond} + U_{angle} + U_{dihedral} \tag{7}$$

$$U_{bond}(r) = \frac{1}{2}k(r - r_0)^2 \tag{8}$$

$$U_{angle}(\theta) = \frac{1}{2}k_{\theta}(\theta - \theta_0)^2 \quad (9)$$

$$U_{dihedral}(\phi) = c_0 + c_1[1 + \cos(\phi)] + c_2[1 - \cos(2\phi)] + c_3[1 + \cos(3\phi)] \quad (10)$$

2.3 Molecular Dynamics Tool and Potential Fields Used in This Thesis

All the simulations in this thesis are carried out using the molecular dynamics package GROMACS (van der Spoel et al. 2005, Hess et al. 2008) with a time step of 1.0 fs implemented in the leapfrog algorithm.

LJ potential parameters and partial charges for pure components studied in this thesis, except the octane molecules, are listed in Table 2.1. Calculation of unlike interactions is based on the Lorentz-Berthelot mixing rules in Equations 11 and 12. The cutoff distance for the Coulomb potential is set to 0.9 nm. For systems involving non-zero charges, long range corrections to electrostatic interactions are treated using the particle mesh Ewald (PME) summation method. The LJ parameters proposed by Cheng and Steele (1990) are used to model carbon atoms in the kerogen and graphite models. The parameters for NaCl are taken from Dang (1995). The force field of MgO follows Cygan et al. (2004).

$$\sigma_{ij} = \frac{1}{2}(\sigma_{ii} + \sigma_{jj}) \quad (11)$$

$$\epsilon_{ij} = \sqrt{\epsilon_{ii}\epsilon_{jj}} \quad (12)$$

For water molecules, the simple point charge extended (SPC/E) model is used, which is a rigid three-site model with a 0.1 nm O-H bond and 109.47° H-O-H angle (Berendsen et al. 1987). The SPC/E water model is one of the more widely adopted models of water and a comparative study by Vega et al. (2005) verified the accuracies of the SPC/E model predictions of density and water structural properties against

experimental observations. Vega and Abascal (2011) also investigated equation of state of water at high pressures of 10,000 and 20,000 bar, and the results of density prediction using SPC/E water model are very good. During the simulation, the SPC/E water bond lengths and angles are fixed by employing the SETTLE algorithm. These force fields for carbon and water have been utilized widely and verified in several previous studies including water adsorption in graphite slit-pores (Striolo et al. 2003) and the behavior of aqueous ionic solutions confined in graphite pores (Chialvo and Cummings 2011, Kalluri et al. 2011). For the carbonyl group, the LJ potential parameters and the partial charge for oxygen atom are taken from Tenney and Lastoskie (2006), and Liu and Wilcox (2012) involving CO_2 adsorption functionalized graphite slit pores with surface heterogeneities.

A united-atom alkane representation and the transferable potentials for the phase equilibria (TraPPE-UA) model is utilized for the octane molecules (Martin and Siepmann, 1998). The TraPPE-UA force field has been shown to accurately describe the vapor-liquid coexistence curves and critical properties of linear alkanes from methane to dodecane (Martin and Siepmann, 1998). Martin and Siepmann (1998) also investigated the influence of high pressure on PVT behavior and showed agreement with experiment for n-pentane. The TraPPE-UA alkane model was previously adopted to analyze adsorption of alkanes with different molecular lengths in graphite slit pores (Harrison et al. 2013) and on carbon nanotubes (Kondratyuk et al. 2005). Jiang et al. (2004) also utilized it to study capillary phase transitions of normal n-alkanes in a carbon nanotube. In TRAPPE-UA model, each CH3 or CH2 group is treated as a single pseudo-atom. A rigid bond length of 1.54 Å connects adjacent pseudo-atoms of an octane molecule. The

bond angle bending is modeled based on Equation 10. Torsional flexibility is expressed in equation 11. The interaction parameters for octane molecules are shown in Table 2.2.

Table 2.1: LJ potential parameters for pairs of pure atoms and partial charges

Atom type	$\varepsilon/k_B{}^*$(K)	σ (nm)	q (e)
Oxygen in water[1]	78.23	0.3166	-0.8476
Hydrogen in water[1]	0	0	0.4238
Carbon not in –C=O[2]	28	0.34	0
Carbon in –C=O[2]	28	0.34	1.047
Oxygen in –C=O[3]	78.23	0.3166	-1.047
Magnesium in MgO[4]	0.0004546	0.5264	1.05
Oxygen in MgO[4]	78.23	0.3166	-1.05
Sodium[5]	50.34	0.2584	1.0
Chloride[5]	50.34	0.44	-1.0

(* kB is the Boltzmann constant; [1] Berendsen et al. 1987; [2] Cheng and Steele 1990; [3] Liu and Wilcox 2012; [4] Cygan et al. 2004; [5] Dang 1995)

Table 2.2: Non-bonded and bonded parameters for the TraPPE-UA force filed for octane**

Non-bonded	$\varepsilon/k_B{}^*$(K)	σ (nm)	q (e)
CH3 – CH3	98	0.3750	0
CH2 – CH2	46	0.3950	0

Bond angle	$k_\theta/k_B{}^*(K/rad^2)$		θ_0 (°)		
CHx – (CH2) – CHy	62500		114		
Torsion	$c_0/k_B{}^*(K)$	$c_1/k_B{}^*(K)$	$c_2/k_B{}^*(K)$	$c_3/k_B{}^*(K)$	
CHx – (CH2) – (CH2) – CHy	0	355.03	-68.19	791.32	

(* k_B is the Boltzmann constant; ** Martin and Siepmann 1998)

To confirm that the equilibrium fluid distributions are achieved, values of temperature, energy, average pressure and average density profiles for fluids are checked to ensure meaningful interpretation. However, criteria for equilibrium are slightly different, depending on the studied cases. The types of ensembles, box sizes and the number of molecules utilized also vary by cases. All of these are described in the following chapters for different applications.

CHAPTER 3

PORE SCALE MODELS OF SHALE KEROGEN

The reliability of any molecular simulation study of thermodynamic properties of fluids in porous carbon materials relies on adopting an appropriate model for kerogen pores. While it is desirable to build a realistic model fully representative of the system of interest, the model design should also be simplistic enough to allow ease of interpretation and computational efficiency. The most common model for organic pore surfaces is the graphite slit pore model that consists of two planar graphite sheets separated by a specified distance. This arrangement has been utilized to quantify the thermodynamic properties of fluids under confinement in organic nanopores. However, this model is not able to replicate some structural properties especially the porous nature of kerogen, and the pure carbon model cannot reflect the maturity of the kerogen which is strongly linked to the amount of functionalized groups in kerogen. To honor the fact of the complexity and heterogeneity in kerogen composition, two kerogen models are constructed. These models use the fragments of graphene sheets to mimic the porous nature of kerogen. This chapter reviews the graphite slit pore models, describes the constructed simplified kerogen models with different degrees of maturity and provides advantages of the proposed models over the traditional ones.

3.1 Graphite Slit Pore Models Description

The study of fluid properties such as adsorption, modified critical properties and fluid densities in organic kerogen pores has traditionally relied on the use of a slit-shaped pure

graphite pore model (Striolo et al. 2003, Severson and Snurr 2007, Diaz-Campos 2010, Kalluri et al. 2011, Didar 2012). Striolo et al. (2003) analyzed water adsorption and distribution. Severson and Snurr (2007) studied the pore size effect and lengths of alkane chain on alkane adsorption. Kalluri et al. (2011) studied distribution of aqueous NaCl solutions. Diaz-Campos (2010) and Didar (2012) revealed the enhancement of sorbed gas due to pore confinement and demonstrated the need for new fluid models that provide properties distinct from the corresponding bulk fluid.

In graphene, carbon atoms (blue color) are arranged in a regular hexagonal pattern with separation of 0.142 nm and Figure 3.1a is an illustration of the structure of graphene. Layers of graphene sheets form graphite with a distance of 0.335 nm between adjacent sheets. The graphite slit pore is built by placing two graphite slabs separated vertically as shown in Figure 3.1b to form the top and bottom surfaces of a slit pore.

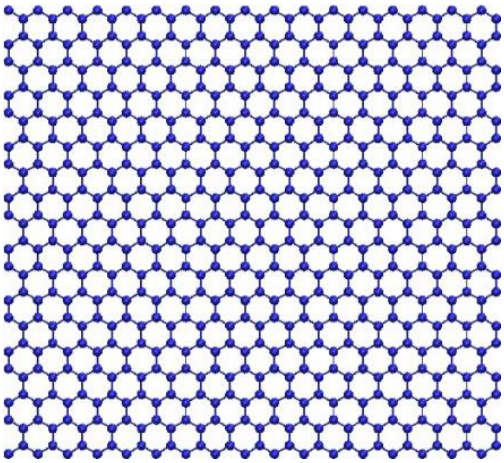

a) View from the top of one graphene sheet

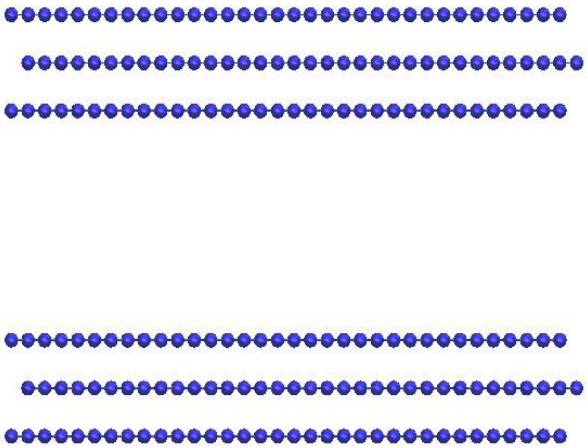

b) Graphite slit pore model

Figure 3.1: An illustration of the pure graphite model

In spite of the utility of graphene pore models for adsorption studies, the model lacks the ability to replicate the behavior of kerogen surfaces of intermediate maturity that are characterized by non-zero atomic O/C and H/C ratios. In order to address this deficiency, several researchers have proposed the use of activated carbon models that contain surface-bound oxygenated groups. Müller and Hung (2000) investigated the adsorption of water and water vapor – methane mixture on activated carbon pores while Striolo (2007) studied self-diffusion of water through oxygenated carbon nanotubes. Liu

and Wilcox (2012) recently analyzed the influence of some functionalized groups placed on the surface graphite on CO_2 adsorption. All these studies indicate that the behavior of fluid molecules in the vicinity of activated carbon is significantly different from the observations obtained for pure graphene surfaces. Figure 3.2 provides the detailed atomic structure of a carbonyl pair colored in black which includes a top and bottom carbonyl group grafted on the same breaking C-C bonds in the graphene basal plane. The bond length of the –C=O is 0.123 nm and the angle of the surface oxygen from the basal plane is 49.5° (Bagri et al. 2010).

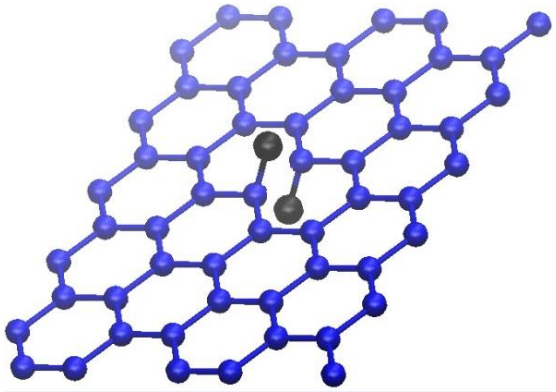

Figure 3.2: The atomic structure of graphene oxide sheet with a carbonyl pair containing a top and a bottom carbonyl group

However, the smooth and flat crystallite surfaces of graphite slit pores are likely to be deficient in representing the more complex structure of kerogen shown in the SEM images (Curtis et al. 2011, Chalmers et al. 2012).

3.2 Description of Kerogen Models with Different Degrees of Maturity

To reflect the complexity in kerogen structure and composition, I rely on two simplified approximations of kerogen that structurally and chemically mimic real organic matter.

The first model contains only carbon and is intended to represent highly mature kerogen associated with extremely low O/C ratios, such as those in gas shales (Jarvie 2012a) and is referred to as the "inactivated kerogen model" throughout the thesis. The second model simulates the nature of partially mature shales such as those associated with oil or condensate production and includes a representative oxygenated group, the carbonyl (-C=O) group, to mimic the presence of functional groups in kerogen of intermediate maturity. The addition of the oxygenated group in the second model creates hydrophilic locations within the kerogen and is referred to as "activated kerogen model". Both models are constructed by mimicking the maturation process of organic matter at elevated temperature and pressure conditions in a molecular dynamics simulator and contain features that are more realistic than the graphite slit pore systems.

The inactivated kerogen model used here is composed of fragments of graphene sheets with various hexagonal unit cells shown in Figure 3.3a with blue color describing carbon atoms and with a dimension of 4.02 nm by 3.87 nm by 2.00 nm. The total number of carbon atoms is 1257. This model is constructed using molecular simulation at the high temperature of 1340 oF and pressure of 7252 psi for a sufficiently long time using an NPT ensemble. The initial arrangement of graphene sheets to construct this model is random; however the equilibrium configuration of the carbon atoms is progressively reached through a sufficiently long simulation time. The intention is to replicate some of the realistic kerogen structural profiles previously reported in literature (Facelli et al. 2011).

The activated kerogen model is based on the inactivated model, but it contains hydrophilic carbonyl (-C=O) groups to model O/C ratios of kerogen of intermediate

maturity. Oxygen atoms are grafted onto randomly chosen edge carbon atoms in the inactivated kerogen model. Figure 3.3b illustrates this model with black circles representing the 20 oxygen atoms in the kerogen body. With the same total number of carbon as the inactivated model, the O/C ratio in this model is around 1.6%. Although lower than O/C ratios of kerogen from shales of intermediate maturity (Vandenbroucke et al. 2007), the results of simulation studies demonstrate that even for such small O/C ratios, the behavior of water in activated kerogen is substantially different from a highly mature inactive kerogen model. Hence with a more realistic ratio, the effect of surface activation is expected to be much more significant. I utilize a 0.1214 nm -C=O bond length (Brennan et al. 2002) and assign the oxygen atom in the direction that carbonyl bond axes are parallel to the basal plate of the hexagonal cells. The oxygen atom in the carbonyl group carries a -1.047e point charge, derived from Liu and Wilcox (2012). To maintain the electro-neutrality, a charge of +1.047e is assigned to the carbon atom that directly connects to the oxygen, while the other carbons in the model kerogen have zero charge.

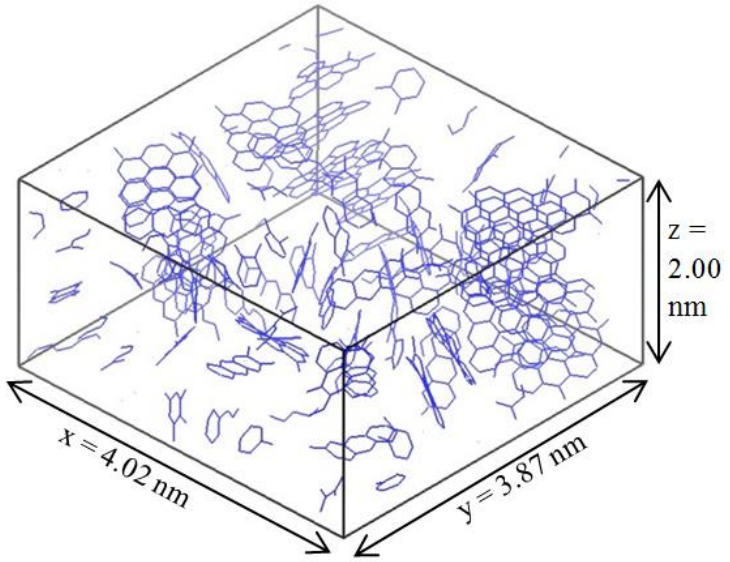

a) The inactivated kerogen model

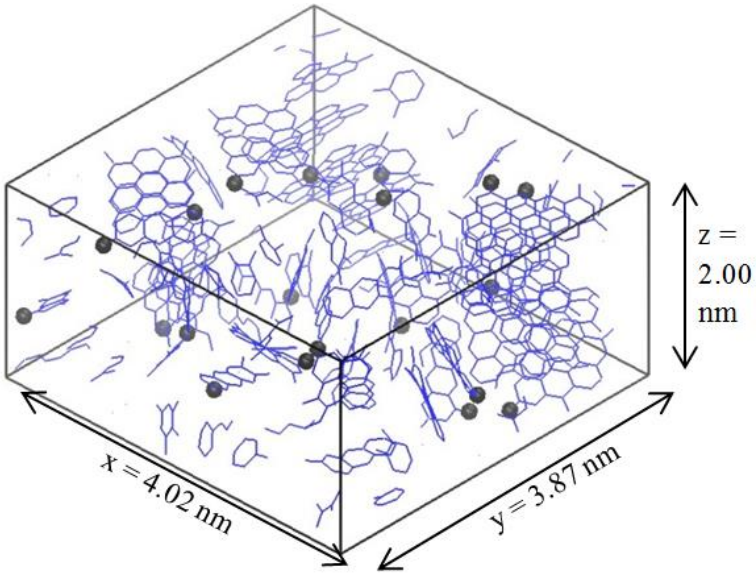

b) The activated kerogen model

Figure 3.3: Illustrations of the activated and inactivated kerogen models

To quantify the roughness of the kerogen surface, the region of top 5 Å in vertical direction is studied, as shown in Figure 3.4. In Figure 3.4a, the green area corresponds to the plane z = 15 Å and the red shaded plane is the middle surface between z = 15 Å and

the top of the kerogen surface z = 20 Å. Deviation of carbon atoms in the z > 15 Å regions from the red shaded plane provides an idea about the surface roughness. In Figure 3.4b, the deviations of some selected carbons are marked by arrows. Figure 3.5 shows how carbon atoms are distributed away from the mid-plane of z = 17.5 Å. Minimum, maximum, mean and the standard deviation are also calculated for these deviations and the results are tabulated in Table 3.1. Figure 3.5 and Table 3.1 show that the surface is very rough.

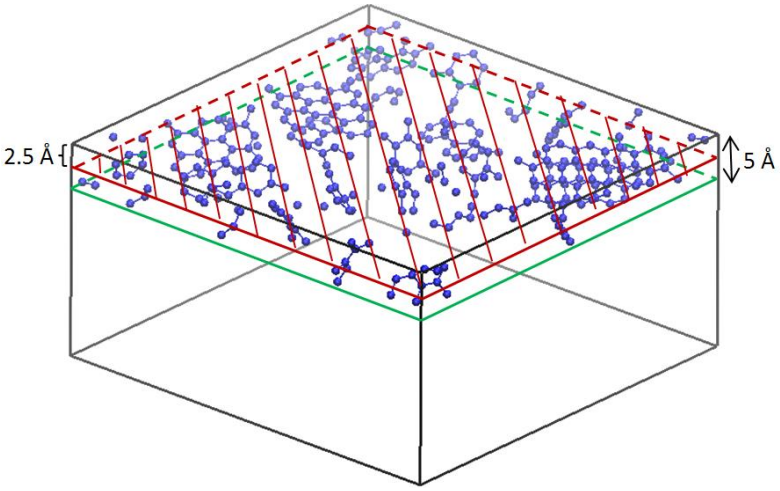

a) Overview

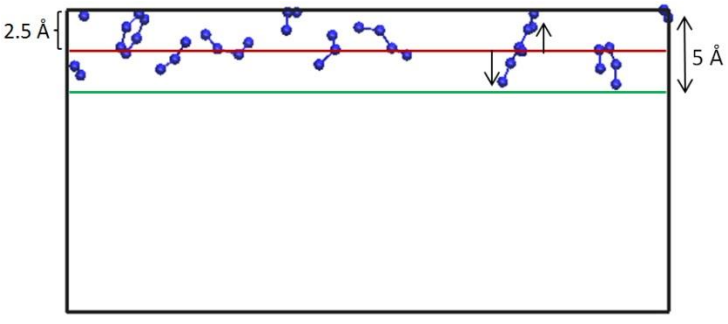

b) Side view with parts of carbon atoms

Figure 3.4: Using carbon atoms in the vertical top layer of 5 Å length to quantify the roughness of the kerogen surface

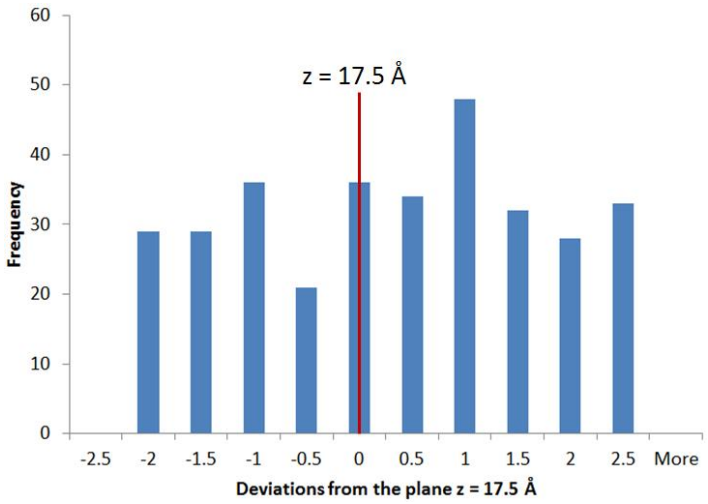

Figure 3.5: Histogram of deviations of atoms in the z > 15 Å region from the plane z = 17.5 Å

Table 3.1: Statistics of deviations of atoms in the z > 15 Å region from the plane z = 17.5 Å

Minimum	-2.47
Maximum	2.47
Mean	0.08
Standard Deviation	1.40

3.3 Organic Pore Model

Figure 3.6 illustrates an organic pore structure using the activated kerogen model shown in Figure 3.3b. This structure is built by placing two slabs of porous kerogen (referred to as a "kerogen body") across a slit pore volume. The pore width can be adjusted by changing the distance between the bottommost carbon atoms of the top slab and the

topmost carbons of the bottom slab. The bounding box of Figure 3.6 encloses the pore model as well as free volumes surrounding the pore model and therefore allows fluid molecules to attain their equilibrium configuration either within the slit pore and porous kerogen or outside in the bulk volume. Consequently, the model construction allows a study of the natural arrangement of fluid molecules in shale nanopores where they are likely to preferentially occupy either the pore volume or remain outside the pores in bulk spaces such as fractures depending on the affinity of the fluids to the pore walls.

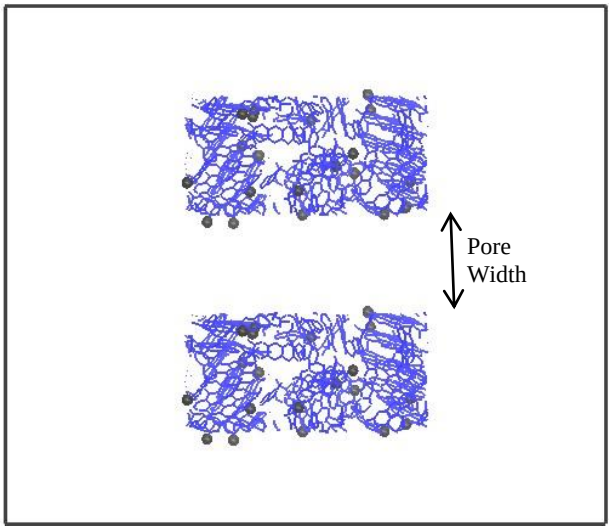

Figure 3.6: Activated kerogen slit pore model with adjustable pore width

In comparison with the graphite slit pore model, the kerogen models (Figure 3.3) proposed here are characterized by structural features similar to those observed in shale organics that are absent from the graphite model (Hu et al. 2013a, 2013b). Consequently, the fluid adsorption is no longer restricted to a planar surface as in the graphite model. Secondly, tortuous pathways and the complex porous structure of organic matter are embedded into these models. Thirdly, the irregular packing of graphitic nanocrystals in the proposed kerogen models leads to disordered nanostructure and imperfect pore

openings. These influence the long range correlation and impact the free energy barriers for molecules to enter pores. Lastly, the addition of surface functionalized groups reflects kerogen maturity and may alter surface wettability due to the hydrophilic nature of these active sites. Therefore, although still an approximation to kerogen, the proposed kerogen models represent a substantial improvement over the graphite slit pore model and the corresponding impact on confined fluid behavior will be demonstrated in a subsequent discussion.

CHAPTER 4

A MICROSCOPIC CHARACTERIZATION OF WETTABILITY IN KEROGEN CHARACTERIZED BY VARYING DEGREES OF MATURITY

The kerogen maturation process is associated with the loss of H/C and O/C ratios which may influence the wettability depending on the affinity of these functionalized molecules with water.

This chapter provides conclusive tests to quantify the wetting angle of water on organic surfaces and determines the kerogen-water-octane contact angle. To avoid the effect of surface roughness on the results of wettability, the traditional flat kerogen surface is utilized and grafting functionalized groups onto it simulates activated surface. The wettability analysis begins with a study of droplets of pure water on the surfaces and is extended to a mixture of water and alkanes. The results from these studies are then utilized to determine contact angles for each of the phases and to quantify wettability. The results imply that the wettability in kerogen is very likely to be heterogeneous. Depending on the maturity level, kerogen may be hydrocarbon wetting at high maturity, neutral wetting at intermediate maturities or even hydrophilic for organic surfaces of very low maturities.

4. 1. Graphene Oxide Surfaces

In this work, the graphene surface model shown in Figure 3.1 is chosen as a proxy for kerogen surfaces. Because graphene is 100% carbon, it is chosen to represent highly

mature kerogen with negligible atomic O/C ratios and virtually no surface functionalized sites. Modeling less mature kerogen pore surfaces with higher atomic C/O ratios, involves grafting different amounts of the representative oxygenated group onto the graphene surface. Bagri et al. (2010) reported that the most stable and favorable structure within the graphene basal plane involved the carbonyl groups when compared to other well-known functional groups such as epoxies and ethers. For this reason, the representative oxygenated group considered in this work is the carbonyl (-C=O) group. The atomic structure of the oxidized graphene is introduced in Figure 3.2. The degree of maturation is described by the n-by-n carbonyl pairs where n is an odd integer and varies from 0 to 8. The resulting kerogen surfaces are shown in Figure 4.1 with blue and black colors representing surface carbon and oxygen respectively. In all kerogen models, the total surface areas is 4.26 nm by 3.936 nm. Figure 4.1 also shows a uniform distribution of carbonyl pairs to avoid localized effects that may result from a heterogeneous distribution of the activated sites. A later section of this work also models a few cases with a heterogeneous distribution of carbonyl pairs. Although the overall atomic O/C ratios remain identical, the localization of these polarized pairs has a significant impact on the behavior of water and eventually on kerogen wettability.

The results of computed O/C ratios for each surface are tabulated in Table 4.1. The table illustrates that the O/C ratios of kerogen in this study range from 0 to 0.2. An example of type II kerogen from the Paris Basin Toarcian provides an example of the variation in O/C ratios with kerogen maturity. According to Behar and Vandenbroucke (1987) the atomic O/C ratio of 0.196 at the beginning of diagenesis changed to 0.089 at the beginning of the catagenesis and finally evolved to 0.026 at the end of catagenesis.

Hence, the variation of the O/C ratios chosen for this study is highly representative of gas shales that largely contain type II kerogen.

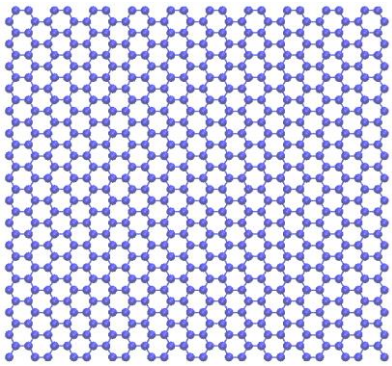

a) Kerogen without carbonyl pairs

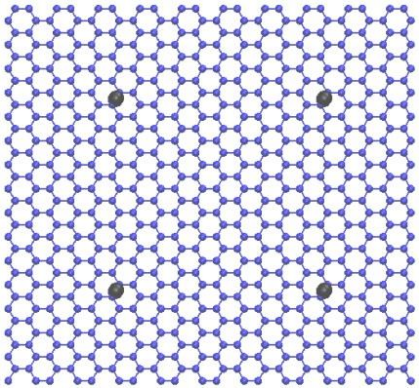

b) Kerogen with 2-by-2 carbonyl pairs

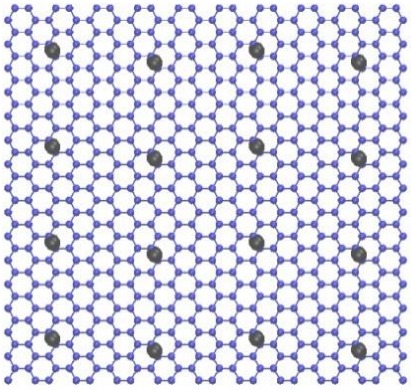

c) Kerogen with 4-by-4 carbonyl pairs

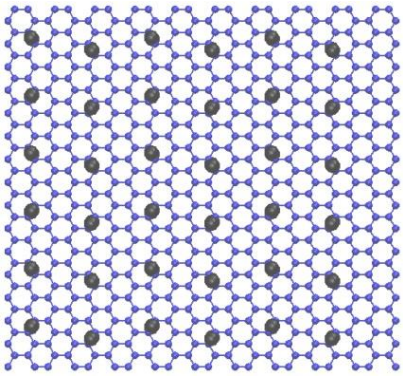

d) Kerogen with 6-by-6 carbonyl pairs

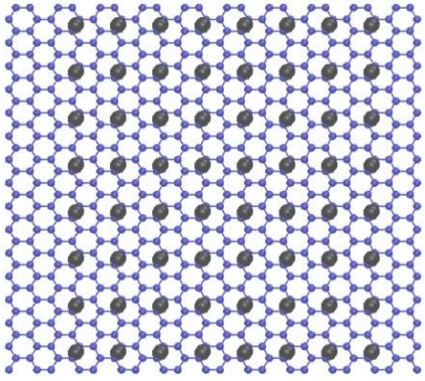

e) Kerogen with 8-by-8 carbonyl pairs

Figure 4.1: Kerogen surfaces are modeled using graphene while kerogen maturity is represented by the atomic O/C ratios going from the most mature in (a) to the least mature in (e)

Table 4.1: Calculated O/C ratio corresponding to various kerogen models

	Kerogen models				
	No carbonyl pairs	2-by-2 carbonyl pairs	4-by-4 carbonyl pairs	6-by-6 carbonyl pairs	8-by-8 carbonyl pairs
Calculated O/C ratio, %	0%	1.25%	5%	11.25%	20%
Total carbon numbers	640	640	640	640	640
Total carbonyl pairs	0	4	16	36	64
Total carbonyl groups	0	8	32	72	128

4.2 Determination of Wettability through Molecular Dynamics

When applying a thin layer of liquid to a solid surface, wetting is the ability of the liquid to stick to the solid surface. Known as wettability, the degree of wetting is generally quantified by the contact angle θ at which the liquid–vapor interface meets the solid–liquid interface. The contact angle of a macroscopic droplet is well described by the celebrated Young's equation explaining the force balance between adhesive and cohesive forces. For water, if $\theta < 90°$, the solid surface is considered hydrophilic; if $\theta > 90°$, then it is hydrophobic. Complete wetting corresponds to $\theta = 0°$.

The determination of contact angle is normally a three-step process following Werder et al. (2003) and Scocchi et al. (2011). First, the ensemble average densities are calculated for a water droplet by introducing a concentric cylindrical binning of equal

volume. The vertical coordinate of the topmost layer in the surface is used as the zero reference level, and the axis normal through the mass center of the droplet is considered as the reference axis. In this study, the cylindrical bins have a height of 0.1 Å and a base area per bin of 10 Å2. By averaging the counted number of water molecules falling within a given volume element, the average density maps for water droplet in different systems are obtained. Detailed density maps for different systems are illustrated in their respective sections below. Secondly, the fluid-vapor interface is identified as an isochoric density profile at a particular density. Lastly, the density profile is fitted with some function and is extrapolated to the surface to measure the contact angle. In this paper, I use a circular best fit. As an example, Figure 4.2 illustrates how to calculate contact angle using the graphene system. Black points are the isochoric density points and fitted circle are shown in red line. Tangent line determining contact angle is illustrated in green. For this example, the isochoric density points below a height of 6 Å are not considered for the fitting to avoid the influence of the solid surface on the density.

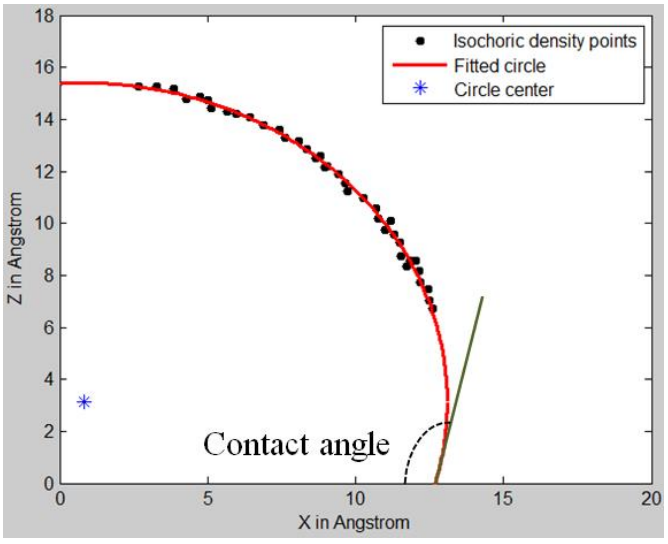

Figure 4.2: Profile of the water droplet in graphene system obtained from density contours

4.3 The Effect of Kerogen Maturity on Contact Angle of Water Droplet

4.3.1 System configuration & initialization

The fluid studied is pure water droplet. During the simulation, oxygen atoms in functional groups and carbon atoms are held stationary, and water molecules are free to move. Simulations are conducted at ambient conditions with the temperature controlled at 300 K and the pressure fluctuating around 1 bar. The canonical ensemble (NVT) is used where the number of molecules, the system volume and the temperature are constant. All studies are run for 22 ns to make sure that the system equilibrium is reached. I calculate temperature, pressure, energy, fluid density and contact angles to ensure equilibration. Once the equilibrium has been achieved, the results from the last 5 ns are averaged for the final analysis. The initial configuration is built with 175 water molecules artificially placed on the surface center. Figure 4.3 demonstrates this initial arrangement using the 4-by-4 GO system as an example. In this figure, the oxygen and hydrogen in water are represented by red and white colors. All other systems use equivalent initial arrangements as Figure 4.3 illustrates. As the simulation progresses, water molecules form droplets and their shapes vary with the amount of carbonyl pairs on the surface.

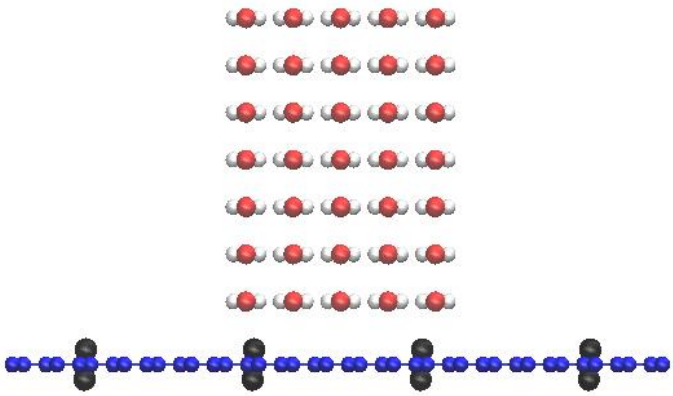

a) Side view

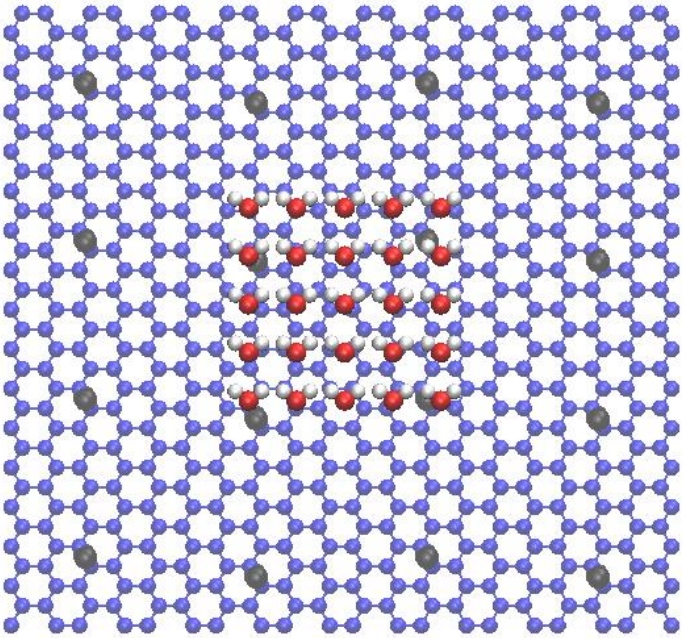

b) Top view

Figure 4.3: Demonstration of the initial arrangement for all the systems with water molecules artificially located near the center of the surfaces. The example here is a 4-by-4 GO system, but all other systems have the same initial configuration

4.3.2 Results

The representative simulation snapshots of the final configurations are provided in Figure 4.4. In all simulations, water molecules aggregate to form droplet shapes, due to the fact that water molecules are polarized and they tend to form hydrogen bonds with each other.

However, the heights of water droplets seem to decrease, as the amount of surface functionalized groups increase. For the graphene model, the 2-by-2 and 4-by-4 graphene oxide monolayers, the water molecules are observed to form clusters close to the surface. In comparison, water forms sheets adjacent to the 6-by-6 and 8-by-8 graphene oxide surfaces. It appears that there exists a critical density of surface active sites beyond which the kerogen pore system could be considered to be complete water-wet. The study shows that the shape of the water droplet has a strong dependency on kerogen maturity that is modeled by modifying the density of the surface functionalized groups.

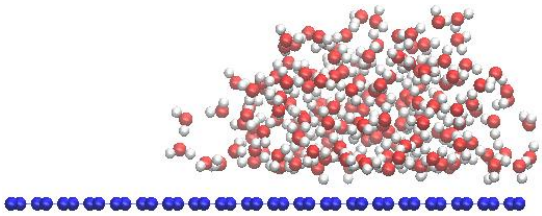

a) Kerogen without carbonyl pairs

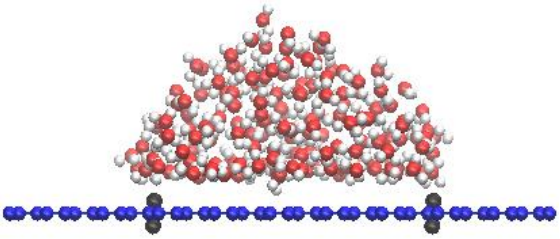

b) Kerogen with 2-by-2 carbonyl pairs

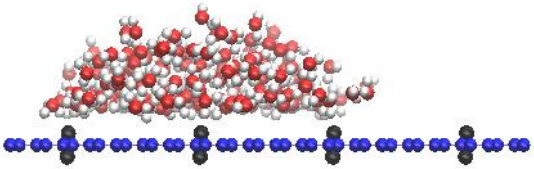

c) Kerogen with 4-by-4 carbonyl pairs

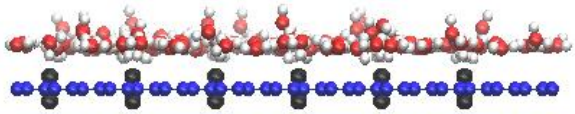

d) Kerogen with 6-by-6 carbonyl pairs

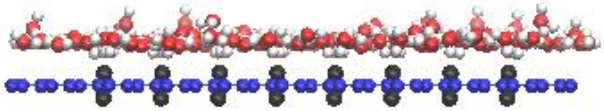

e) Kerogen with 8-by-8 carbonyl pairs

Figure 4.4: Final configurations for different systems

To quantify the possible wettability alternation, contact angles is calculated for each case. The average density maps in number of molecules per $Å^3$ for water droplet on pure graphene, 2-by-2 and 4-by-4 graphene oxide surfaces are shown in Figure 4.5. I do not include the density maps for the other two models, simply because they appear to be complete wetting in Figure 4.4. Figure 4.5 confirms that the shape and the height of the water droplets change with the density of surface functionalized groups.

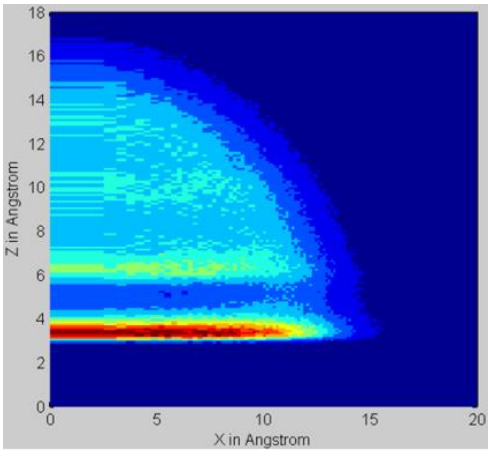

a) Kerogen without carbonyl pairs

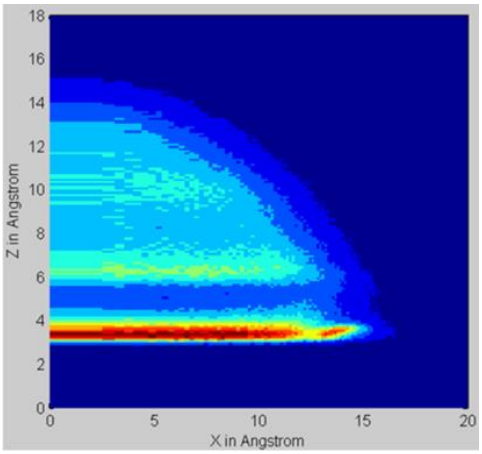

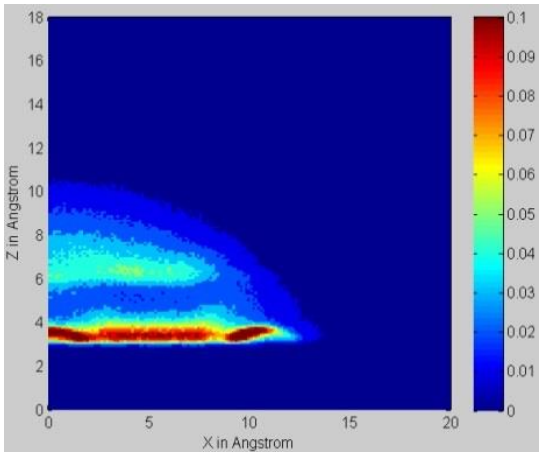

b) Kerogen with 2-by-2 carbonyl pairs c) Kerogen with 4-by-4 carbonyl pairs

Figure 4.5: Average density maps for water droplet in different systems. Z=0 corresponds to the carbon surfaces

The calculated contact angle for each system is shown in Table 4.2. The contact angle of the graphene monolayer surface obtained from the simulation is consistent with the experimental data (Shih et al. 2012) of 96° and other molecular dynamics simulation results (Taherian et al. 2013) of 100°. Additionally, the surface wettability changes from hydrophobicity of the graphene model to neutral wetting of the 2-by-2 graphene oxide

model, and is even further altered to hydrophilicity when the graphene oxide surfaces have intermediate levels of surface activation. The surface becomes complete wetting with an O/C ratio higher than a critical value (O/C = 0.1125 for the 6-by-6 GO model). Figure 4.6 plots the contact angle versus the O/C ratio. Clearly, as the ratio increases, the contact angle decreases until a threshold O/C ratio is reached. Hence, the wettability of kerogen is very likely to depend on its maturity level.

Table 4.2: Calculated contact angles for different systems

	8-by-8 –C=O kerogen	6-by-6 –C=O kerogen	4-by-4 –C=O kerogen	2-by-2 –C=O kerogen	Graphene: this MD simulations	Graphene: experimental data and other MD simulations*
Contact angle θ, degree	0°	0°	64.51°	89.25°	102.67°	95~100°

(* Shih et al. 2012, Taherian et al. 2013)

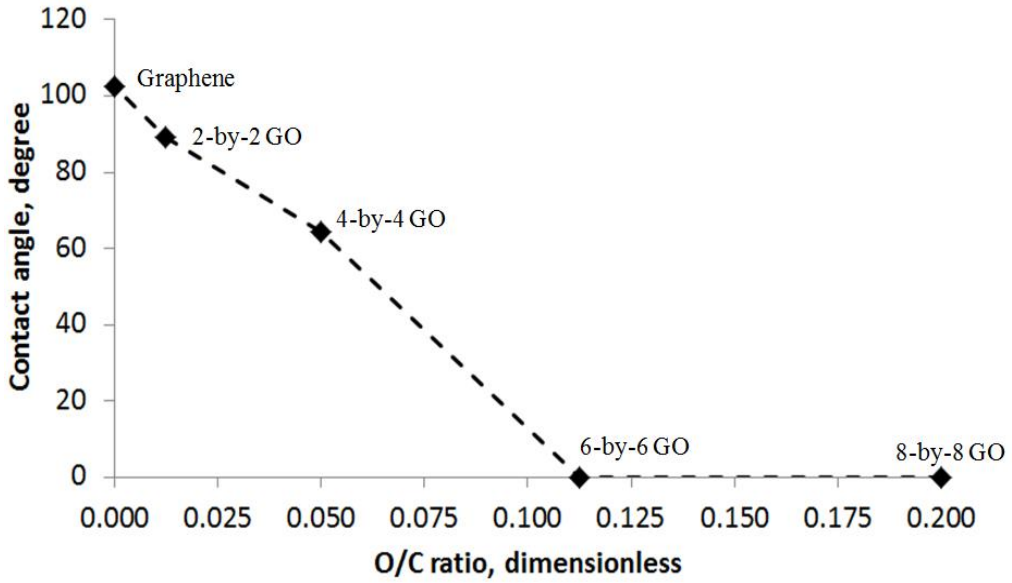

Figure 4.6: Contact angle dependence on O/C ratio for pure water wettability study

4.4 Characterization of Wettability in Kerogen with Water and Hydrocarbon in Systems

4.4.1 System configuration & initialization

This session is an extension of the previous study in Chapter 6. It includes a mixture of water and octane molecules in the systems. All the fluid molecules are allowed to move as simulation time progresses and their different behavioral patterns associated with each surface are examined to evaluate kerogen wettability. During the simulation, the surfaces are held stationary. For all the cases, simulations are conducted with both canonical ensemble (NVT) and isothermal-isobaric ensemble (NPT) where N, V, P and T represent constant quantities of numbers of molecules, system volume, pressure and temperature accordingly. To start simulations, I first run a 10 ns NVT and then a 10 ns NPT with Berendsen weak coupling method. Finally, a 50 ns NVT concludes the simulations with stable equilibrium configurations achieved. During the simulations, the pressure is controlled at 1 atm with a relaxation time of 100 fs and the temperature is maintained at

300 K (80 oF) using the Nose-Hoover thermostat approach with a relaxation time of 200 fs. In the final NVT step, I check values of pressure, temperature, energy, fluid density and contact angle to ensure that system equilibrium is reached for each case. All these quantities are constant for the last 20 ns of the 50ns NVT simulations and hence the simulation results of the last 20 ns are used to produce the data for analysis.

The behavior of octane and water molecules in the vicinity of different surfaces is studied. The total number of fluid molecules is 560 with 280 octane and 280 water molecules. The initial configuration is chosen to avoid any bias caused by grouping like molecules together and consists of water and alkane molecules arranged alternatively to fill the simulation box of size 4.26 nm by 3.94 nm by 5.67 nm. Due to the periodic boundary condition applied, the surfaces extend infinitely in the X- and Y- directions with an effective pore width of about 5 nm. For each system, the surface is built based on a three-layer graphite with the surface activated site applied to the top layer only. The purpose of this arrangement is to construct a nano-sized pore where the upper pore wall is graphene while the bottom surface contains functionalized groups thereby providing a strong contrast in surface chemistry and a means to illustrate the significance of surface activated sites to fluid behavior. Figure 4.7 illustrates the initial configuration of the octane and water molecules in a kerogen system with 6-by-6 carbonyl pairs where green color is for the octane, and the white and red are for hydrogen and oxygen atoms in water molecules. Initial arrangements for all other systems are equivalent to that shown in Figure 4.7.

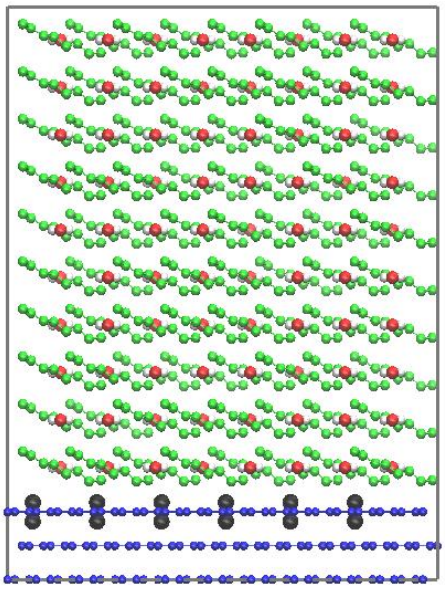

Figure 4.7: The initial arrangement of binary fluid in a kerogen system with 6-by-6 carbonyl pairs

4.4.2 Characterization of Wettability in Kerogen

The fluid arrangements for the various graphene surfaces with varying levels of O/C ratios when equilibrium is achieved are displayed in Figure 4.8. Because of the periodic boundary conditions imposed and the fact that the carbonyl groups are only grafted onto the top graphene sheet of the 3-sheet graphite surface, the fluid at the top of the simulation box is effectively under the influence of a pure graphene surface while the fluid molecules in the lower part of the box are influenced strongly by the activated surface. The level of influence is controlled by the density of the carbonyl groups. For the polar water molecules, there are two competing forces: the interaction between the polar carbonyl group and water as well as the water-water interactions. Figure 4.8 illustrates some observations listed below:

1. Water molecules form round or drop-shape clusters when octane molecules are present. The clustering mechanism is because polarized water molecules have a strong

tendency to form hydrogen bonds with each other. This is observed in all case studies irrespective of the level of surface activation.

2. The locations of the water droplets however depends on the intensity of surface activation. When the surfaces contain very few carbonyl groups, these additional groups have an almost negligible impact on the water droplet, as the accumulated water distributes itself around the center of the 5 nm pore and there are only negligible differences between the pure graphene surface (Figure 4.8a) and the 2-by-2 carbonyl pairs kerogen pore wall (Figure 4.8b) indicating that the lower surface is largely hydrophobic with an affinity to octane. However, as more activated sites become available in Figure 4.8c-e, water molecules form "bridges" with the surface hydrophilic groups. As a result, the water clusters are attached to these kerogen surfaces and their shape reflects the influence of the kerogen maturity. The kerogen surface with O/C = 5% (Figure 4.8c) appears to be hydrophobic as indicated by the water droplet contact angle; however, higher O/C ratios influence the height, the radius and the contact angle of the droplet, perhaps resulting in different wetting properties.

3. A distinct adsorbed octane layer is formed in the vicinity of the pure graphene surface, due to planar geometry of the surface and the strong potential between the octane and the surface carbon. These well-defined alkane layers are also reported in Severson and Snurr (2007), Diaz-Campos (2010) and Didar (2012). When the kerogen surface is modified to represent intermediate maturity levels (Figure 4.8c-e), the water aggregates break the adsorbed octane layer due to the stronger interaction between water and the surface oxidized sites.

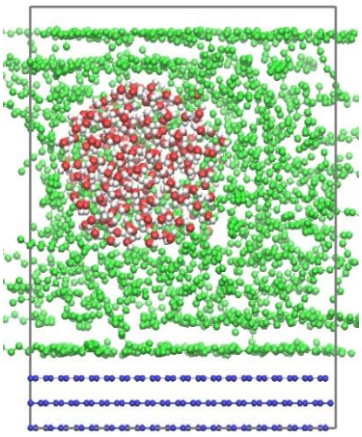

a) No –C=O pairs kerogen model

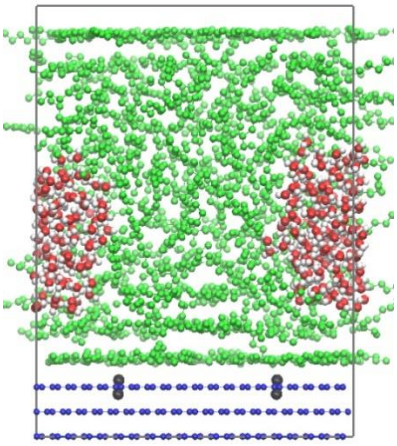

b) 2-by-2 –C=O pairs kerogen model

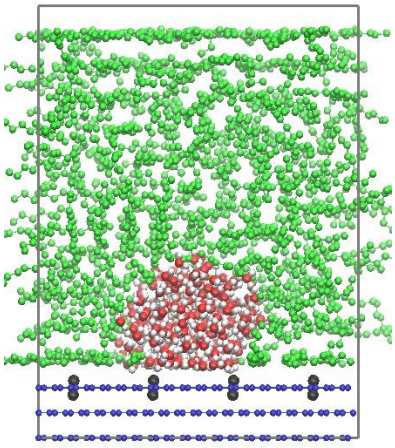

c) 4-by-4 –C=O pairs kerogen model

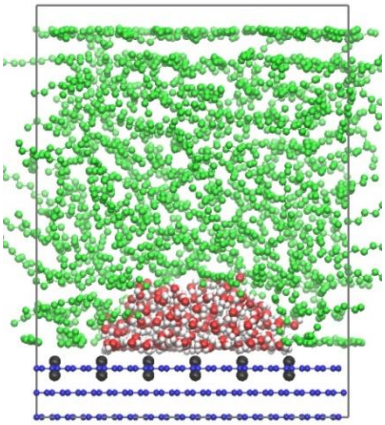

d) 6-by-6 –C=O pairs kerogen model

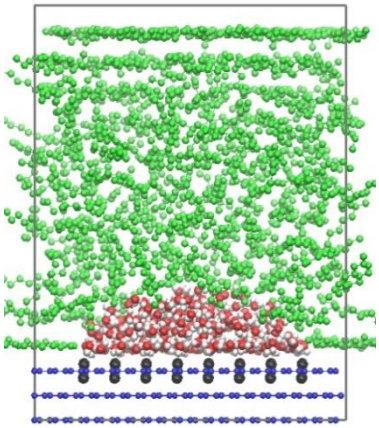

e) 8-by-8 –C=O pairs kerogen model

Figure 4.8: Representative snapshots of equilibrium state for kerogen surfaces of different degrees of activation

To calculate contact angles, the average density map of water is plotted in Figure 4.9, providing isochore information in number of molecules per $Å^3$ for the kerogen models with 4-by-4, 6-by-6, and 8-by-8 carbonyl pairs. For the other two kerogen models, water aggregates in the center of the pore, indicating strong hydrophobicity of the surfaces; thereby the contact angles for these two models are not calculated. As figure 4.9 illustrates, the height of the droplet decreases and the droplet extends to attach to the surface in a larger area as the O/C ratio increases.

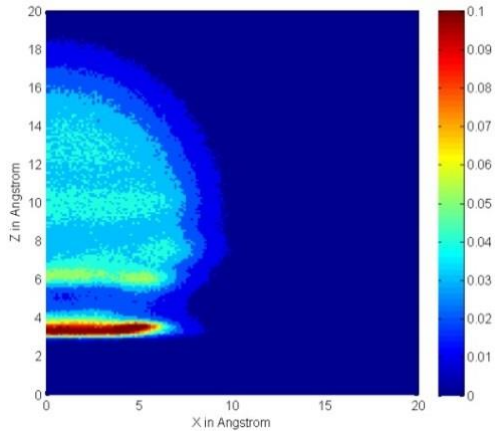

a) 4-by-4 –C=O pairs kerogen model

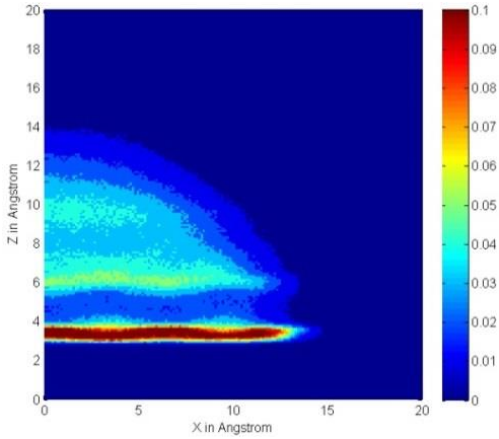

b) 6-by-6 –C=O pairs kerogen model

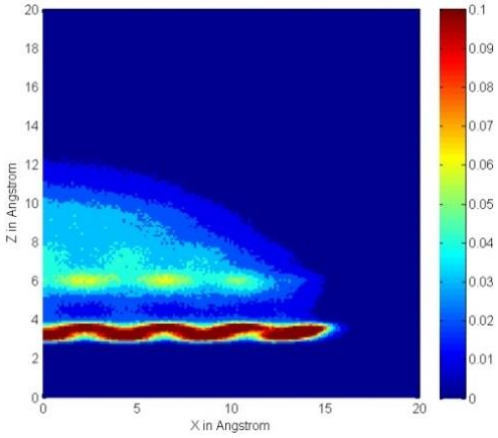

c) 8-by-8 –C=O pairs kerogen model

Figure 4.9: The average density map of water clusters for 3 kerogen models

The calculated contact angles for the 3 kerogen models along with their responding O/C ratios are summarized in Table 4.3. For the kerogen model with 4-by-4 carbonyl pairs, the contact angle demonstrates that the surface is still hydrophobic with an O/C ratio equal to 5%. However, when this ratio increases to 11.25%, the surface becomes almost neutral wetting and it further alters to become hydrophilic at the highest O/C ratio. These quantitative results confirm that the wettability of the kerogen is very likely to be a function of the surface functionalized groups and thereby depends on the level of maturity of the kerogen.

Table 4.3: Calculated contact angles for 3 kerogen models with uniformly distributed carbonyl pairs

	Kerogen models with uniformly distributed carbonyl pairs		
	4-by-4 -C=O pairs	6-by-6 -C=O pairs	8-by-8 -C=O pairs
O/C ratios, %	5%	11.25%	20%
Contact angle θ, degree	180°	92.18°	71.12°

4.4.3 The Influence of Surface Heterogeneity on Wettability

This section discusses the impact of heterogeneity in the placement of surface activated groups on kerogen wettability. The kerogen surfaces of Figure 4.10 are constructed with similar atomic O/C ratios as the surfaces containing 4-by-4, 6-by-6, and 8-by-8 carbonyl pairs in Figure 4.1; however in Figure 4.10, the distribution of the carbonyl groups is random. The motivation for this study is to understand the link between the local densities of the surface oxygen to the wetting characteristics of the surfaces. By employing the same initial configuration and simulation process as previously described, the finalized states are shown in Figure 4.11. By comparing the results of Figure 4.11 with those presented in Figure 4.8, it becomes apparent that with a non-homogeneous distribution of carbonyl groups, the contact angles are lower for the same levels of atomic O/C ratios. For the case of O/C = 20%, water molecules even form sheets adjacent to the kerogen surface indicating a strong affinity towards water. Table 4.4 tabulates the contact angles for these three heterogeneous kerogen models. Surface wettability changes from hydrophobic with the kerogen model carrying 5% O/C ratio to hydrophilic with an O/C equivalent of 11.25% and becomes completely water wetting at an O/C ratio = 20%. The results seem to indicate that the effect of localization creates conditions where beyond a critical local O/C ratio, kerogen may become completely hydrophilic.

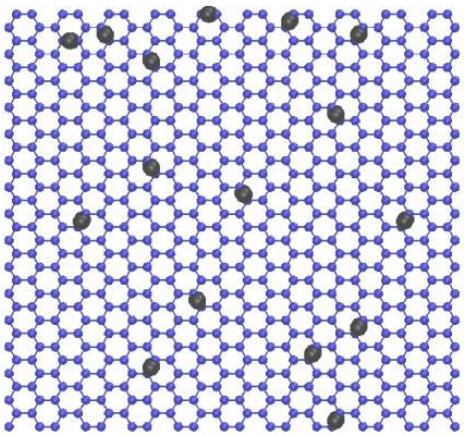

a) Kerogen model with O/C =5%

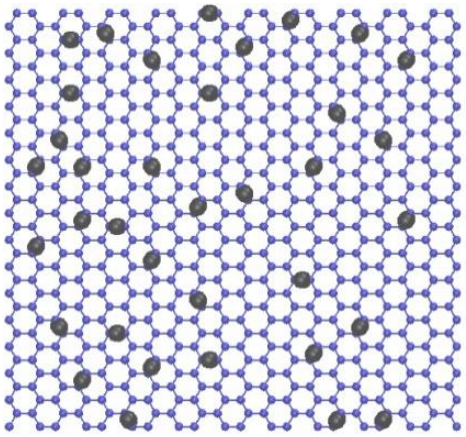

b) Kerogen model with O/C =11.25%

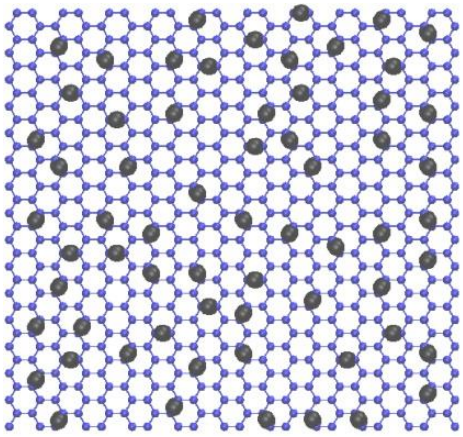

c) Kerogen model with O/C =20%

Figure 4.10: Modeling of kerogen with heterogeneous distributed carbonyl groups

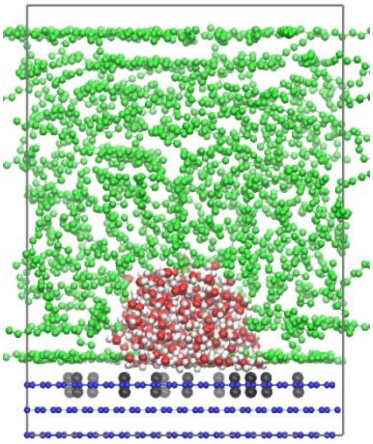

a) Kerogen model with O/C =5%

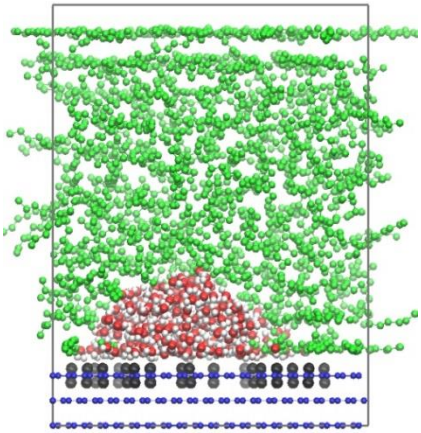

b) Kerogen model with O/C =11.25%

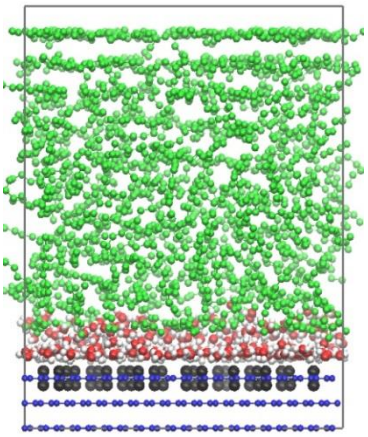

c) Kerogen model with O/C =20%

Figure 4.11: The representative snapshot of equilibrium state for kerogen systems with heterogeneous distributed carbonyl groups

Table 4.4: Calculated contact angles for 3 kerogen models with heterogeneous distributed carbonyl pairs

	Kerogen models with heterogeneous distributed carbonyl pairs		
	O/C = 5%	O/C = 11.25%	O/C = 20%
O/C ratios, %	5%	11.25%	20%
Contact angle	120.55°	83.58°	0°

4.5 Conclusion

This chapter reports the wettability changes of the organic materials in terms of contact angle with various kerogen maturity levels. In all cases, the polar water molecules aggregate to form clusters in the present of alkane. The shape and the location of the water cluster, however, have a strong correlation with the density of the surface functionalized sites that serves as a proxy for kerogen maturity.

The key observations of this study are summarized as following:

1. With small O/C ratios as seen in highly mature gas shales, the kerogen is very likely to be octane-wetting. Small levels of surface activation has a negligible impact on wettability. However, for shales of intermediate maturity and higher O/C ratios, kerogen may be heterogeneous-wet or even hydrophilic.

2. Heterogeneity in the placement of the surface activated sites tends to decrease water droplet contact angles resulting in kerogen surfaces that are more water-wetting than the surfaces with a uniform distribution of functionalized sites.

3. It is possibly that, in reality, there exists a critical density of surface functionalized sites beyond which the kerogen pore system could be considered to be completely water-wet.

The results from this study have several implications of practical significance. Firstly, it demonstrates that kerogen wettability is a function of shale maturity. Secondly, it indicates that modeling multiphase flow, estimating hydrocarbon-in-place and understanding changes in fluids saturations is more complex than previous thought. More research is needed to fully capture the reservoir-scale impact of the changes in wettability with kerogen maturity.

CHAPTER 5

THE BEHAVIOR OF WATER

IN ORGANIC KEROGEN NANOPORES

Understanding the distribution of water in organic-rich shales is crucial to quantifying the relationship between oil well productivity and recovery of fracture water, to evaluating or interpreting multiphase flow measurements and simulations for wettability and relative permeability effects and to accurately model storage of hydrocarbons. The study of the governing factors controlling the distribution of water in organic rich shales is therefore merited.

This chapter focuses on a pore-scale study of the distribution of water in organic kerogen shale nanopores. Different kerogen models are compared, and the sensitivity of the results to pore size, degree of kerogen maturity and pore wall roughness on the storage of water are examined. Additionally, the effects of pore filling and phase changes in kerogen nanopores that are a result of the characteristics of nanopore confinement of water are demonstrated.

5.1 System Configuration and Initialization

Three slit pore sizes of 1.6, 1.2 and 0.9 nm are considered in this study with the pore located in the center of the simulation box shown in Figure 3.4. For the inactivated and activated kerogen model, considering the roughness of the pore surface, those pore sizes are measured between the lowest carbon atom of the upper surface and the top-most atom of the lower one. For the graphite model, pore width refers to the center to center distance

between the bottom-most layer of the top slab and the top-most layer of the bottom slab. The box dimension is 10 nm by 3.87 nm by 8.6nm for kerogen systems and 10 nm by 3.834 nm by 4.8 nm for graphite slit pore models. Information regarding the numbers of molecules and the carbon density for the different pore systems is provided in Table 5.1. For graphite, the density of carbon atom is known to be 114 atoms per nm3 (Steele 1974). The carbon densities in both activated and inactivated kerogen are 2514/(2*4.02*3.87*2) ~ 40 atoms per nm3. The initial configuration is built with water molecules placed outside of the slit pore to allow the molecules to reach their equilibrium configuration either inside or outside the pore. Therefore as the simulation progresses, water either fills the pore or remains outside of it depending on the interactive forces between water and the pore wall.

To run the simulations, both canonical ensemble (NVT) and isothermal-isobaric ensemble (NPT) are used. A 10 ns NPT is conducted to set the pressure to 200 bar (2901 psi) by Berendsen weak coupling method. Then, a 50 ns NVT is run with a temperature maintained at 300 K (80°F) using the Nose-Hoover thermostat. The relaxation time for the Nose-Hoover thermostat and the Berendsen weak coupling method is set to be 100 fs. During the process, all the carbon and oxygen atoms in the kerogen bodies are fixed. The simulation box is periodic in three directions. I calculate temperature, energy, average pressure, number of particles within the surface or pores and average density profiles inside and outside the pore to ensure equilibration. Once equilibrium has been achieved, the results from the last 10 ns are averaged for the final analysis.

Table 5.1: Composition of three models with various pore widths and their associated carbon densities

	Water	Carbon not in -C=O	Carbon in -C=O	Oxygen in -C=O	Carbon density, Atoms per nm^3
Activated Kerogen Model - all three pores	8962	2474	40	40	40
Inactivated Kerogen Model - 0.9 nm	8650	2514	N/A	N/A	40
Inactivated Kerogen Model - 1.2 and 1.6 nm	8962	2514	N/A	N/A	40
Graphite Slit Model - all three pores	5002	3672	N/A	N/A	114

5.2 Results

The final configurations for the pore sizes of 0.9 nm, 1.2 nm and 1.6 nm are reported in Figure 5.1a-c for the activated kerogen model, in Figure 5.2a-c for inactivated kerogen model and in Figure 5.3a-c for graphite slit pore model respectively. Water is shown with red and white dots and all other colors are the same as in Figure 3.3. The corresponding fluid density profiles across the width of the pore are plotted in Figures 5.1d-f, 5.2d-f and 5.3d-f where the first water layers are highlighted with shaded grey color and the second layers with a striped pattern. The density profiles are computed from the top of the topmost pore wall to the bottom of the lower pore wall and represent the averaged water density over the entire length of the pore surface.

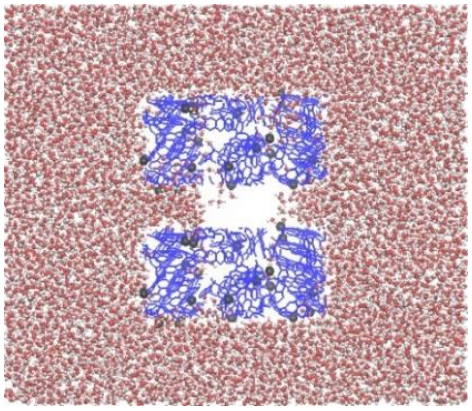

a) Fluid distribution in 0.9 nm pore

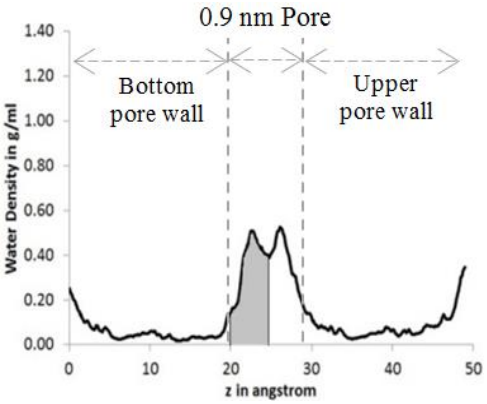

d) Density for 0.9 nm pore

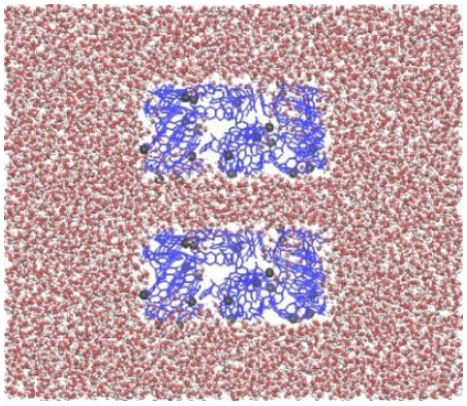

b) Fluid distribution in 1.2 nm pore

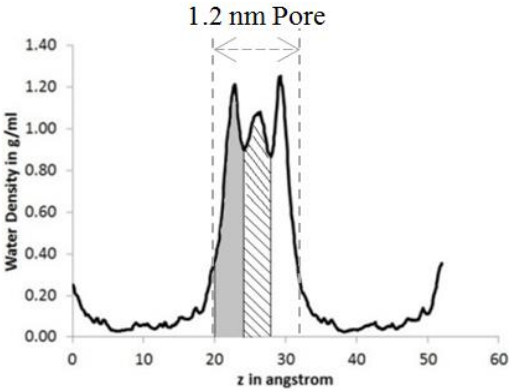

e) Density for 1.2 nm pore

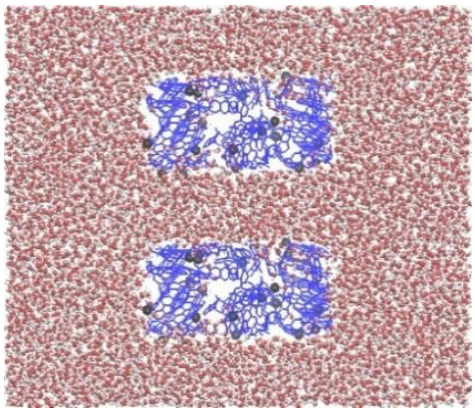

c) Fluid distribution in 1.6 nm pore

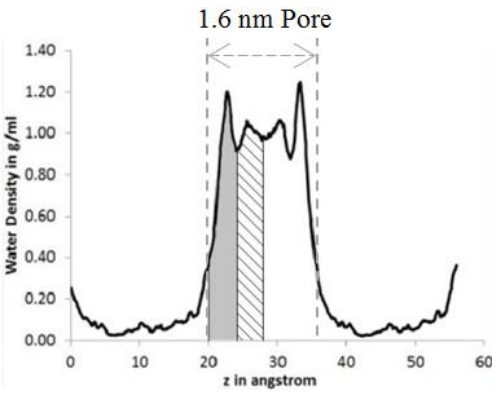

f) Density for 1.6 nm pore

Figure 5.1: a - c are the final configurations for the activated kerogen pores. d - f are the corresponding densities of water across the width of the pore

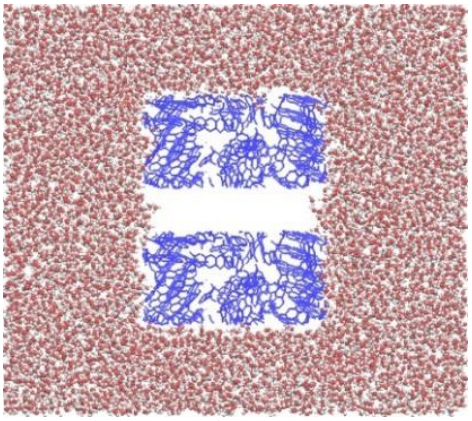

a) Fluid distribution in 0.9 nm pore

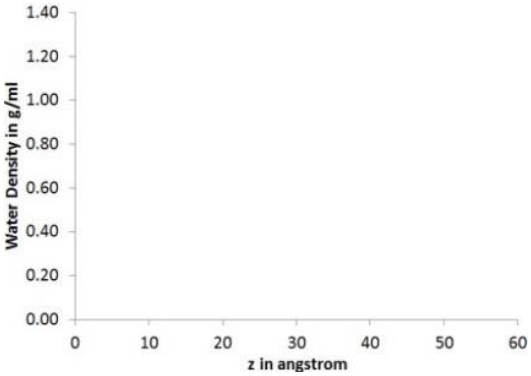

d) Density for 0.9 nm pore

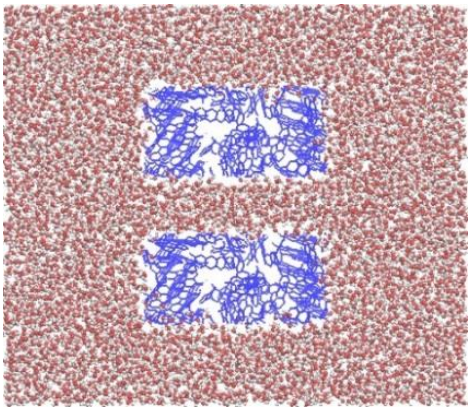

b) Fluid distribution in 1.2 nm pore

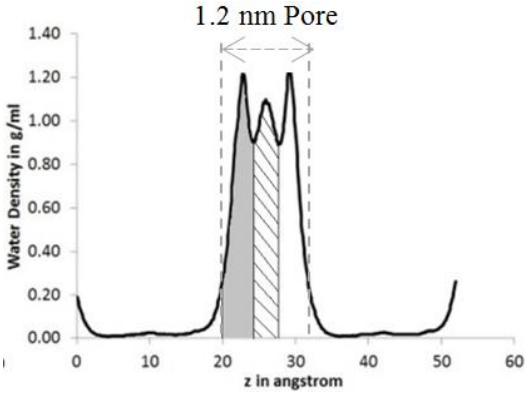

e) Density for 1.2 nm pore

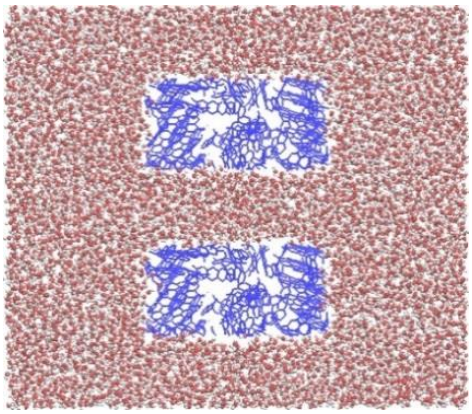

c) Fluid distribution in 1.6 nm pore

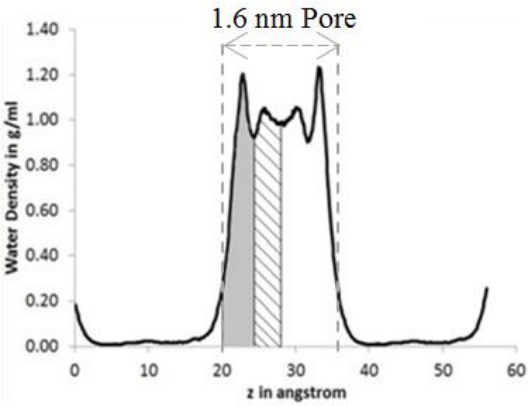

f) Density for 1.6 nm pore

Figure 5.2: a - c are the final configurations for the inactivated kerogen pores. d - f are the corresponding densities of water across the width of the pore

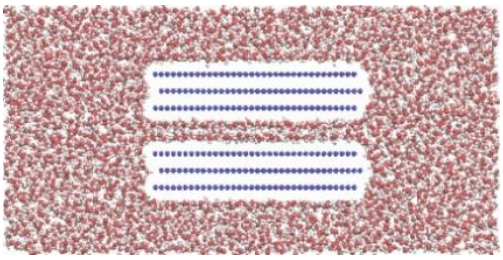

a) Fluid distribution in 0.9 nm pore

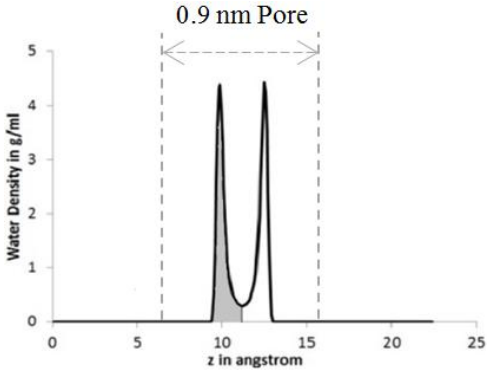

d) Density for 0.9 nm pore

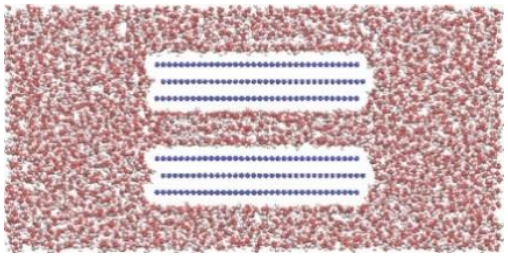

b) Fluid distribution in 1.2 nm pore

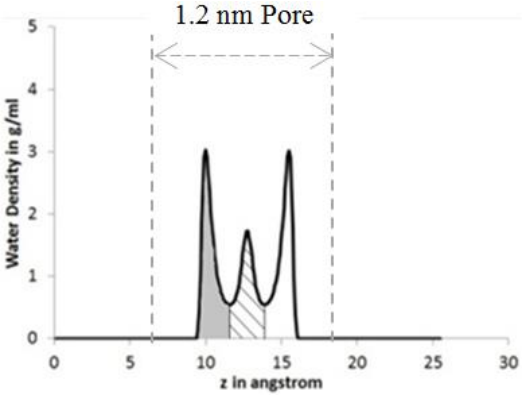

e) Density for 1.2 nm pore

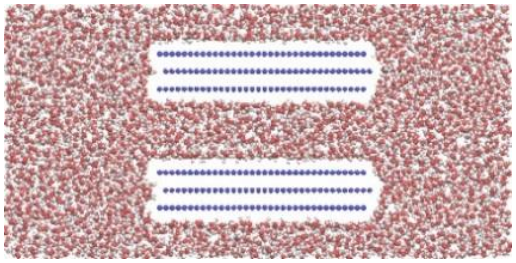

c) Fluid distribution in 1.6 nm pore

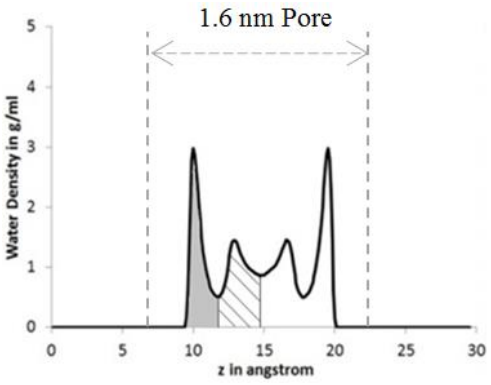

f) Density for 1.6 nm pore

Figure 5.3: a - c are the final configurations for the graphite slit pores. d - f are the corresponding densities of water across the width of the pore

5.2.1 Pore Filling Effect

The simulation results indicate that for the larger pores of 1.2 nm and 1.6 nm, water molecules penetrate the pores at 300 K (80°F) and 200 bar (2901 psi), regardless of the pore wall material and pore surface geometry. The water within these larger pores is in the liquid phase with peaks in the density profiles occurring due to adsorption of water at the pore walls. The results also highlight the asymmetric density profiles present in the kerogen pores in contrast to the more symmetric profiles of the graphene slit pore. This is simply a consequence of the irregular, non-planar structure of the pore models constructed for this study and shown in Figure 3.4.

In contrast, the behavior of water in the 0.9 nm pores is distinctly different. For the 0.9 nm pores, water partially enters the activated kerogen pore (Figure 5.1a and 5.1d), does not enter the inactivated kerogen pore system (Figure 5.2a and 5.2d) while it completely fills the graphite pore (Figure 5.3a and 5.3d). The density profiles of water in these 0.9 nm pores also substantially differ from the corresponding profiles for the 1.2nm and 1.6 nm pores. For the graphite model, the density profile indicates two very prominent adsorption peaks, while in the 0.9 nm activated kerogen pore, water is very likely to be in the vapor phase because partial penetration of water in to the pore leads to a much lower water density. For the inactivated kerogen model, water preferentially remains completely outside of the 0.9 nm pore at a pressure of 300 bar (2901 psia) illustrating the hydrophobicity of highly mature organic kerogen at this pressure. These simulation results indicate that under the same pressure and temperature conditions, water has different density (phase) and adsorption characteristics depending on pore surface chemistry and pore geometry.

This phenomenon of complete pore filling is related to the relative strength of adsorbent-adsorbate and adsorbate-adsorbate interactions (Striolo et al. 2003). The adsorbent in this study is the pore wall while the adsorbate is water. The results obtained with the graphite model are consistent with Chialvo and Cummings (2011) in which pure water filled the graphite slit pores with widths larger than 0.7 nm at ambient conditions and no water entered the pore when the width was reduced to 0.6 nm or less.

As the pore becomes smaller, the pressure required to support the pore filling phenomenon decreases (Striolo et al. 2003) enabling easier access of the fluid molecules to the pore volume. However, pore filling transitions to pore emptying at pore widths smaller than a threshold distance. This is observed in the case of the 0.9 nm inactivated kerogen model of Figures 5.2a and 5.2d. Generally, the theory behind the pore emptying phenomenon is related to the distortion of the tetrahedral hydrogen bonded network of liquid water due to the influence of the pore walls and therefore much higher pressures are required to fill the pores (Striolo et al. 2003, Giovambattista et al. 2007). In my case, the difference of results for all three pores of 0.9 nm width is related to the carbon density and the density of oxygenated groups. The lower carbon density of the inactivated kerogen models (shown in Table 5.1) likely results in weaker water-pore wall interactions contributing to the need for a very large liquid entry pressure. In contrast, pore filling occurs for the 0.9 nm graphite slit pore while for the 0.9 nm activated kerogen pore, the water density profiles suggest an intermediate state created by a balance of forces: the attractive forces between the activated surface sites and water, and forces for pore filling created by the kerogen body. This behavior is also indicated in Brennan et al. (2002) where adsorption isotherms were studied for a porous carbon model with various

densities of the activated sites and the amount of water adsorption was shown to increase with the density of activated surface sites. Hence, these quantitative results depend not only on carbon density, but also on the density of oxygenated groups, because these polar groups can form hydrogen bonds with water. It seems that the kerogen surfaces increases the threshold pore width below which pore emptying occurs leading to negligible water adsorption inside the pore compared to using graphite slit pore model. It is likely that in addition to the carbon density and density of surface activation sites, the surface geometry may play a role in impacting the pressure values required for fluid entry. In fact, the work of Palmer and Gubbins (2012) on the development of realistic models for activated carbons has shown that the predictions regarding the fluid behavior in carbon-based materials strongly depend on the model implemented for the adsorbent material.

Experimentally, significant water adsorption due to pore filling effect was reported for activated carbon nanopores (Kaneko et al. 1999, Alcañiz-Monge et al. 2002, Kimura et al. 2004) and for nanoporous hydrophobic solids (Ohba et al. 2005, Cailliez et al. 2008). It is possible that immature shales and shales within the oil window may be characterized by considerable water storage within the organic pore networks of the kerogen. The observations in Figures 5.1 and 5.2 also indicate that water may enter organic pore networks at low pore pressures following an initial period of depletion.

5.2.2 Influence of Surface Roughness on Water Adsorption

The impact of the pore surface on water adsorption causes differences in the density profiles for water shown in Figures 5.1d-f, Figures 5.2d-f and Figures 5.3d-f for the activated kerogen pores, the inactivated kerogen cases and the graphite slit pores

respectively. These plots provide water density profiles calculated across the simulation box in the vertical direction from the bottom pore wall to the upper pore wall. The different regions of the pore are labeled in each figure. The figures show well defined water layers for different pore widths with slight deviations from symmetric profiles occurring for the kerogen pore models. When pore filling occurs in the 1.2 nm and 1.6 nm pores of Figures 5.1, 5.2 and 5.3, the number of high-density layers of water does not seem to change irrespective of the pore surface geometry and degree of surface activation. For the 1.2 nm pores, the 3 distinct peaks in Figures 5.1e, 5.2e and 5.3e indicate that the water molecules arrange themselves in 3 layers with the layers adjacent to the pore walls exhibiting a higher density due to packing on the pore walls. For the 1.6 nm pores, 4 layers are formed with two high density layers adjacent to the pore walls.

However, there are some key differences in the density profiles depending on the surface material and surface roughness; in particular, the ratios of the high density layers at the pore walls to the density of the fluid layers in the center of the pores. In graphite slit pores, as seen in Figure 5.3, this ratio is substantial, while the density profiles are more uniform across the width of the pore for the kerogen pores of Figures 5.1 and 5.2. This is related to surface roughness, and perhaps also to the carbon density in the pore walls. Note that the density of carbon atoms at the pore surface is related to the strength of the water-carbon interactions. As illustrated in Table 5.1, the carbon density in kerogen models is much lower than that on the graphite slit pore model. The much lower carbon densities in the kerogen models yield weaker effective attractive interactions between water molecules and pores, resulting in less prominent water layers close to the pore walls. Surface roughness is thought to be responsible for the more uniform distribution

of water molecules within the kerogen model pores. Surface roughness and surface asperities lead to additional pore volume that the water molecules can access as seen in Figure 5.1e-f and Figure 5.2e-f, where the equilibrium density of water is non-zero within the kerogen body. To emphasize the impact of surface roughness, we calculate the water density profiles over successive 1 nm-wide windows across the entire pore length as shown in Figure 5.4 for the 1.2 nm inactivated kerogen pore. The different density profiles suggest a dependence of the local density on the surface structure which may be locally smooth or may have asperities.

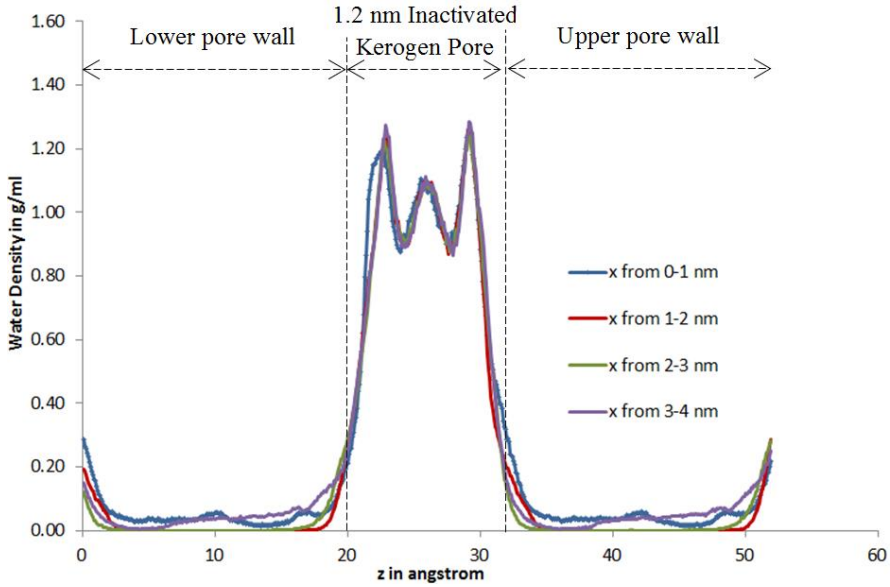

Figure 5.4: Water density profiles calculated with successive 1 nm-wide windows across the length of the pore for a 1.2 nm inactivated kerogen model

The number of water molecules stored per unit length in each of the layers of Figures 5.1d-f, 5.2d-f and 5.3d-f is also calculated to quantify the amount of adsorption. The results are shown in Figure 5.5. In the graphite pore model, adsorption in the first layer exceeds the amount adsorbed in the second layer irrespective of the pore width. In

the case where substantial surface roughness is present, surface roughness diminishes the amount of water adsorbed in the first layer, while there is little to no impact on the amount adsorbed in the second layer. This is observed across all kerogen pore widths irrespective of whether activated or not. The low value for the first layer adsorption within the 0.9 nm activated kerogen model in Figure 5.5 is due to the fact that this pore is only partially filled, as illustrated in Figure 5.1a. Although this study focuses on the distribution of water, in a previous study (Hu et al. 2013c), we demonstrated similar reduction in adsorbed volumes of octane in layers adjacent to the pore wall when pore roughness is present.

The water density profiles (Figure 5.1d-f, Figure 5.2d-f and Figure 5.3d-f) and the adsorption quantified in Figure 5.5 provide some evidence of multilayer adsorption. Even though validity of the monolayer Langmuir adsorption model (Langmuir, 1916) needs further study about the adsorption-desorption processes, the observation may indicate the deficiency of it in nano scaled kerogen pores. For shale gas reservoirs, the invalidity of the Langmuir isotherm when the pore filling phenomena were present was previously reported in Chen et al. (2013) and Li et al. (2013).

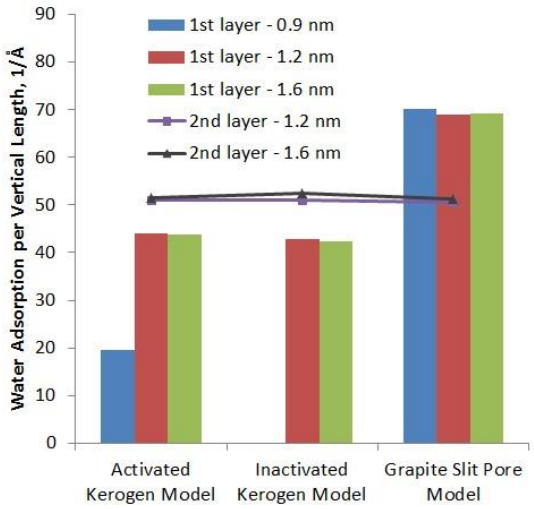

Figure 5.5: Water adsorption per vertical length in 1st and 2nd layers, 1/ Å

5.2.3 The Role of Kerogen Maturity on Water Uptake

In this section, the role of maturity quantified by O/C ratios on water uptake in kerogen bodies and the organic pores is reviewed. In the case of the activated kerogen which serves as a proxy for kerogen in shales of moderate maturity, water molecules are seen to diffuse into the porous space around the oxygenated surface sites. This occurs because of the hydrogen bonds that can form between water molecules and the oxygenated sites within the kerogen, as shown in Figure 5.6. A randomly chosen surface activation site is shown in green and 3 water molecules are observed, shown in yellow and white, surrounding this site. The observation that not significant amounts of water molecules accumulate around the active sites could be a consequence of the sparse distribution of functionalized groups and very narrow porous volume inside the kerogen body considered in these simulations.

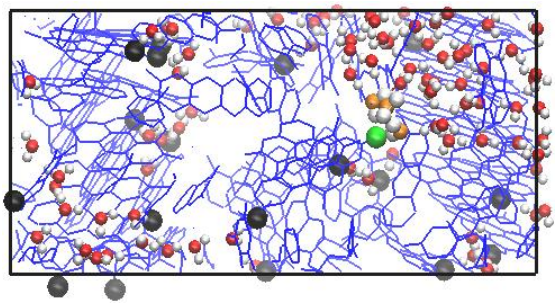

a) Side view

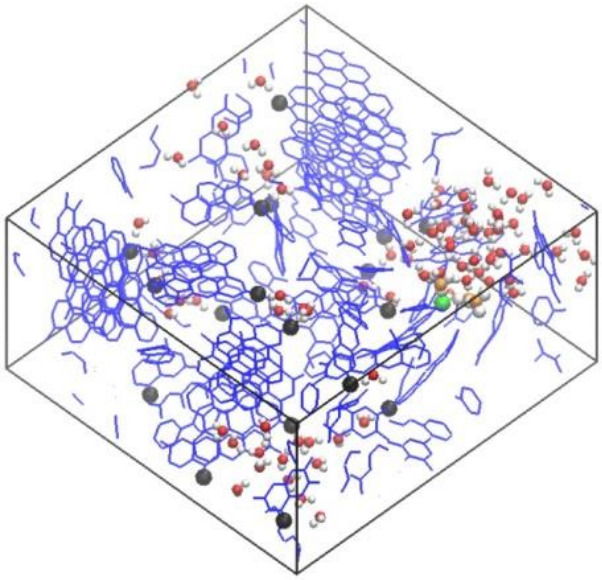

b) Overall 3D view

Figure 5.6: Water uptake in activated kerogen materials

For highly mature kerogen characterized by very small O/C ratios, water uptake is only restricted to a few large nano-cracks around the borders of the kerogen as shown in Figure 5.2a-c. For the graphite cases in Figure 5.3a-c, it would be impossible to uptake any water. What this signifies is that water may be present even within the kerogen body and diffusion of water in to kerogen may be a mechanism for storage of water, either following hydraulic fracturing or during the depositional process and subsequent maturation of the shale.

Figure 5.7 provides the average number of water molecules found within the kerogen body as well as in the pore space during the course of the simulations. The results are used to quantify the influence of kerogen maturity on water uptake. For the O/C ratio of 1.6%, Figure 5.7a shows that water uptake in the activated kerogen model is about twice as much as that within the inactivated kerogen. These differences are solely the consequence of the amount of oxygenated functional groups and their corresponding distribution in the material. Although a low O/C ratio is adopted in this study, it is likely that for shales within the oil window with O/C ratios as high as 10% (Vandenbroucke et al. 2007), the amount of water that can be stored within the kerogen will be substantially more. For the inactivated kerogen model, the smaller amount of water uptake found in some nano-cracks near the surfaces is mainly due to the effect of surface roughness. This surface effect leads to wider effective pore widths in kerogen models than in the graphite pores. As can be seen in Figure 5.1a-c and Figure 5.2a-c, the water density have wider non-zero regions than the nominal pore widths. As a result, when pore filling occurs in the 1.2nm and 1.6 nm pores, the water stored in the activated and inactivated kerogen model is higher than that in the graphite pore, shown in Figure 5.7b.

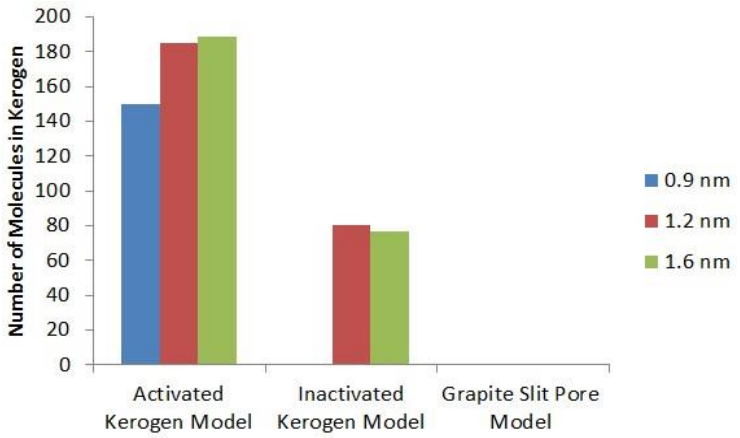

a) Total number of water molecules in kerogen

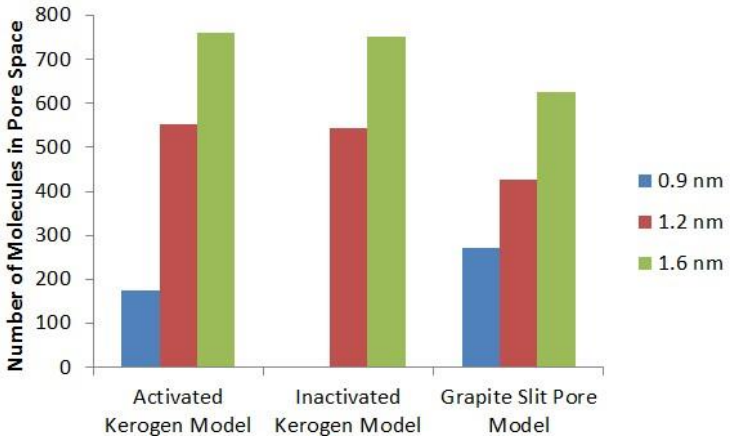

b) Total number of water molecules in pore space

Figure 5.7: Total number of water molecules (a) in kerogen and **(b) in pore space for various systems**

The presence of water uptake in kerogen indicates that water may enter organic pores when surface activation sites are present. This phenomenon is likely to be a function of the density of the activated sites and is likely to impact transport of fluids at the nanoscale and thereby influence relative permeability, capillary pressure curves, water mobility and hydrocarbon-in-place estimates.

5.3 Conclusion

This chapter emphasizes the influence of pore sizes, surface roughness and the degree of kerogen maturity on the behavior of water in organic nanopores. Some of the key findings from this work are provided below:

1. Complex kerogen structure strongly influences the behavior of water, when compared to the results of planar graphite slit-pore systems. These create conditions for

different mechanisms of water entrapment, differing amounts of adsorption and uptake of water by the pore body.

2. The degree of surface activation that represents kerogen maturity has a considerable impact on interactions between water and kerogen pore walls. This may result in trapping of water in the organic matter, and may partially explain the low recovery of hydraulic fracture water during well clean-up. Similar observation was also reported in a model of active carbons (Brennan et al. 2002).

CHAPTER 6

THE DYNAMICS OF HYDRAULIC FRACTURE WATER IN SHALE NANO-PORES

Field operations of hydraulic fracture treatment have some common observations including poor recovery of hydraulic fracture water and the progressive increases in produced water salinity. Although there have been some attempts to address these phenomena, the associated theories are lacking in scientific rigor. The purpose of this study is to provide some fundamental insights into the above issues and reveal the potential trapping mechanisms for hydraulic fracture water.

In Chapter 5, the distribution of pure water is analyzed. However, the fresh water injected for the hydraulic fracturing treatment also contains a limited amount of salt. To better represent the hydraulic fracture water, brine water should be studied.

This chapter extends the Chapter 5, and focues on describing the distribution of saline water in organic and inorganic pores as a function of pore size and pore morphology. To simplify the system, the selected saline solution is the NaCl aqueous solution. The results imply that introducing electrolytes into the water system does not affect the water dynamics in various pores and the distribution of ions depends on the chemistry of the surface material.

6.1 Modeling of Inorganic Matters in Shale

Realistic inorganic materials in shale are very challenging to model because of the heterogeneity in mineralogy. Inorganic material in shales may occur due to the presence

of silica, carbonates, various clays such as illite, smectite, kaolinite and also due to the presence of other minerals such as pyrite. Largely because of the presence of these clays, their different structural elements, surface areas and cation-exchange capacities, it remains very challenging to represent this level of heterogeneity and to model their interactions.

To simplify the problem, magnesium oxide (MgO) crystals is used to represent inorganic materials. As a fundamental constituent of several minerals found in the subsurface, the MgO itself is an inorganic material and is relatively easy to analyze. For some ultramafic rock types (Wyllie 1970), such as dunite, MgO concentrations are more than 40%. For pure dolomite (i.e. calcium magnesium carbonate), the amount of MgO is as high as 22%. Additionally, MgO possesses similar wetting properties to materials that constitute the inorganic material in shales. Consequently, as a basis for comparison with organic materials, MgO serves as a reasonable first-order approximation to inorganic pores.

The structure of the MgO crystal is a face-centered cubic with magnesium (silver color), and oxygen (purple color) atoms alternate with each other, as is shown in Figure 6.1. The distance between magnesium and oxygen atoms is 0.21 nm. The dimension of the simulation box is 4.205 nm by 4.205 nm by 1.2615 nm.

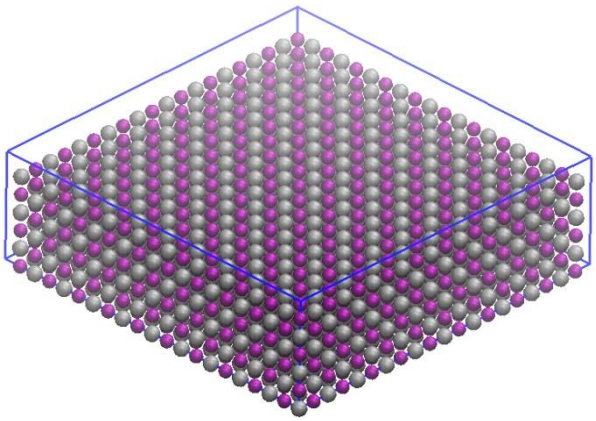

Figure 6.1: Crystal structure of magnesium oxide

6.2 System configuration & initialization

This work considers 3 pore sizes of 0.9 nm, 1.2 nm and 1.6 nm. Each pore is centered in the simulation box with the overall lengths listed in Table 6.1. For the initial configuration, water and NaCl ions are placed outside of the pores, as shown in Figure 6.2. The composition of the simulated systems with three pore widths is illustrated in Table 6.2 for kerogen pores and Table 6.3 for MgO systems. The specified number of molecules is chosen to render liquid properties outside of the pore at equilibrium state consistent with the corresponding properties in the bulk. The ionic concentration is almost the same (1.95 – 1.96 M) which makes the results comparable to each other as the pore sizes and surface materials change. Although, the specified NaCl salinity is much higher than typical hydraulic fracture water treatments, statistical bias arising from the use of a small number of molecules may bias the interpretation and consequently, a higher salinity is chosen.

Table 6.1: Dimensions of simulation boxes for various organic and inorganic pores

	x, nm	y, nm	z, nm
Organic - Inactivated Kerogen Model	10	3.87	8.6
Inorganic - MgO Crystal Model	9.995	4.205	7.702

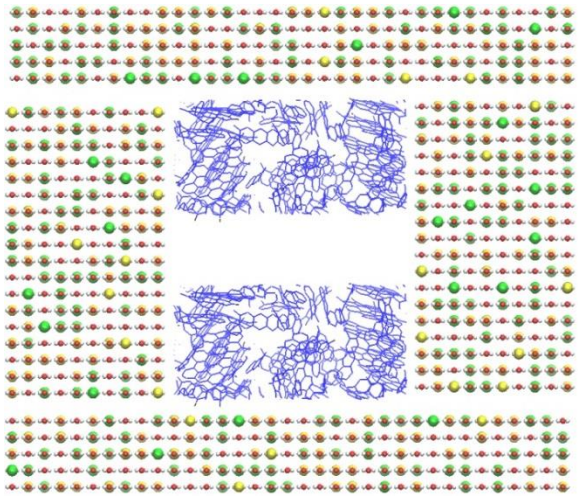

a) 1.2 nm Inactivated kerogen pore

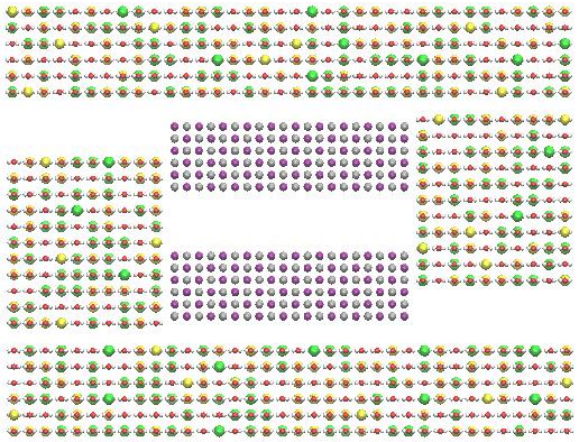

b) 1.2 nm MgO pore

Figure 6.2: Orthographic illustrations of the initial system configurations for both inactivated kerogen and MgO pores. Pore widths are 1.2 nm

Table 6.2: Composition of the kerogen systems for different pore sizes

	Number of Molecules				Ionic Strength	
	Water	Na^+	Cl^-	Carbon	Unit in Molarity	Unit in gram/liter
0.9 nm	8602	301	301	2514	1.953	114.142
1.2 nm	8602	301	301	2514	1.953	114.142
1.6 nm	8504	298	298	2514	1.956	114.307

Table 6.3: Composition of the MgO systems for different pore sizes

	Number of Molecules				Ionic Strength	
	Water	Na^+	Cl^-	MgO	Unit in Molarity	Unit in gram/liter
0.9 nm	8530	299	299	2400	1.957	114.341
1.2 nm	8530	299	299	2400	1.957	114.341
1.6 nm	8504	298	298	2400	1.956	114.307

For all the simulations, both canonical ensemble (NVT) and isothermal-isobaric ensemble (NPT) are conducted. The temperature is maintained at 300 K (80 oF) using the Nose-Hoover thermostat and the pressure is controlled at 200 bars (2901 psi) by the Berendsen weak coupling method. The total simulation time is 63 ns for each organic

pore case and is 133 ns for each inorganic simulation. The first 5 ns are for NVT running to start the simulation. The next 8 ns are run with NPT to control the pressure. Then, a 50 ns NVT is conducted in the final step until the system equilibrium is reached for organic systems and a 120 ns NVT is conducted for the inorganic systems. The results of the last 10 ns of the 50 ns NVT steps are used for data analysis in organic pores, while the last 20 ns of the 120 ns are used for the inorganic ones. During the simulation, the pore walls are fixed, but water molecules are allowed to move dynamically.

Criteria for equilibration included constant temperature and pressure, constant energy, and constant averaged density profiles inside and outside the pore. Kalluri et al. (2011) report a strong influence of the pore wall on the fluids up to a distance of 1-1.5 nm from the pore wall. Therefore the bulk region in this thesis is defined as the volume outside the pore located more than 1.5 nm away from the kerogen bodies. When the system is stable, the influence of the pore wall on the properties of fluid in the bulk regions is negligible and hence this region is meant to replicate the bulk properties. Hence, in addition to above criteria, I also check the density of water in the bulk region and the results are consistent with experiments.

6.3 Results

6.3.1 Hydraulic fracture water distribution

Initially water and NaCl ions are located outside of the pores. During the simulations, the electrolyte solution enters the pores following inter- and intra- molecular interactions. The final equilibrated states for inactivated and activated kerogen systems, and inorganic pores are described in Figure 6.3, 6.4 and 6.5 respectively. Color representations of surfaces are exactly the same as in Figure 3.3 and 6.1. Oxygen and hydrogen atoms in

water molecules are demonstrated in red and white. Yellow and green balls are for sodium and chloride ions.

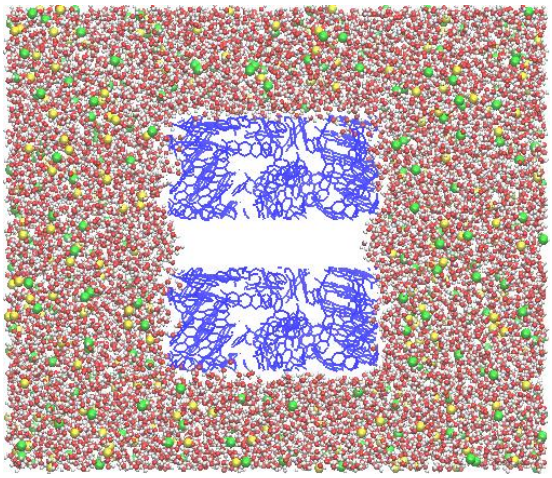

a) 0.9 nm inactivated kerogen pore

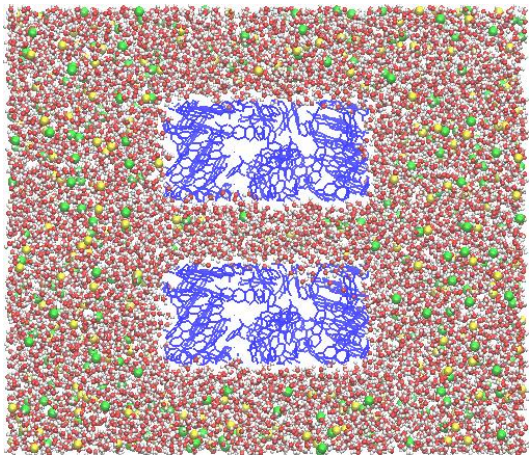

b) 1.2 nm inactivated kerogen pore

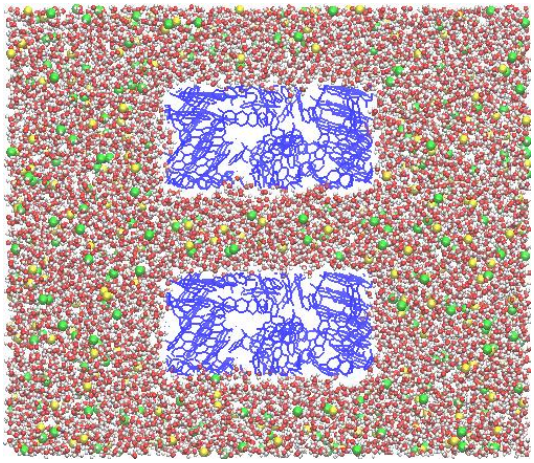

c) 1.6 nm inactivated kerogen pore

Figure 6.3: Snapshots of final configurations for the inactivated kerogen pores of different sizes

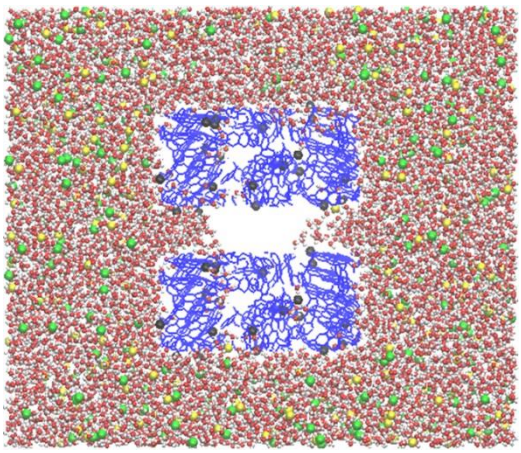

a) 0.9 nm activated kerogen pore

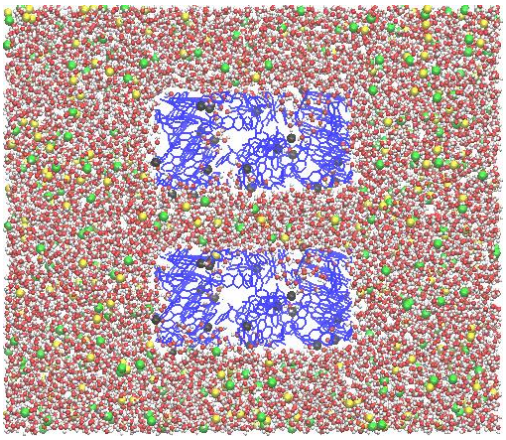

b) 1.2 nm activated kerogen pore

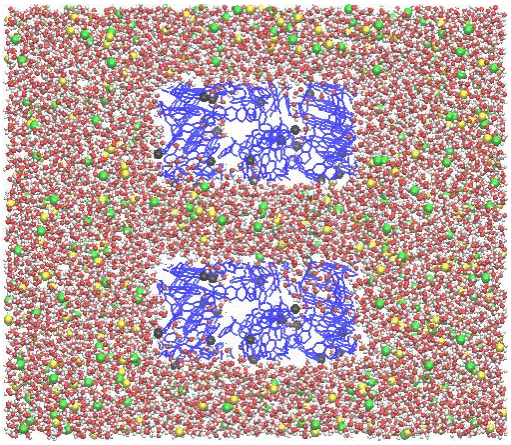

c) 1.6 nm activated kerogen pore

Figure 6.4: Snapshots of final configurations for the activated kerogen pores of different sizes

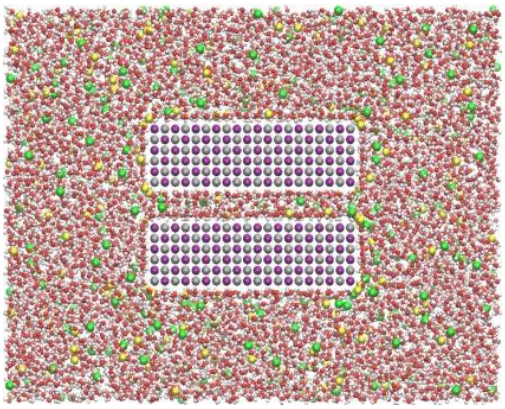

a) 0.9 nm MgO pore

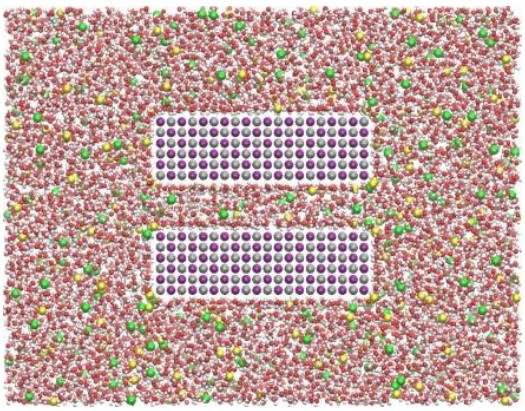

b) 1.2 nm MgO pore

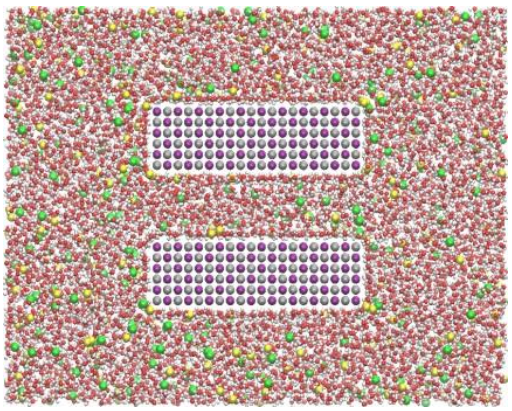

c) 1.6 nm MgO pore

Figure 6.5: Snapshots of final configurations for the crystal MgO pores of different sizes

The water distribution in the organic pores is very similar to the pure water study in Chapter 5. For the 0.9 nm pore width, water molecules only partially enter the activated kerogen pore, while pore emptying is observed in the inactivated kerogen system. For larger pores, the complete pore filling is observed. In addition, one thing worth mentioning in activated kerogen pores is that there exist some water molecules inside the kerogen material itself, regardless of pore sizes. The possible mechanisms for these phenomena have been discussed in previous chapter and is omitted here to save space.

For various inorganic (MgO) pores, the pore emptying-like phenomenon is no longer observed. The reason is because that MgO is characterized by polar groups on the hydrophilic surfaces. Hence, extensive hydrogen bonds are formed near the surfaces, and the water molecules are expected to fill all the studied MgO pores. In Figure 6.5, water density is the greatest near the MgO surfaces and a clear preferred water orientation (formation of hydrogen bonds due to fluid-solid interaction) denoted by an obvious "red ring" around the MgO surfaces is formed where oxygen atom in water are represented in red. This ring is not observed in the previously studied kerogen pores due to the fact that hydrophobic surfaces are non-polar materials and they are not capable of forming hydrogen bonds with water molecules.

6.3.2 Distribution of Ions in Organic and Inorganic Pore Models

The average number of water molecules and electrolyte within the kerogen pore surfaces and the pores are presented in Table 6.4. For a fixed pore width, the number of molecules stored in the top and bottom activated kerogen surfaces at the equilibrium state are approximately identical to each other with the exception of the 0.9 nm pore. In the 0.9 nm pore, the surface differences are mainly due to the fact that the pore does not allow sufficient uptake of water and the pore is only partially filled. As the pore size increases from 0.9 nm to 1.2 nm, more water molecules diffuse into the surfaces along with a few electrolyte ions. When pore filling occurs, the storage capacities of the kerogen body becomes almost constant as illustrated by the amount within surfaces of the 1.2 nm and 1.6 nm pores in Table 6.4. The sodium ions are preferentially adsorbed in comparison to the chlorides because of the attraction between the negatively charged surface oxygen

and the cations. The relatively low numbers of sodium ions in the bottom surface for the 1.6 nm pore indicates the possibility that there is a competition with water for adsorbing to the activated sites, and also could be due to ion hydration forces and ion-surface oxygen interaction.

Within the pores itself, as pore sizes increase, there is a corresponding increase in the number of water molecules and electrolytes. With the small O/C ratio in the activated kerogen pore model, no significant change in the storage of water is observed in comparison to the inactivated one (see Table 6.4), which indicates that the effect of the surface activation on the water adsorption in the pore is somewhat negligible and may become insignificant in larger pores.

Table 6.4: Average number of molecules in the water and ions systems for two kerogen models with different pore sizes

Number of molecules		Activated Kerogen Systems			Inactivated Kerogen Systems	
		0.9 nm	1.2 nm	1.6 nm	1.2 nm	1.6 nm
Top Surface	Water	78.71	93.6	92.62	39.58	36.9
	Sodium	0.34	0.8	0.86	0.04	0.04
	Chloride	0.08	0.12	0.1	0.04	0.02
Bottom Surface	Water	68.67	94.2	91.97	39.28	36.2
	Sodium	0.3	0.83	0.34	0.03	0.02
	Chloride	0.05	0.09	0.06	0.02	0.02
Pore	Water	146.72	538.44	732.31	528	729
	Sodium	1.06	13.14	21.68	7.85	17.4
	Chloride	0.8	13.69	22.37	8.02	17.1

To quantify the distribution of electrolytes between the pore and bulk volume, the partition coefficient Γ is calculated which is defined as the ratio of ionic concentration in the pore to that in the bulk. Equation (13) shows how the partitioning coefficient is computed. In this study, since the diffusion of water into the kerogen surfaces occurs,

determination of the number of ion and water outside of the pore does not include the amount stored in the kerogen body and is formulated in equation (14).

$$\Gamma = \frac{C_{pore}}{C_{bulk}} = \frac{\frac{N_{ion\ in\ pore}}{N_{water\ in\ pore}}}{\frac{N_{ion\ outside\ pore}}{N_{water\ outside\ pore}}} \tag{13}$$

$$N_{ion\ or\ water\ outside\ pore} = N_{total\ number\ of\ ion\ or\ water} - N_{ion\ or\ water\ in\ surfaces} - N_{ion\ or\ water\ in\ pore} \tag{14}$$

The average partition coefficients of Na^+ and Cl^- ions are provided in Table 6.5. All the partition coefficients are less than unity which indicates that ions prefer to stay in the bulk regions exterior to the pore. The values of the partition coefficients could depend on the planar size of the pore surfaces since more ions are likely to be attracted to pores with a larger surface area which may result in a higher partition coefficient. This preference is explained by entropy due to the fact that hydrated ions inside the neutral pores have limited free volume accessibility (Kalluri et al. 2011). This explains the observation that as a pore becomes wider, more ions enter the pore as indicated in the Table 6.5. For a 0.9 nm pore, the small partition coefficients are due to the reason that water only partially fills the pore.

Compared with partition coefficients obtained from inactivated kerogen model, there are moderate increases for all the pores considered in this study indicating the influence of ion-surface oxygen interaction. This result is reinforced by comparing the stored number of molecules in Table 6.4, and there is an increase of ion number in the pores when the kerogen surfaces are activated. In both activated and inactivated kerogen case studies, there however is always some amount of water within the kerogen body. Water adsorption in the inactivated surfaces is due to the surface roughness, as water

appears to stay in some large nano-cracks around the borders of the surfaces illustrated in Figure 6.3. With the oxygenated surfaces, water-surface oxygen attraction may play a more important role.

In contrast to the results for a smooth neutrally charged graphene slit pore reported in Kalluri et al. (2011) where a countable amount of ions were found only in the 1.6 nm graphene slit pore, the ionic concentrations in this study for both 0.9 nm and 1.2 nm are significantly higher. Considering the size of the hydrated Na^+ and Cl^- ions (0.72 nm and 0.66 nm respectively), this could be due to the larger excluded volume effect or wider effective pore sizes resulting from surface roughness and ion-surface oxygen interaction in the activated kerogen model since there are some water molecules in nano-cracks within the activated kerogen surfaces.

The influence of hydrophilic pore on the distributions of ions is also reflected in partition coefficients in Table 6.5. Compared to all of the kerogen case studies, there is a significant increase in the number of ions inside the pores, due to the interaction of ions with MgO surfaces and with the obvious water layer near the surfaces. In fact, for larger pore widths of 1.2 nm and 1.6 nm, there is no obvious preference regarding where they would like to stay, which is indicated by unity partition coefficients. For the 0.9 nm pore, even though the pore width is comparable to the hydrated ions, which restricts the entry of ions, the non-zeros values of partition coefficients indicate the strong interaction among ion-water and ion-surface. Interestly, the Γ value of the Na^+ for the 1.6 nm MgO pore is slightly smaller than that in the 1.2 nm pore. This could be possibly because the number of Na^+ attracted into a relatively larger pore is largely restricted to the water layers closest to the wall surfaces (Figure 6.5), and the wall surface has a limited adsorption

capacity with a fixed surface area. This study therefore shows that hydrophilic surfaces not only create ideal conditions for water adsorption close to the surface, but also influences the ion distributions due to the combined effect of ion-surface, ion-water and ion-ion interactions. In realistic clay in shales, due to the negative charges on the clay layers, shales are reported to be permeable to the Na^+ but impervious to the Cl^- (Peters 2012). Even though the results from this study do not indicate the stronger transport ability of Na^+ than Cl^- in MgO, the study reveals that the surface materials have a great impact on the dynamics of ions as a result of the ion-surface, ion-water and ion-ion correlations.

Table 6.5: Average partition coefficients for ions in activated kerogen pores

Pore width, nm	Organic Systems				Inorganic Systems	
	Activated Kerogen		Inactivated Kerogen		MgO	
	Na^+	Cl^-	Na^+	Cl^-	Na^+	Cl^-
0.9	0.2	0.15	N/A	N/A	0.65	0.72
1.2	0.67	0.7	0.4	0.41	1.07	1.08
1.6	0.82	0.84	0.66	0.65	1.02	1.09

6.3.3 Density profiles

Density profiles in the number of molecules per angstrom3 for water and ions are correspondingly shown in Figure 6.6, 6.7, 6.8 for kerogen and the inorganic pores. For kerogen systems, considering that some water molecules also penetrate nano-cracks in

the surface, plots in Figure 6.6 and 6.7 include densities from the bottom to the top kerogen pore walls.

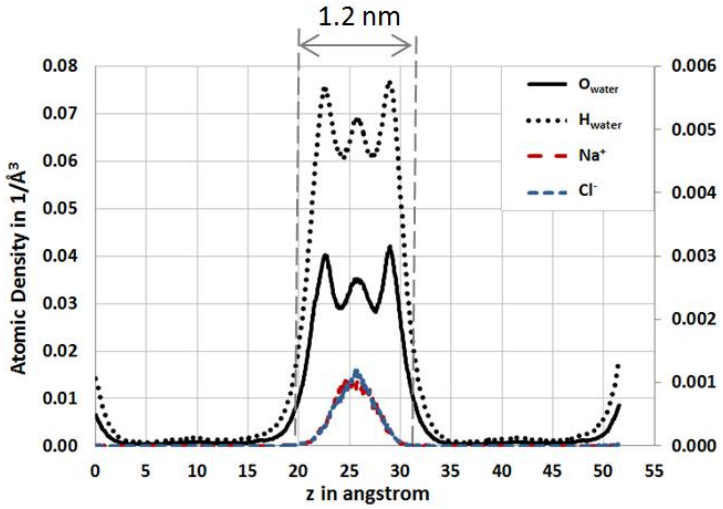

a) 1.2 nm inactivated kerogen pore

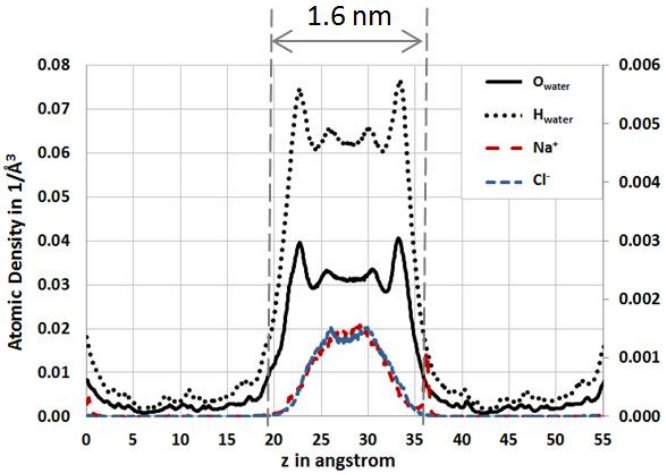

a) 1.6 nm inactivated kerogen pore

Figure 6.6: Atomic density of oxygen (black solid line) and hydrogen (black dotted line) atoms in water molecules, Na^+ (red long dashed line) and Cl^- (blue short dashed line) ions for inactivated kerogen pores. Left and right y-axis represents the density of water molecules and ion atoms, respectively

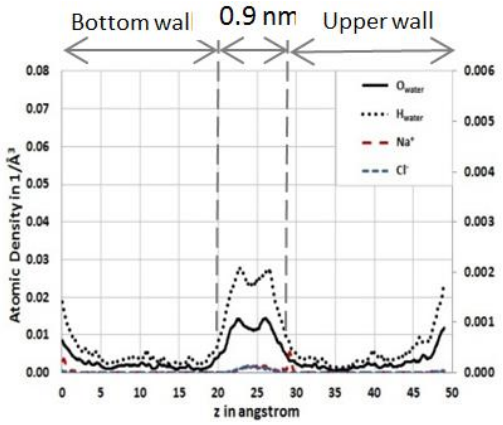

a) 0.9 nm activated kerogen pore

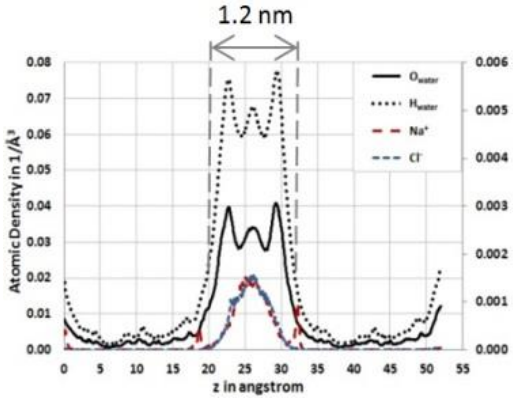

b) 1.2 nm activated kerogen pore

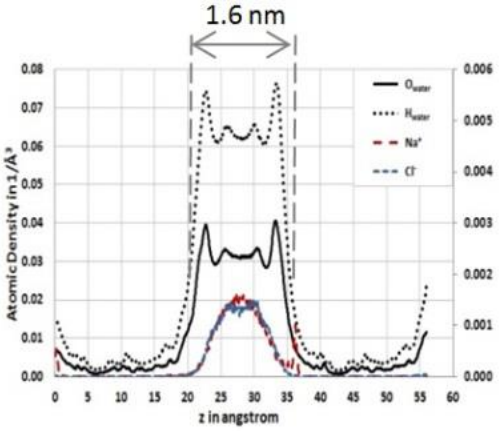

c) 1.6 nm activated kerogen pore

Figure 6.7: Atomic density of oxygen and hydrogen atoms in water molecules, Na^+ and Cl^- ions for activated kerogen pores. Left and right y-axis represents the density of water molecules and ion atoms, respectively

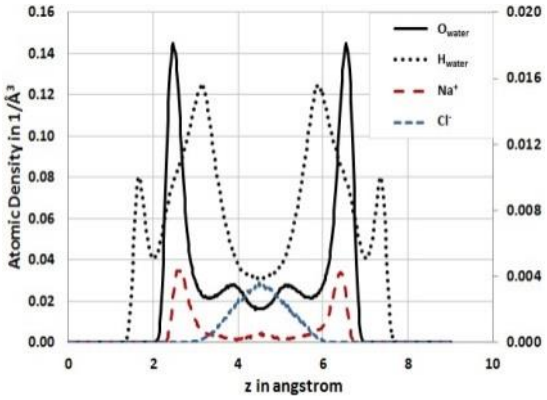

a) 0.9 nm MgO pore

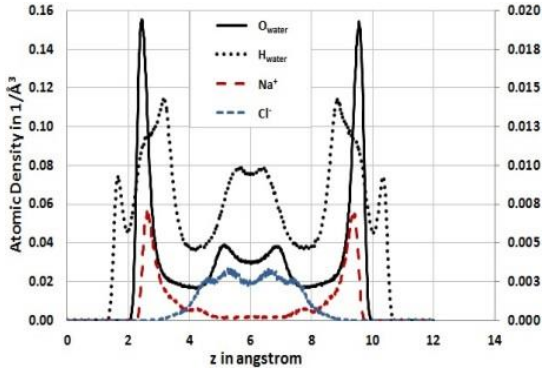

b) 1.2 nm MgO pore

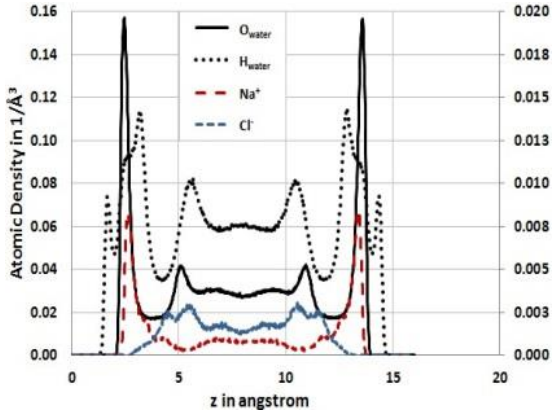

c) 1.6 nm MgO pore

Figure 6.8: Atomic density of oxygen and hydrogen atoms in water molecules, Na^+ and Cl^- ions for MgO pores. Left and right y-axis represents the density of water molecules and ion atoms, respectively

In kerogen pores, when NaCl electrolytes are present, water molecules have the same density profile as the study of pure water in Chapter 5. Regarding the distributions of ions inside the kerogen pores, most of the Na^+ and Cl^- ions accumulate within the center of the pore. The ion density for the 0.9 nm activated pore is significantly lower than in the other ones, which is consistent with the low partition coefficient results. There appears to be a direct relationship among ions and the water layers located in the pore center. This indicates the formation of the hydration shell of attracted water molecules around those ions, as a result of favorable interaction of Na^+ (or Cl^-) ions with oxygen (or hydrogen) atoms of water. In addition, some ionic correlations exist between the density of Na^+ and Cl^-.

For the inorganic pores in Figure 6.8, regardless of pore sizes, water molecules form four layers in the pores. Two of these water layers are due to strong interaction between water and MgO surfaces, leading to prominent, well-defined layers close to the surfaces with sharp density intensities. In Figure 6.5, the "red rings" around the surfaces correspond to these prominent water layers. Another two of the water layers are located near the center of the pore. Since the shape of the hydrogen density is quite different from that of the oxygen density, the water structure or the orientation of the water molecules is very likely to be strongly influenced by the confined MgO pores. There are two hydrogen layers formed around the prominent water layer near each surface. The first layer is made up of a portion of the hydrogen atoms from the well-defined water layers, as these hydrogen atoms are pointing towards the walls. The second hydrogen density peak with a higher intensity is largely formed by the rest of the hydrogen atoms in the same water layer close to each wall, and the remaining hydrogen atoms in these water layers are

pointing away from the surface. The water density profiles are consistent with Phan et al. (2012), in which thin water films in contact with free standing MgO surface was studied.

With respect to the distribution of the ions in the MgO pores, Na^+ seems to have an affinity towards the MgO surfaces, since it is attracted to the negatively charged oxygen in the prominent water layers. Cl^-, by contrast, is pushed towards the pore center, as a result of the repulsive forces interacting with these water layers. In addition, a small amount of Na^+ also accumulates around the center of the pore, because of the ion-ion correlation between Na^+ and Cl^-.

6.4 Conclusion

This paper investigates the dynamics of water molecules and NaCl electrolytes confined in organic and inorganic pores with various widths. Compared with the Chapter 5, this study involves brine water and is more appropriate to describe the distribution of hydraulic fracture water. In addition to the conclusions made in Chapter 5, additional findings include:

1. Surface activation by grafting oxygenated functional groups onto the kerogen material could attract water molecules into the organic matter; hence it could possibly change the wettability property of the organic pores.

2. Water entrapment is possibly not restricted to inorganic pores and water storage could occur in organic pores as well. The combination of these two would prevent flow-back of some hydraulic fracture water.

3. The chemistry of the surface material clearly impacts the distribution of ions. For the kerogen pores, ions generally prefer to stay outside the pores, and only a small

amount enters the pores. By contrast, the inorganic pores have a strong affinity for aqueous NaCl electrolytes.

CHAPTER 7

THE DYNAMICS OF WATER AND HYDROCARBON IN SHALE-KEROGEN PORES OF POTENTIALLY HETEROGENEOUS WETTABILITY

Studies on shale maturity and shale molecular structure indicate the presence of some functional groups associated with oxygen, hydrogen and nitrogen (Vandenbroucke et al. 2007, Facelli et al. 2011). Because of the presence of these polarized groups, our understanding of the wettability of the kerogen surface as purely hydrophobic may be inadequate. We may instead have to consider kerogen characterized by heterogeneous wet surfaces because of the affinity of hydrogen in water molecules to these surface sites.

Even though I have already considered the effect of surface activation in the studies of Chapter 5 and 6, the focus of these chapters was on water entrapment mechanisms in small organic kerogen pores and hence the major fluid in the systems is water. It is however likely that kerogen, because of its relative hydrophobicity, is also associated with the storage of alkanes. Therefore, in this chapter, a more realistic case containing both water and octane molecules is investigated in kerogen pore systems. The dynamics of the mixture enables an understanding of both the activated kerogen model and the water trapping mechanisms when alkanes are present. The results indicate that maturity of the kerogen controls the wettability of organic nanopores and for intermediate maturity such as in liquids-rich shales, organic pore systems may have heterogeneous-wet characteristics.

The material presented in this chapter was accepted to the SPE Journal.

7.1 System configuration & initialization

The model configuration is a large simulation box with a pore located in the center. Because of the size of the simulation box, fluid molecules are not constrained to remain either within the pore or within the kerogen body and therefore a more representative analysis of fluid-pore wall interactions may be achieved. The simulation results of the activated kerogen pore are compared with the inactivated kerogen pores and smooth graphite slit pores having similar planar areas of the organic surfaces and the same pore width of 5 nm. The surface carbons are shown in black and the oxygen atoms in the functional groups as green dots. Hydrogen and oxygen atoms in water molecules are represented by white and purple colors. The octane molecules are shown in yellow. Sizes of the spheres do not reflect real sizes of atoms. Table 7.1 gives the box dimensions for the various 5 nm pores.

Equal amounts of water and octane are used in all studies and the compositions of the different simulated systems are tabulated in Table 7.2. The octane and water molecules are initially placed randomly throughout the simulation box to avoid favoring any particular configuration as shown in Figure 7.1 for the activated kerogen pore as an example. The initial configuration for the inactivated kerogen pore and the graphite slit pore are identical. Carbon atoms in kerogen are shown in blue lines and it is decorated by black oxygen atoms in the functional group. Oxygen and hydrogen atoms of water are shown in red and white; octane molecules are shown in green.

Table 7.1: Dimensions of simulation boxes for water and octane systems in various 5 nm kerogen pores

Models	Dimensions		
	x, nm	y, nm	z, nm
Activated kerogen	12	3.87	9.05
Inactivated kerogen	12	3.87	9.05
Graphite slit pore	12	3.834	7.01

Table 7.2: Composition of the water and octane systems in various 5 nm kerogen pores

Models	Number of molecules				
	Water	Octane	Inactivated Carbon	Activated Carbon	Activated Oxygen
Activated kerogen	1180	1180	2474	40	40
Inactivated kerogen	1180	1180	2514	N/A	N/A
Graphite slit pore	927	927	4284	N/A	N/A

Simulations are conducted with canonical ensemble (NVT) where number of molecules, system volume and temperature are held constant. All studies are run for 35 ns. The last 7.5 ns of each system are used for data analysis. During the simulation,

temperature is maintained at 300K (80oF) by using the Nose-Hoover thermostat with a relaxation time of 100 fs. The final system pressure is around 300 bar (4351 psi). During the simulation, oxygen atoms in functional group and carbon atoms are held stationary. Periodic boundary conditions are applied in three directions.

In order to confirm that the equilibrium fluid distributions are achieved, I check values of temperature, energy, average pressure and average density profiles for water and octane inside and outside the pore to ensure meaningful interpretation. Additionally, octane densities in regions far removed from the pore surfaces are compared with experimentally obtained bulk octane densities. The octane density in the units of number of molecules per angstrom3 in the bulk region surrounding the 5 nm activated kerogen pore is calculated to be 0.0037 which compares well with the experimental result of 0.0038 at the 300K and 300 bar conditions (Lemmon et al. 2005).

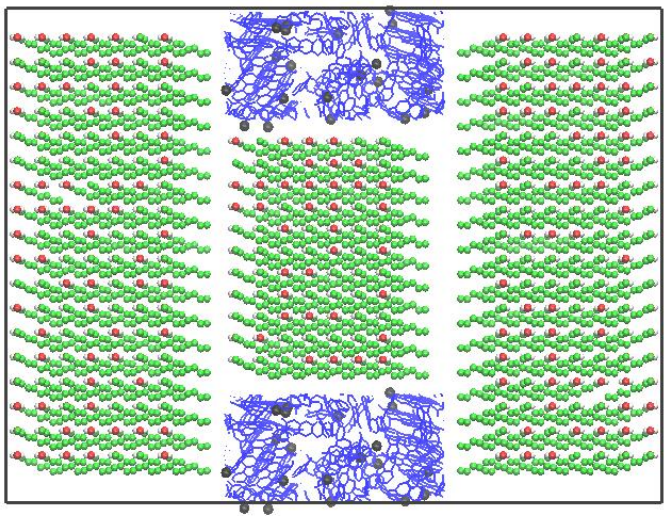

Figure 7.1: An orthographic illustration of the initial system configurations of the water and octane systems for 5 nm activated kerogen pore

7.2 Results

Because kerogen has traditionally been viewed as hydrophobic, a mixture of water and octane molecules is expected to provide an understanding of wettability as a function of surface activation and also investigate water trapping mechanisms in the presence of alkanes. The evolution of water and octane from their initial configuration to their respective final states in a 5nm wide activated kerogen pore is shown in Figure 7.2. The final configuration at the end of the simulation for the 5nm wide activated kerogen pore is shown in Figure 7.3. The corresponding figures for the 5nm wide inactivated kerogen pore are shown in Figures 7.4 and 7.5 while the results for the graphite slit pore are shown in Figures 7.6 and 7.7.

The results indicate that as time progresses during the simulation, water molecules first form small clusters that then group together to create a larger water cluster. Because of the presence of polar activated functional groups in Figures 7.2 and 7.3, the large water cluster is attracted in to the activated kerogen pore while water shows a preference to occupy regions outside the pore in both the inactivated kerogen pore and the graphite slit pore models. The asymmetric pore structure tends to cause imbalances in the final distribution of water in the case of the inactivated kerogen pore. In contrast, when the pore model is symmetric, water distributes itself in a near-symmetric arrangement outside the pore.

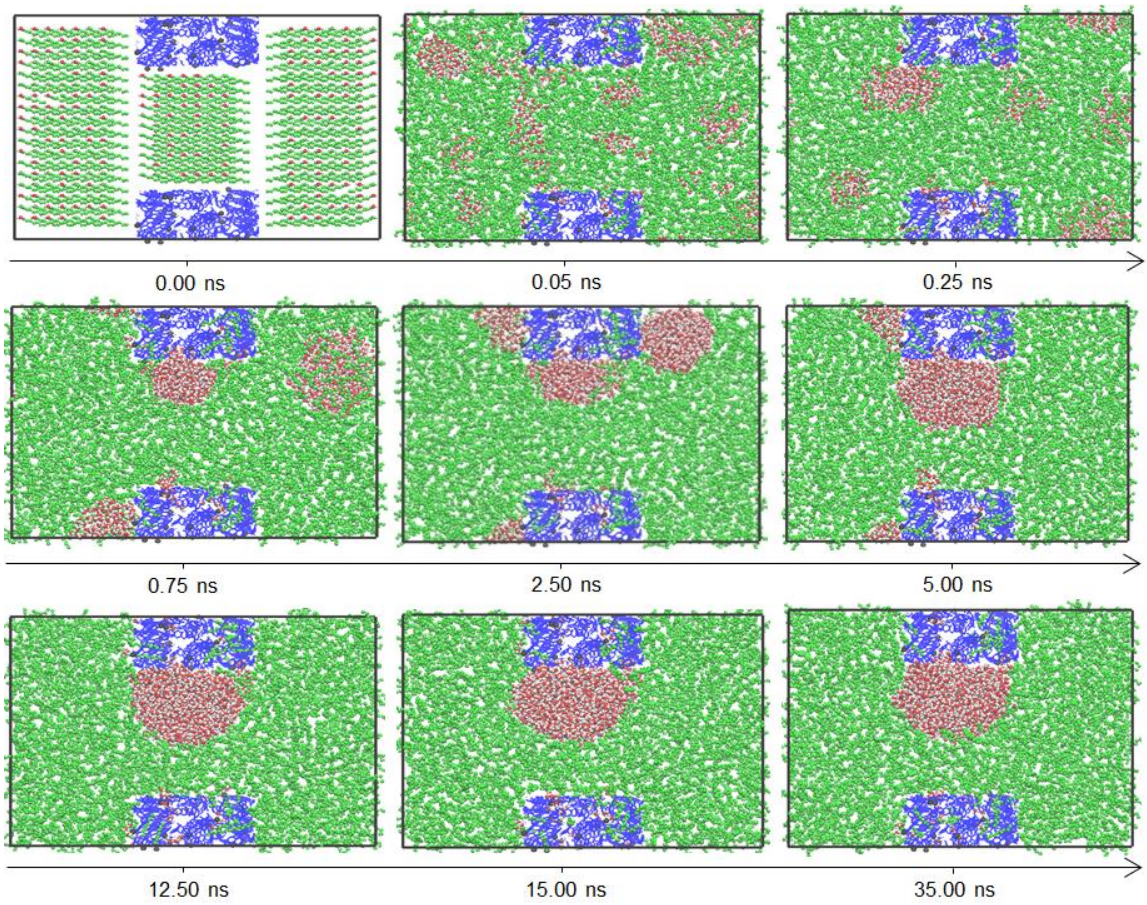

Figure 7.2: Snapshots of the simulation process with time beginning with the initial configuration for the 5nm activated kerogen pore system

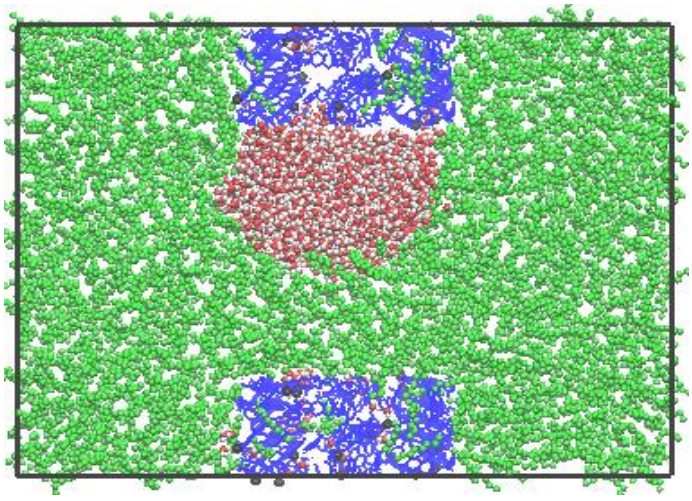

Figure 7.3: Final configuration of the 5nm activated kerogen pore system

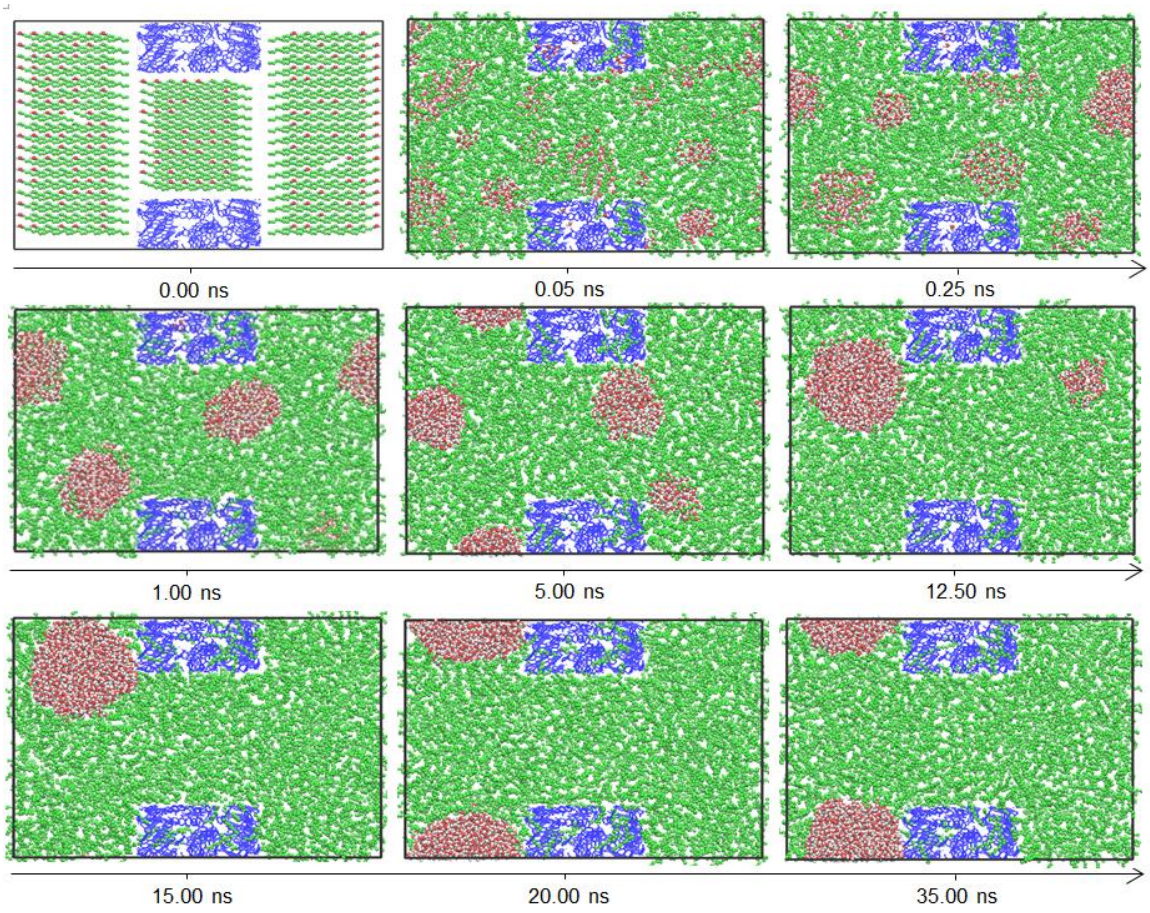

Figure 7.4: Snapshots of the simulation process with time beginning with the initial configuration for the 5nm inactivated kerogen pore system

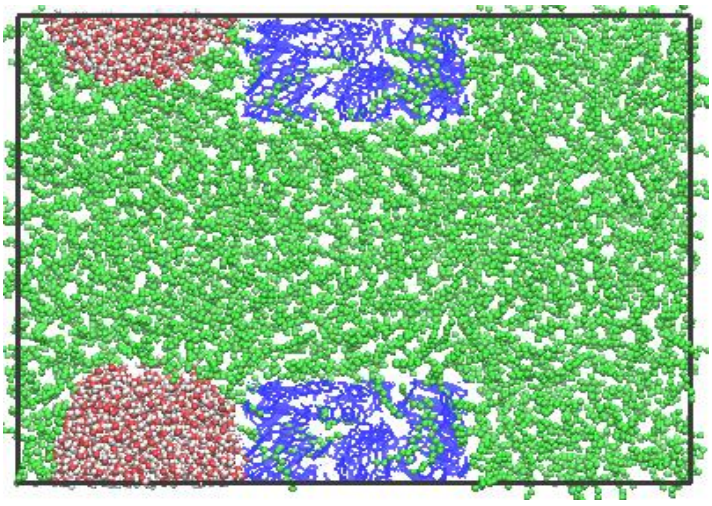

Figure 7.5: Final configuration of the 5nm inactivated kerogen pore system

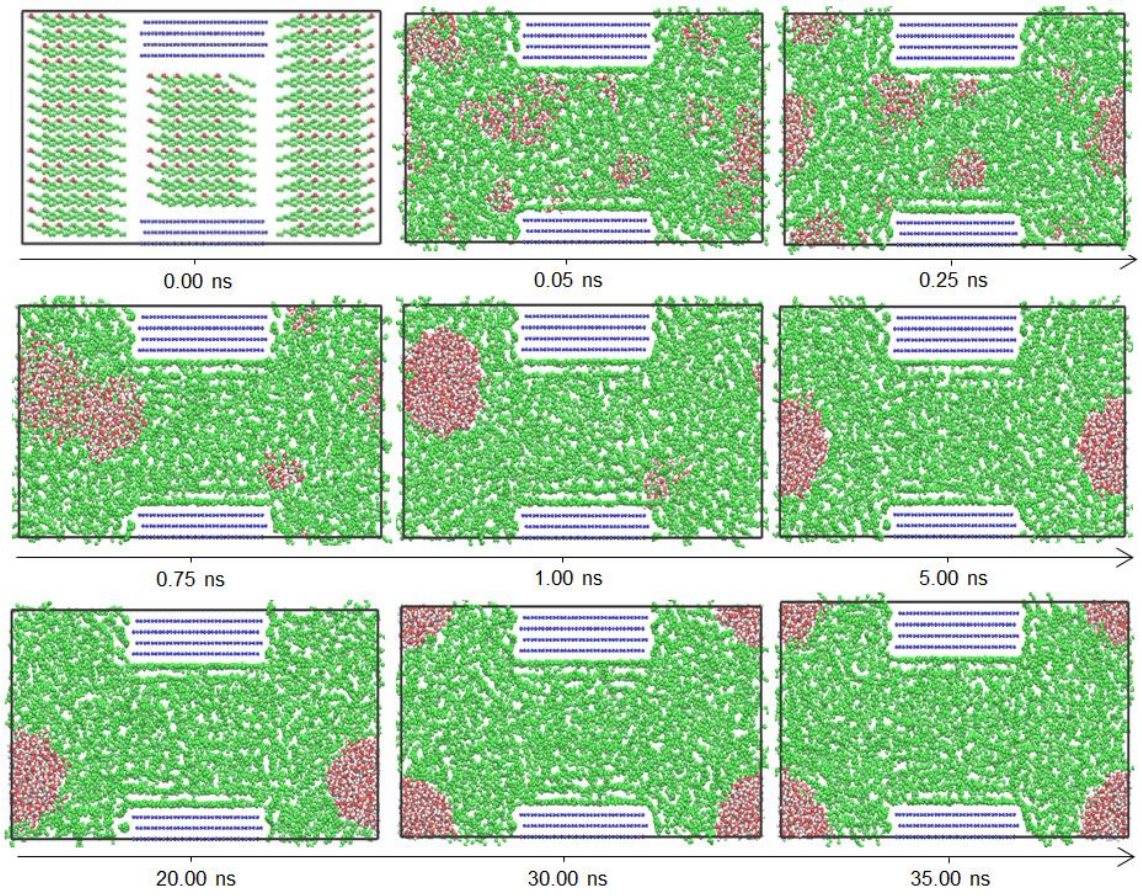

Figure 7.6: Snapshots of the simulation process with time beginning with the initial configuration for the 5nm graphite slit pore system

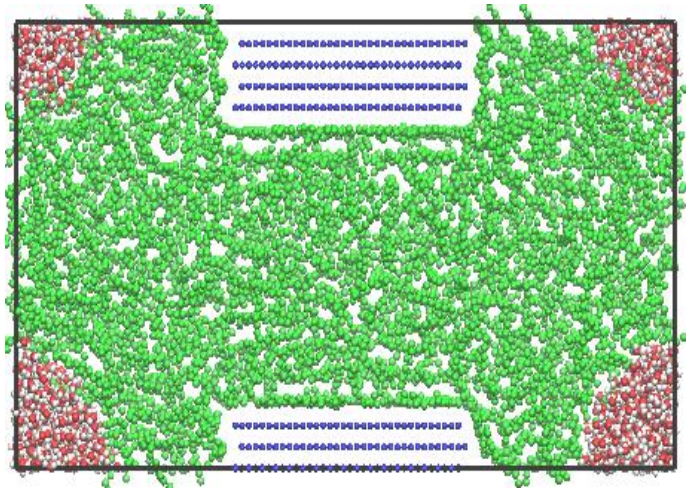

Figure 7.7: Final configuration of the 5nm graphite slit pore system

7.2.1 Behavior of Water: Formation of Water Clusters

Hu et al. (2013a, 2013b) discussed the behavior of water in organic nanopores in the absence of any hydrocarbon and report that water completely fills large kerogen pores irrespective of the level of activation and can potentially be adsorbed on the pore surfaces. In this study, water forms large clusters in the presence of octane irrespective of the pore surface geometry or chemistry as shown in Figures 7.2-7.7. The clustering mechanism occurs because water molecules are polarized and have a strong tendency of forming hydrogen bonds with each other in the absence of a stronger interaction between water and other particles. This also governs the formation of a round or drop-shape water aggregation as the exposed hydrogen bonds on other non-polar materials are minimized and the hydrogen bonds with other water molecules are maximized. This can have the following implication: during re-stimulation following a period of depletion or during the soaking phase of hydraulic fracturing operations, water may enter in to kerogen pores and micro-cracks. This may be especially important for shales of intermediate maturity such as those found in liquids-rich shale plays (Jarvie 2012a). The multiphase distributions within the activated kerogen pore in Figures 7.2 and 7.3 can lead to the formation of water trapping or water blocks, modified relative permeability curves and hydrocarbon storage curves.

7.2.2 Potential Wettability Alternation Due to Surface Activation

The key difference between the activated pore models and the inactivated pore models is that the location of the water clusters when octane is also present is strongly linked to the

presence of the activated functional groups in kerogen. For the activated pores seen in Figure 7.2 and 7.3, clusters of water are formed within the pore. For the inactivated pore systems in Figures 7.4-7.7, the water clusters preferentially remain in the regions exterior to the pore. These results indicate that the presence of surface functional groups may cause a wettability alteration from hydrophobic or octane-wetting to heterogeneous wettability. It is clear that octane and water occupy the pore simultaneously in Figure 7.3, in contrast with observations in Figure 7.5 and 7.7 where the pores are largely octane-wetting.

In Figure 7.3, there is a fairly large water cluster whose diameter is comparable to the pore length. The reason for the cluster clinging to the upper activated kerogen body is due to the presence of several extruding surface oxygen atoms in the top kerogen body which allows water clusters to easily form "bridges" between active sites and thereby attract more water molecules. Hence, the amount of water in the cluster and the contact angle of the interface are likely to depend on the local density of the surface oxygen on the kerogen bodies. With a more realistic O/C atomic ratio, more water molecules may be attracted to the activated kerogen pores. Trapping of fracture water in shales of intermediate maturity may therefore be a result of trapping in organic pores in addition to the well-known phenomenon of adsorption in inorganic clay minerals (King 2012).

7.2.3 Presence of Octane and Water in the Kerogen Body

The uptake of octane and water by the kerogen bodies is also seen to be a function of surface activation. The activated model in Figures 7.2 and 7.3 captures some water and octane molecules adsorbed within the kerogen body with the water molecules restricted

to the activated functional groups. The inactivated kerogen model in Figures 7.4 and 7.5 on the other hand only allows octane and restricts the entry of water in to the pore body. For the graphite slit pores in Figures 7.6 and 7.7, both water and octane are absent in the kerogen body. The number of particles stored within top and bottom kerogen bodies and within the pores for different systems is tabulated in Table 7.3. Since calculations are averaged over the last 7.5 ns, the particle numbers in the tables are not integers. The table shows significantly more water molecules and a slight-to-moderate decrease in the amount of octane in activated kerogen pores than in the inactivated ones. The presence of water within the activated kerogen body may block some of the nano-cracks in the kerogen body and restrict the entry of octane while also reducing the surface area available for octane adsorption. This effect in porous activated carbons was also observed in Brennan et al. (2002). Together with the water entrapment in activated kerogen pores, the presence of water within the kerogen body clearly indicates the heterogeneous wettability of kerogen and supports experimental observations of water content in organic material (Chalmers and Bustin 2010, Ruppert et al. 2013). Water uptake and alkane storage are therefore likely to be controlled by proportion of hydrophobic to hydrophilic sorption sites throughout the kerogen.

Table 7.3: Average number of molecules in various 5 nm kerogen pores

Number of molecules		Activated kerogen pore	Inactivated kerogen pore	Graphite slit pore
Top kerogen body	Water	35.19	0.35	N/A
	Octane	10.58	15.54	N/A
Bottom kerogen body	Water	28.30	0.81	N/A
	Octane	12.70	15.02	N/A
Pore	Water	1100.08	0.01	0.01
	Octane	144.45	278.79	270.73

7.2.4 Dependence of Adsorption Characteristics on Surface Roughness

In the graphite slit pore system of Figure 7.7, a distinct adsorbed octane layer is formed in the vicinity of the pore surface, while this high-density adsorbed layer is not observed in both the activated and inactivated kerogen models. This is likely due to the pore surface roughness and the differences in the carbon density in the kerogen and graphite models.

The density in number of molecules per angstrom3 for water and octane are correspondingly shown in Figures 7.8 to 7.10. The calculations for density are obtained by counting numbers of particles based on the center of mass in vertical bins of width 0.1 Å averaged over the last 7.5 ns. The figures demonstrate a layering effect for octane in all pores with varying density values which depend on the strength of the octane-wall interaction. Also, because of the existence of water clusters within the activated kerogen

pores, the calculated octane density profiles are not symmetric. The slightly lower density intensity of the first octane layer in the activated kerogen pore than that in the inactivated kerogen pore is a result of the presence of polarized groups in the activated kerogen which attracts water molecules to accumulate near the kerogen body, as water competes with octane for adsorption. The key difference between the various case studies is associated with adsorption. For the graphite system as seen in Figure 7.10, the density of the first octane layer close to the pore wall is significantly larger than that of the second layer which is consistent with the observation of the final configurations seen in Figure 7.7. These well-defined alkane layers have also been reported in Severson and Snurr (2007), Diaz-Campos (2010) and Didar (2012).

By contrast, for the activated and inactivated kerogen models, octane molecules are more evenly distributed in the pores, resulting in much smaller ratios between the intensities of high and low density peaks near the walls. Surface roughness therefore plays a considerable role in dictating fluid distributions. Surface roughness in the kerogen leads to the use of fewer carbon atoms than in the graphite slit pore model which further impacts the strength of the near-wall potentials. The much lower carbon densities in the kerogen models tend to weaken the effective Lennard-Jones potential between octane molecules and the pores resulting in less prominent octane layers close to the pore walls and a more uniform density profile across the width of the pore. Moreover, rough pore wall surfaces cause changes to the orientation of octane molecules whereas in a graphite pore system, octane molecules can align themselves parallel to the pore wall.

In Diaz-Campos (2010), the effect of multilayer adsorption was ignored in pores larger than 2nm because of the high intensity of the first adsorbed layer of methane, when

planar graphite slit pores were used. Consequently, a Langmuir model for adsorption (Langmuir, 1916) was considered to be appropriate for slit pore systems in Diaz-Campos (2010). Although this work is an exploratory analysis of multiphase fluid distributions in organic nanopores, pore surface roughness is seen to cause multiple layer adsorptions with comparable peak intensities. The study of alkane adsorption in realistic organic shale nanopores therefore merits more attention as indicated by the results presented in this study. In any case, the use of planar graphite model to generalize storage in organic nanopores is likely to be inadequate.

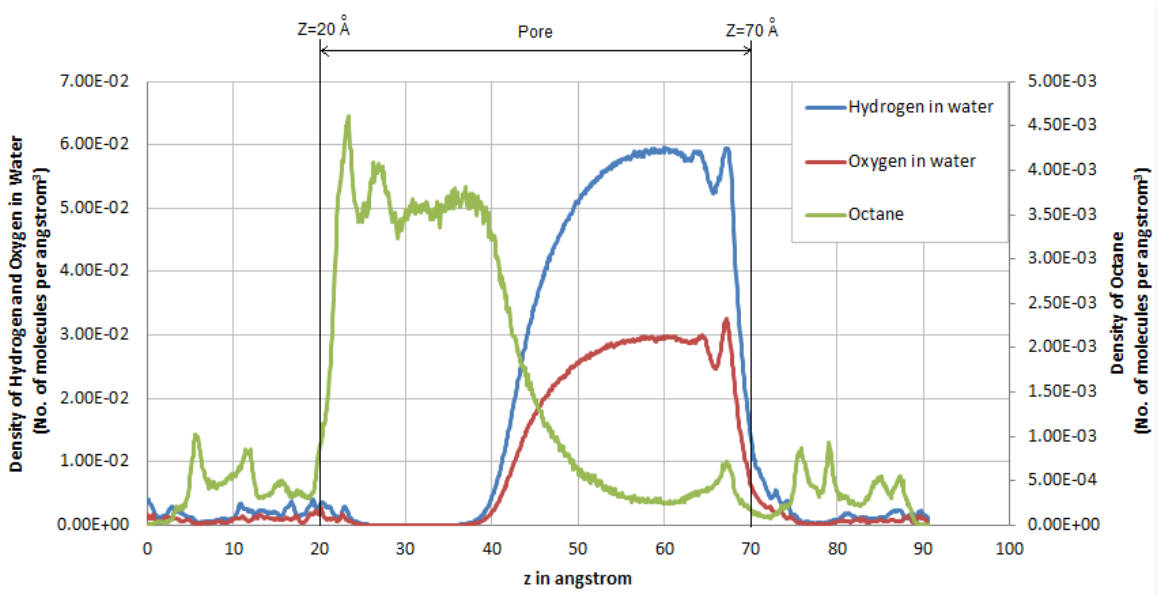

Figure 7.8: Density profiles for oxygen and hydrogen atoms of water, and octane molecules versus vertical length for the 5nm activated kerogen pore

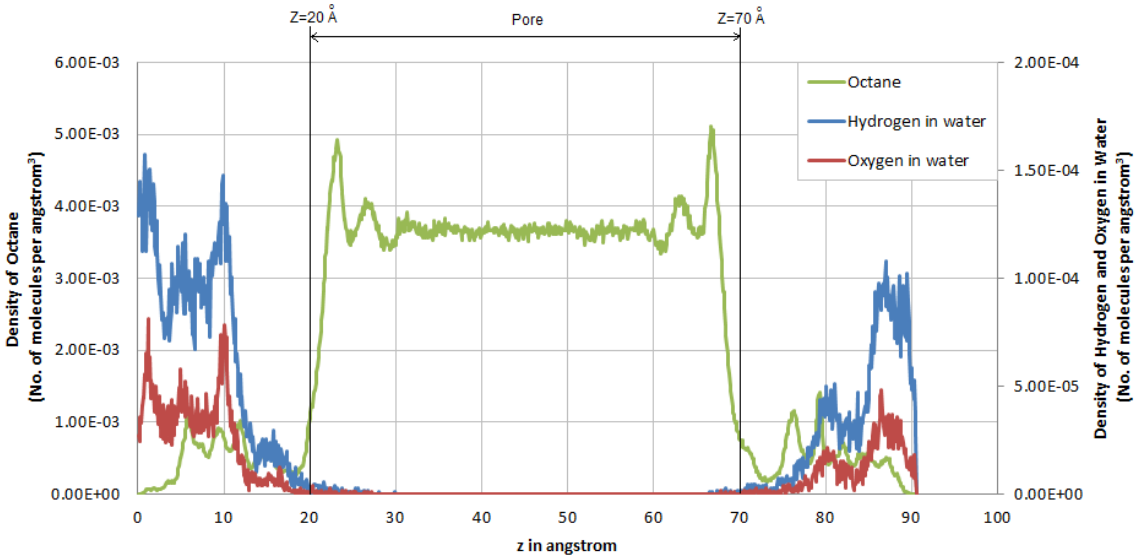

Figure 7.9: Density profiles for oxygen and hydrogen atoms of water, and octane molecules versus vertical length for the 5nm inactivated kerogen pore

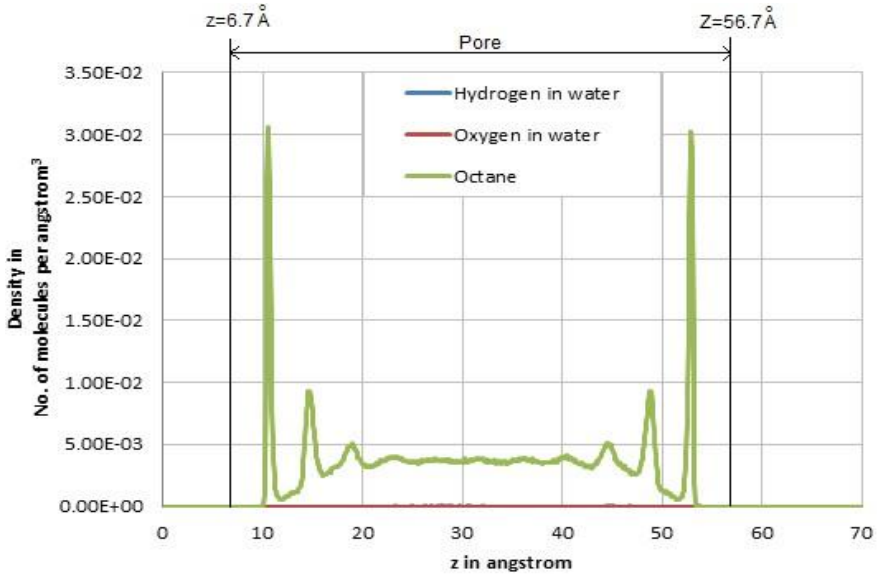

Figure 7.10: Density profiles for oxygen and hydrogen atoms of water, and octane molecules versus vertical length for the 5nm smooth graphite slit pore

7.3 Conclusion

This chapter reports the behavior of water and octane molecules confined in three kerogen pores with the same 5 nm pore widths: an activated kerogen pore where surfaces have been partly oxidized with a small O/C ratio, an inactivated kerogen pore without any surface activation, and the popular graphite slit pore. In all cases, water molecules are seen to aggregate together to form clusters due to the polarity of water, when alkanes are present. The distribution of octane within these pores is also seen to be a function of surface roughness and the presence of activated sites. The key observations of this study can be summarized as the following:

1. Surface morphology of the pores significantly alters the dynamics of water and octane inside the pores. With oxygenated functionalized groups within the kerogen body, water molecules favorably stay inside the pore due to surface activation. In contrast, water molecules accumulate outside of non-polarized pores when the inactivated kerogen model and the graphite slit pore are used.

2. Surface roughness may influence the fluid-pore wall interaction. As a result, the octane adsorption in the kerogen pores is more evenly and smoothly distributed, while an appreciable octane mono-layer is seen in graphite slit pores.

3. Surface activation changes the surface property from hydrophobic to heterogeneous-wetting. Significantly more water molecules are captured in nano-cracks within the activated kerogen bodies than that within the pure carbon bodies.

4. The distribution of both polar (water) and non-polar (alkanes) molecules within the pore is a function of surface roughness, the presence of activated sites and pore size.

CHAPTER 8

CONCLUSIONS AND PRACTICAL SIGNIFICANCE

This chapter provides conclusions drawn from the results presented in previous chapters. The study investigated the surface wettability effect of kerogen in Chapter 4 where the dynamics of various fluids are shown to be influenced by kerogen maturation on the confined pores of the constructed simplified kerogen models. The fluids considered in this thesis include pure water in Chapter 5, brine in Chapter 6 and a mixture of water and hydrocarbon in Chapter 7.

The proposed simplified kerogen models go beyond the conventional graphene slit pore systems and incorporate structural features that mimic kerogen pore systems including heterogeneous wettability, surface roughness, tortuous paths and material disorder. The activated kerogen model contains surface oxidized functional groups and is built to represent kerogen from shales of intermediate maturity as observed in shale oil plays. The carbon-only inactivated kerogen model containing no oxygenated sites represents highly mature shales found in shale gas plays. By comparing the results of these kerogen models with a traditional kerogen proxy of a graphitic slit-shaped pore, the role of kerogen maturity in fluid distribution is studied and the impact of maturity level on wettability in organic pores is revealed.

Some of the key findings from this work are provided below:

1. The results indicate the need for moving beyond planar graphite slit-pore systems towards more sophisticated kerogen pore systems when attempting to quantify fluid thermodynamic properties in shales. With the same pore width, the distribution of

both polar (water) and non-polar (octane) molecules within the pore is a function of surface roughness, the porous nature, and the presence of activated sites etc.

2. Surface morphology of the pores strongly influences the behavior of fluids, the effective pore width and the strength of fluid-pore surface interactions. These create conditions for different mechanisms of fluid entrapment, differing amounts of adsorption and uptake of fluids by the organic material.

3. Adsorption characteristics of organic pores are significantly influenced by the surface roughness. Uniformly distributed alkanes are observed within the pore, implying multilayer adsorption. In reality, the Langmuir monolayer adsorption model may be inadequate to quantify fluid storage.

4. The presence of micro-cracks and functional groups within kerogen creates a potential for storage of water, ions and alkanes within the body of kerogen itself and may serve as an additional storage mechanism in addition to free and adsorbed phases.

5. Kerogen maturity levels have impact on its wettability. The presence of functional groups within kerogen may change its wetting characteristics from hydrophobic to heterogeneous-wetting.

6. It is possible that there exists a critical density of surface functionalized sites beyond which the kerogen pore system could be considered to be completely water-wet. When surfaces contain higher density amounts than the threshold, water forms sheets adjacent to the surfaces.

The thesis offers several results of practical significance.

First, the results indicate that kerogen of intermediate maturity such as those in oil shales (Jarvie 2012b) may be heterogeneous-wetting. This is in contrast to the reported

observations in Passey et al. (2010) which suggests that organics are largely hydrophobic. Since the wettability issue is directly related to multiphase flow modeling, fluid saturation profiles and hydrocarbon-in-place estimation, this study motivates further investigation in to the lab- and reservoir-scale impact of kerogen thermal maturity levels on its wettability.

Secondly, there may also be pore filling effects causing water entrapment in small pores depending on the level of organic maturity which may be a mechanism for trapping of hydraulic fracture water. The amount of water trapped will likely be a function of organic pore connectivity, organic pore size distribution, the number of activated sites and the amount of organics in shales.

Thirdly, the results from the graphite slit pore model show strong monolayer adsorption characteristics for alkanes. However, adsorption characteristics of kerogen may need to be carefully interpreted in the presence of significant surface roughness. In reality, the storage of alkanes within kerogen may be in between the results obtained for the graphite slit pore and the kerogen models chosen in this study. Storage experiments in shales indicate some adsorptive effects (Sigal et al. 2013). Nevertheless, the graphite slit pores are likely to be representative of the micro-cracks found in kerogen (Ousseini 2012) while the kerogen pore models considered in this work are more representative of the pores observed in SEM images of kerogen-rich shales (Curtis et al. 2013).

Recommended future research may be categorized into three areas. First, the impact of other functionalized groups such as epoxy, carboxyl, hydroxyl embedded in kerogen material on fluid behavior and distribution is merited. Additionally, a study of multi-component hydrocarbons may be necessary and their interplay with water

molecules when confined in nano-sized organic pores would provide us a better idea about the wettability and water entrapment in shale kerogen. Lastly, the influence of temperature and pressure on the contact angles is also recommended to better characterize kerogen wettability.

REFERENCES

Alcañiz-Monge J., Linares-Solano A., and Rand B. 2002. Mechanism of Adsorption of Water in Carbon Micropores as Revealed by a Study of Activated Carbon Fibers. J Phys Chem B. Vol. 106, No. 12, pp.3209–16.

Akkutlu, I.Y., Fathi, E., 2012. Multiscale Gas Transport in Shales With Local Kerogen Heterogeneities. SPE-146422. SPE Journal. Vol. 17, pp. 1002 - 1011.

Alder, B.J. and Wainwright, T.E. 1957. Phase Transition for a Hard Sphere System. The Journal of Chemical Physics. Vol. 27, No. 5, pp. 1208-1209.

Ambrose, R.J. 2011. Micro-Structure of Gas Shales and its Effects on Gas Storage and Production Performance. Ph.D Thesis, University of Oklahoma, Norman, OK.

Bagri, A., Grantab, R., Medhekar, N.V., and Shenoy, V. B. 2010. Stability and Formation Mechanisms of Carbonyl- and Hydroxyl-Decorated Holes in Graphene Oxide. J. Phys. Chem. C. Vol. 114, No.28, pp 12053–12061.

Behar, F., Vandenbroucke, M., 1987. Chemical modelling of Kerogens. Organic Geochemistry. Vol. 11, pp. 15–24.

Berendsen, H. J. C., Grigera , J. R., and Straatsma, T. P. 1987. The Missing Term in Effective Pair Potentials. The Journal of Physical Chemistry. Vol. 91, No. 24, pp. 6269–6271.

Brennan, J.K, Thomson, K.T., and Gubbins, K.E. 2002. Adsorption of Water in Activated Carbons: Effects of Pore Blocking and Connectivity. Langmuir. Vol. 18, pp.5438-5447.

Cailliez F., Trzpit M., Soulard M., Demachy I., Boutin A., Patarin J., et al. 2008. Thermodynamics of Water Intrusion in Nanoporous Hydrophobic Solids. Phys Chem Chem Phys. Vol. 10, No. 32, pp. 4817–26.

Chalmers, G.R., and Bustin, M.R. 2010. The Effects and Distribution of Moisture in Gas Shale Reservoir Systems. Poster presentation at AAPG Annual Convention and Exhibition, Louisiana, New Orleans, USA.

Chalmers, G.R., Bustin, M.R., and Power, I.M. 2012. Characterization of Gas Shale Pore Systems by Porosimetry, Pycnometry, Surface Area, and Field Emission Scanning Electron Microscopy/Transmission Electron Microscopy Image Analyses: Examples from the Barnett, Woodford, Haynesville, Marcellus, and Doig Units. AAPG Bulletin. Vol. 96, No. 6, pp. 1099–1119.

Chen, J.H., Mehmani, A., Li, B.Y., Georgi, D., and Jin, G. 2013. Estimation of Total Hydrocarbon in the Presence of Capillary Condensation for Unconventional Shale Reservoirs. Paper SPE 164468 presented at the SPE Middle East Oil and Gas Show and Exhibition, Manama, Bahrain.

Cheng, A. and Steele, W. A. 1990. Computer Simulation of Ammonia on Graphite. I. Low Temperature Structure of Monolayer and Bilayer films. Journal of Chemical Physics. Vol. 92, pp. 3858.

Chialvo, A.A, and Cummings, P.T. 2011. Aqua Ions-Graphene Interfacial and Confinement Behavior: Insights from Isobaric-Isothermal Molecular Dynamics. The Journal of Physical Chemistry A. Vol. 115, pp. 5918-5927.

Cipolla, C.L., Lolon, E., Erdle, J., and Tathed, V.S. 2009. Modeling Well Performance in Shale-Gas Reservoirs. Paper SPE 125532 presented at the SPE/EAGE Reservoir Characterization and simulation Conference, AbuDhabi, UAE, 19-21 October.

Cole, D.R., Striolo, A., and Phan, A. 2013. Hydrocarbon Behavior at Nanoscale Interfaces, in 'Carbon in the Earth'. Reviews in Mineralogy and Geochemistry, R.M. Hazen, R.J. Hemley, A. Jones, and J. Barross Editors. In Press.

Crain, E.R. 2010. Crain's Petrophysical Handbook. Rocky Mountain House, AB : Spectrum 2000 Mindware.

Curtis, M.E., Ambrose, R.J., Sondergeld, C.H., and Rai, C.S. 2010. Structural Characterization of Gas Shales on the Micro- and Nano-Scales. Paper SPE 137693 presented at Canadian Unconventional Resources and International Petroleum Conference, Calgary, Alberta, Canada.

Curtis, M.E., Ambrose, R.J., Sondergeld, C.H., and Rai, C.S. 2011. Transmission and Scanning Electron Microscopy Investigation of Pore Connectivity of Gas Shales on the Nanoscale. Paper SPE 144391 presented at North American Unconventional Gas Conference and Exhibition, Woodlands, Texas, USA.

Cygan, R.T., Liang, J.J., and Kalinichew, A.G. 2004. Molecular Models of Hydroxide, Oxyhydroxide, and Clay Phases and the Development of a General Force Field. J. Phys. Chem. B. Vol. 108, pp. 1255.

Dang, L.X. 1995. Mechanism and Thermodynamics of Ion Selectivity in Aqueous Solutions of 18-Crown-6 Ether: A Molecular Dynamics Study. J. Am. Chem. Soc. Vol. 117, pp. 6954-6960.

Devegowda, D., Sapmanee, K., Civan, F. and Sigal, R.F. 2012. Phase Behavior of Gas Condensates in Shales Due to Pore Proximity Effects: Implications for Transport, Reserves and Well Productivity. Paper SPE 160099 presented in SPE Annual Technical Conference and Exhibition, San Antonio, Texas.

Diaz-Campos, M. 2010. Uncertainties in Shale Gas-in-Place Calculations: Molecular Simulation Approach. Master's Thesis, University of Oklahoma, Norman, OK.

Didar, B. 2012. Multi-Component Shale Gas-in-Place Calculations. Master's Thesis, University of Oklahoma, Norman, OK.

Elijah O. 2011. An NMR study of shale wettability. Master's Thesis, University of Oklahoma, Norman, OK.

Energy Information Administration, June 2013. Technically Recoverable Shale Oil and Shale Gas Resources: An Assessment of 137 Shale Formations in 41 Countries Outside the United States.

Energy Information Administration, April 2013. Annual Energy Outlook 2010 with Projections to 2040.

Facelli, J.C., Pugmire, R.J., Pimienta, I.S., Badu, S. and Orendt, A.M. 2011. Atomistic Modeling of Oil-Shale Kerogens and Asphaltenes along with their Interactions with the Inorganic Material Matrix. Department of Energy Topical Report,http://repository.icse.utah.edu/dspace/bitstream/123456789/11076/1/icse_atomistic_modeling_topical_report.pdf.

Fathi, E., Tinni, A., and Akkutlu, I.Y. 2012. Shale Gas Correction to Klinkenberg Slip Theory. Paper SPE 154977 presented at SPE Americas Unconventional Resources Conference, Pittsburgh, Pennsylvania USA.

Fine, R.A, and Millero, F.J. 1973. Compressibility of Water as a Function of Temperature and Pressure. J. Chem. Phys. Vol 59, pp. 5529.

Firincioglu, T. 2013. Bubble Point Suppression in Unconventional Liquids Rich Reservoirs and Its Impact on Oil Production. PhD Dissertation, Colorado School of Mines, Golden, Colorado.

Giovambattista, N., Rossky, P.J. and Debenedetti, P.G. 2007. Effect of Pressure on the Phase Behavior and Structure of Water Confined between Nanoscale Hydrophobic and Hydrophilic Plates. J. Phys. Chem. C. Vol.111, pp.1323–32.

Harrison, A., Cracknell, R. F., Krueger-Venus, J., and Sarkisov, L. 2013. Branched Versus Linear Alkane Adsorption in Carbonaceous Slit Pores. Adsorption. doi:10.1007/s10450-013-9589-1.

Hess, B., Kutzner, C., van der Spoel, D., Lindahl, E. 2008. GROMACS 4: Algorithms for Highly Efficient, Load-Balanced, and Scalable Molecular Simulation. J. Chem. Theory Comp. Vol.4, pp.435–447.

Hu, Y., Devegowda, D., Striolo, A., Ho, T. A., Phan, Anh., Civan, F., and Sigal, R. F. 2013a. A Pore Scale Study Describing the Dynamics of Slickwater Distribution in Shale Gas Formations Following Hydraulic Fracturing. Paper SPE 164552 presented at SPE Unconventional Resources Conference, Woodland, Houston, USA.

Hu, Y., Devegowda, D., Striolo, A., Phan, Anh., Ho, T. A., Civan, F., and Sigal, R. F. 2013b. A Pore Scale Study of Slickwater Systems in Shale Reservoirs: Implications for Frac-Water Distribution and Produced Water Salinity. Paper SPE 168762 presented at Unconventional Resources Technology Conference, Denver, Colorado, USA.

Hu, Y., Devegowda, D., Striolo, A., Civan, F., and Sigal, R. F. 2013c. Microscopic Dynamics of Water and Hydrocarbon in Shale-Kerogen Pores of Potentially Mixed-Wettability. Paper SPE 167234 presented at SPE Unconventional Resources Conference - Canada, Alberta, Canada.

Hu, Y., Devegowda, D., Striolo, A., Phan, A.T.V, Ho, T.A., Civan, F., and Sigal, R. F. 2014a. Microscopic Dynamics of Water and Hydrocarbon in Shale-Kerogen Pores of Potentially Mixed Wettability. Paper SPE 167234, SPEJ, accepted for publication.

Hu, Y., Devegowda, D., Striolo, A., Phan, Anh., Ho, T. A., Civan, F., and Sigal, R. F. 2014b. The dynamics of hydraulic fracture water confined in nano-pores in shale reservoirs. Journal of Unconventional Oil and Gas Resources. Vol. 9, pp. 31–39.

Jarvie, D. M., 2012a, Shale Resource Systems for Oil and Gas: Part 1—Shale-gas Resource Systems, in J. A. Breyer, ed., Shale reservoirs—Giant resources for the 21st century: AAPG Memoir 97, p. 69–87.

Jarvie, D. M., 2012b, Shale Resource Systems for Oil and Gas: Part 2—Shale-Oil Resource Systems, in J. A. Breyer, ed., Shale reservoirs—Giant resources for the 21st century: AAPG Memoir 97, p. 89–119.

Jiang, J., Sandler, S.I., and Smit, B., 2004. Capillary Phase Transitions of n-Alkanes in a Carbon Nanotube. Nano Letters. Vol. 4, No. 2, pp. 241-244.

Kalluri, R.K., Konatham, D., and Striolo, A. 2011. Aqueous NaCl Solutions within Charged Carbon-Slit Pores: Partition Coefficients and Density Distributions from Molecular Dynamics Simulations. The Journal of Physical Chemistry. Vol. 115, pp. 13786-13795.

Kaneko K., Hanzawa Y., Iiyama T., Kanda T., and Suzuki T. 1999. Cluster-mediated water adsorption on carbon nanopores. Adsorption. Vol. 5, pp. 7 - 13.

Kimura T., Kanoh H., Kanda T., Ohkubo T., Hattori Y., Higaonna Y., et al. 2004. Cluster- Associated Filling of Water in Hydrophobic Carbon Micropores. J Phys Chem B. Vol. 108, No. 37, pp.14043–8.

King, G.E. 2010. Thirty Years of Gas Shale Fracturing: What Have We Learned? Paper SPE 133456 presented at the SPE Annual Technical Conference and Exhibition, Florence, Italy, 19-22 September.

King, G.E. 2012. Hydraulic Fracturing 101: What Every Representative, Environmentalist, Regulator, Reporter, Investor, University Researcher, Neighbor and Engineer Should Know About Estimating Frac Risk and Improving Frac Performance in Unconventional Gas and Oil Wells. Paper SPE 152596 presented at the SPE Hydraulic Fracturing Technology Conference, Woodlands, 6-8 February.

Kondratyuk, P., Wang, Y., Karl Johnson, J., and John T. Yates , Jr. 2005. Observation of a One -Dimensional Adsorption Site on Carbon Nanotubes: Adsorption of Alkanes of Different Molecular Lengths. J. Phys. Chem. B. Vol. 109, pp.20999-21005.

Langmuir, I. 1916. The Constitution and Fundamental Properties of Solids and Liquids. Part I. Solids. J. Am. Chem. Soc. Vol 38, pp. 2221-2295.

Lemmon, E.W., McLinden, M.O. and Friend, D.G. 2005. Thermophysical Properties of Fluid Systems. In NIST Chemistry WebBook, NIST Standard Reference Database Number 69, (Linstrom, P.J.,, and Mallard, W.G., eds.). online http://webbook.nist.gov.

Li, B., Mehmani A., Chen, J., Georgi, D., and Jin, G. 2013. The Condition of Capillary Condensation and Its Effects on Adsorption Isotherms of Unconventional Gas Condensate Reservoirs. Paper SPE 166162 presented at the SPE Annual Technical Conference and Exhibition, New Orleans, Louisiana, USA.

Liu, Y., and Wilcox, J. 2012. Effects of Surface Heterogeneity on the Adsorption of CO_2 in Microporous Carbons. Environmental Science and Technology. Vol. 46, pp. 1940 - 1947.

Martin, M.G., and Siepmann, J.I. 1998. Transferable Potentials for Phase Equilibria. 1. United-Atom Description of n-Alkanes. J. Phys. Chem. B. Vol.102, pp. 2569-2577.

McCarthy, K., Rojas, K., Niemann, M., Palmowski, D., Peters, K., and Stankiewicz, A. 2011. Basic Petroleum Geochemistry for Source Rock Evaluation. Oilfield review summer. Vol. 23, pp. 32 – 43.

Müller, E.A, and Hung, F.R. 2000. Adsorption of Water Vapor-Methane Mixtures on Activated Carbons. Langmuir. Vol. 16, pp. 5418-5424.

Ohba, T., Kanoh H., and Kaneko K. 2005. Water Cluster Growth in Hydrophobic Solid Nanospaces. Chem – A Eur J. Vol.11, No.17, pp. 4890–4.

Osborne, K.L. 2009. Temperature-Dependence of the Contact Angle of Water on Graphite, Silicon, and Gold. Master's Thesis, Worcester Polytechnic Institute, Worcester, Massachusetts.

Palmer, J.C, and Gubbins, K.E. 2012. Atomistic Models for Disordered Nanoporous Carbons Using Reactive Force Fields. Microporous and mesoporous materials. Vol. 154, pp 24-37.

Palisch, T.T., Vincent, M.C., and Handren, P.J. 2008. Slickwater Fracturing – Food for Thought. Paper SPE 115766 presented at the SPE Annual Technical Conference and Exhibition, Denver, 21-24 September.

Passey, Q.R., Bohacs, K.M., Esch, W.L., Klimentidis, R., and Sinha S. 2010. From Oil-Prone Source Rock to Gas-Producing Shale Reservoir - Geologic and Petrophysical Characterization of Unconventional Shale Gas Reservoirs. Paper SPE 131350

presented at International Oil and Gas Conference and Exhibition in China, Beijing, China.

Peters, E.J. 2012. Advanced Petrophysics: Volume 1: Geology, Porosity, Absolute Permeability, Heterogeneity, and Geostatistics, first ed. Live Oak Book Company, Texas, US.

Phan, A., Ho, T.A., and Striolo, A. 2012. Molecular Structure and Dynamics in Thin Water Films at Metal Oxide Surfaces: Magnesium, Aluminum, and Silicon Oxide Surfaces. The journal of Physical Chemistry C. vol 116, pp. 15962-15973.

Qin, B. 2007. Numerical study of Recovery Mechanisms in Tight Gas Reservoirs. Master's Thesis, University of Oklahoma, Norman, OK.

Rullko¨tter, J., and Michaelis, W. 1990. The Structure of Kerogen and Related Materials. A Review of Recent Progress and Future Trends. Advances in Organic Geochemisry. Vol. 16, pp. 829-852.

Ruppert, L.F., Sakurovs, R., Blach, T.P., He, L. Melnichenko, Y.B., Mildner, D.F. and Alcantar-Lopez, L. 2013. A USANS/SANS Study of the Accessibility of Pores in the Barnett Shale to Methane and Water. Energy Fuels. Vol. 27, pp. 772-779.

Sapmanee K. 2011. Effects of Pore Proximity on Behavior and Production Prediction of Gas/Condensate. Master's Thesis, University of Oklahoma, Norman, OK.

Schein, G. 2005. The Application and Technology of Slickwater Fracturing. Paper SPE 108807 presented as a Distinguished Lecture during the 2004- 2005 season.

Scocchi, G., Sergi, D., D'Angelo, C., and Ortona, A. 2011. Wetting and contact-line effects for spherical and cylindrical droplets on graphene layers:A comparative molecular-dynamics investigation. Physical Review E. Vol.84, pp. 061602.

Severson, B.L., ad Snurr, R.Q. 2007. Monte Carlo Simulation of n-Alkane Adsorption Isotherms in Carbon Slit Pores. J. Chem. Phys. Vol. 126, pp. 134708.

Shih, C. J., Wang, Q. H., Lin, S., Park, K. C., Jin, Z., Strano, M.S.,and Blankschtein, D. Breakdown in the wetting transparency of graphene. Phys. Rev. Lett. 2012, 109, 176101.

Sigal, R.F. 2013. The Effects of Gas Adsorption on Storage and Transport of Methane in Organic Shales, Accepted for publication in Petrophysics.

Sondergeld, C.H., Ambrose, R.J., Rai, C.S., and Moncrieff, J. 2010. Micro-Structural Studies of Gas Shales. Paper SPE 131771 presented at SPE Unconventional Gas Conference, Pittsburgh, Pennsylvania, USA.

Sondhi, N. 2011. Petrophysical characterization of Eagle Ford Shale. Master's Thesis, University of Oklahoma, Norman, OK.

Steele, W.A. The Interaction of Gases with Solid Surfaces. Pergamon Press: Oxford, 1974.

Striolo, A., and Chialvo, A.A, Cummings, P.T and Gubbins, K.E. 2003. Water Adsorption in Carbon-Slit Nanopores. Langmuir. Vol. 19, pp. 8583-8591.

Striolo, A. 2007. Water Self-Diffusion Through Narrow Oxygenated Carbon Nanotubes. Nanotechnology. Vol. 18, pp. 475704-475714.

Striolo. A. 2011. From Interfacial Water to Macroscopic Observables: A Review. Adsorption Science and Technology. Vol, 29, pp. 211-258.

Taherian, F., Marcon, V., and van der Vegt N. F. A. 2013. What Is the Contact Angle of Water on Graphene? Langmuir. Vol. 29,

Tenney, C.M., and Lastoskie, C.M. 2006. Molecular Simulation of Carbon Dioxide Adsorption in Chemically and Structurally Heterogeneous Porous Carbons. Environmental Progress. Vol. 25, No.4, pp. 343-354.

Tissot, B.P., Welte, D.H., 1978. Petroleum Formation and Occurrence, first ed. Springer Verlag, Berlin.

Travalloni, L., Castier, M., and Tavares, F.W. 2014. Phase Equilibrium of Fluids Confined in Porous Media from an Extended Peng-Robinson Equation of State. Fluid Phase Equilibria. Vol. 362. pp. 335-341.

Vandenbroucke, M., Bordenave, M.L., Durand, B., 1993. Transformation of organic matter with increasing burial of sediments and the formation of petroleum in source rocks. In: Bordenave, M.L. (Ed.), Applied Petroleum Geochemistry. Editions Technip, Paris, pp. 101–122.

Vandenbroucke, M., and Largeau, C. 2007. Kerogen Origins, Evolution and Structure. Organic Geochemistry. Vol. 38, pp 719-833.

van der Spoel, D., Lindahl, E., Hess, B., Groenhof, G., Mark, A. E., and Berendsen, H. J. C. 2005. GROMACS: Fast, Flexible and Free. J. Comp. Chem. Vol.26, pp1701–1718.

Vega, C., McBride, C., Sanz, E., and Abascal, J.L.F. 2005. Radial Distribution Functions and Densities for the SPC/E, TIP4P and TIP5P Models for Liquid Water and Ices Ih, Ic, II, III, IV, V, VI, VII, VIII, IX, XI and XII. Phys. Chem. Chem. Phys. Vol. 7, pp. 1450-1456.

Vega C. and Abascal, J.L.F. 2011. Simulating Water with Rigid Non-Polarizable Models: A General Perspective. Phys. Chem. Chem. Phys. Vol. 13, pp. 19663–19688.

Warpinski, N.R., Kramm, R.C., Heinze, J.R., and Waltman, C.K. 2005. Comparison of Single- and Dual-Array Microseismic Mapping Techniques in the Barnett Shale. Paper

SPE 95568 presented at the SPE Annual Technical Conference and Exhibition, Dallas, 9-12 October.

Werder, T., Walther, J. H., Jaffe, R. L., Halicioglu, T., and Koumoutsakos, P. 2003. On the Water-Carbon Interaction for Use in Molecular Dynamics Simulations of Graphite and Carbon Nanotubes. J. Phys. Chem. B. Vol.107 No.6, pp 1345–1352.

Xiong, X., Devegowda, D., Michel, G.G., Sigal, R.F., and Civan, F. 2012. A Fully-Coupled Free and Adsorptive Phase Transport Model for Shale Gas Reservoirs Including Non-Darcy Flow Effects. Paper SPE 159758 presented at SPE Annual Technical Conference and Exhibition, San Antonio, Texas, USA.

NOMENCLATURE

a_i	acceleration of atom i
c_i	constant
C_{pore}	ionic concentration in the pore
C_{bulk}	ionic concentration in the bulk
F_i	force acting on atom i
k_θ	force constant
m_i	mass of atom i
N	number of particles
q_i	partial charge of atom i
q_j	partial charge of atom j
r_i	intermolecular distance
t	Time
U_{angle}	bond angle bending potential
U_B	bonded energy
U_{bond}	bond stretching potential
U_{el}	electrostatic potential
U_i	potential energy of atom i
U_{NB}	nonbonded energy
U_{total}	total energy
$U_{dihedral}$	dihedral potential
U_{VW}	12-6 Lennard-Jones (LJ) potential

Γ	partition coefficient
ε	potential well depth
ϵ_0	permittivity of free space
σ	distance of zero intermolecular potential
ϕ	current dihedral angle
θ	current bond angle
θ_0	equilibrium bond angle

APPENDIX A

DETERMINATION OF SYSTEM EQUILIBIRUM

To ensure the effectiveness of the simulation results, stable systems are required and the state of equilibrium must be checked. In this study, two criteria are applied in each case to make sure the systems have been stabilized.

The first one is to re-run the system using initial configurations where the arrangement of particles is significantly different from the previous starting points and the expected results. Because the simulation results do not depend on the initial configurations, a different initial configuration should generate equivalent final results when the true equilibrium state is reached. For example, for the study of water distribution in the 0.9 nm inactivated kerogen pore, in addition to the initial arrangement described in Section 5.1, another initial profile with water fully penetrating all sizes of the pores is studied as well. This configuration is illustrated in Figure A.1. As simulation progresses, water molecules escape from the 0.9 nm inactivated kerogen pore, generating a final simulation configuration consistent with the results in Figure 5.2a in Chapter 5. Another example is given for the study of water and octane mixture in the inactivated kerogen pore. Instead of arranging water and octane randomly across the simulation box, a new initial arrangement is studied with water molecules inside the pore and octane placed outside of it, as Figure A.2 shows. After 90 ns simulation time, water clusters are formed outside of the studied pore and the final configuration is the same as Figure 7.5.

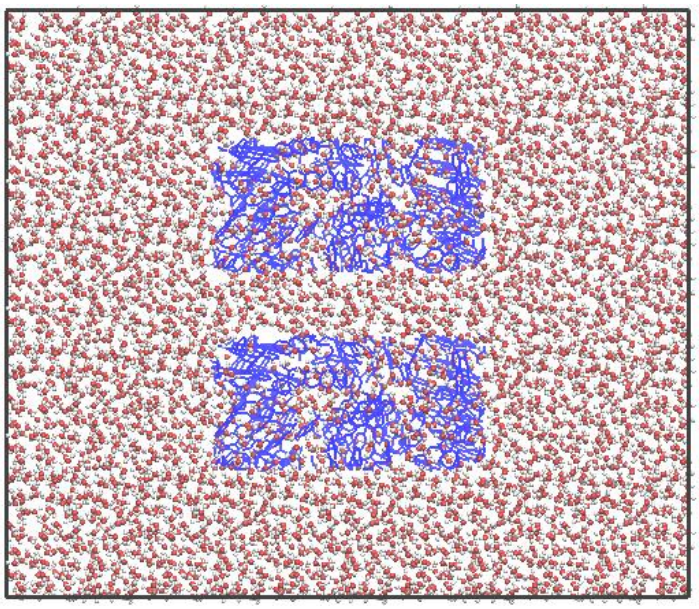

Figure A.1: Different initial configuration studied for the case of water molecules in 0.9 nm inactivated kerogen pore

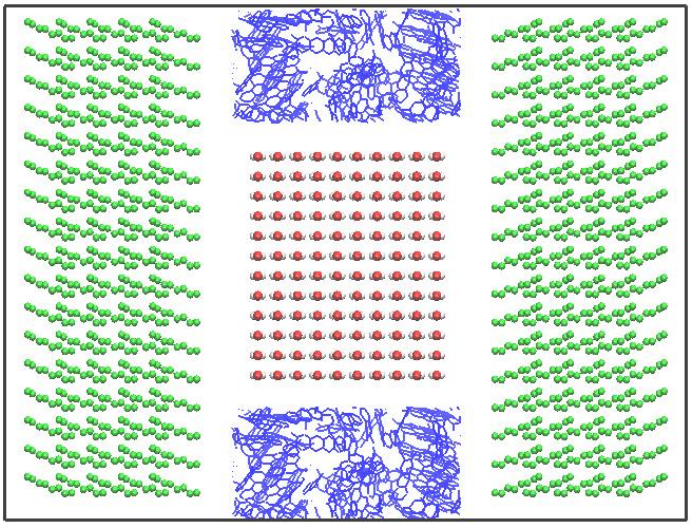

Figure A.2: Different initial configuration studied for the case of water and octane mixture in inactivated kerogen pore

Another criterion is to make sure that values of temperature, energy, average pressure, number of particles, average density profiles, and bulk properties, are constant when system equilibrium is reached. The study of pure water in 1.2 nm activated kerogen

pore is used as an example to determine the equilibrium state. In this case, a total of 50 ns NVT is run after controlling pressure. These 50 ns duration is separated into 5 pieces with 10 ns in each. Figure A.3 shows the temperature and the moving average of the values versus simulation time for the final 10 ns. Figure A.4 is the pressure and its moving average for the last 10 ns simulation. From Figure A.3 and A.4, the average temperature and pressure are maintained at controlled values, 300 K and 200 bar. Figure A.5 is energy quantities as the last 10 ns simulation progresses, and the values are constant with time. Numbers of molecules in the last consecutive 30 ns are also compared with each other and are illustrated in Table A.1, to ensure that molecule amounts are constant for each 10 ns. Density profiles for every 10 ns duration are also compared regarding the shape and intensities of high and low peak. Finally, bulk water densities in regions far from the pore surfaces are compared with experimentally obtained bulk water densities. Kalluri et al. (2011) report a strong influence of the pore wall on the fluids up to a distance of 1-1.5 nm from the pore wall. We therefore define the bulk region as the volume outside the pore located more than 1.5 nm away from the kerogen bodies. When the system is stable, the influence of the pore wall on the properties of fluid in the bulk regions is negligible and hence this region is meant to replicate the bulk properties. The water density in the units of g/cm^3 in the bulk region is calculated to be 0.997 which compares well with the experimental result of 1.005 at the 300K and 200 bar conditions (Fine et al. 1973).

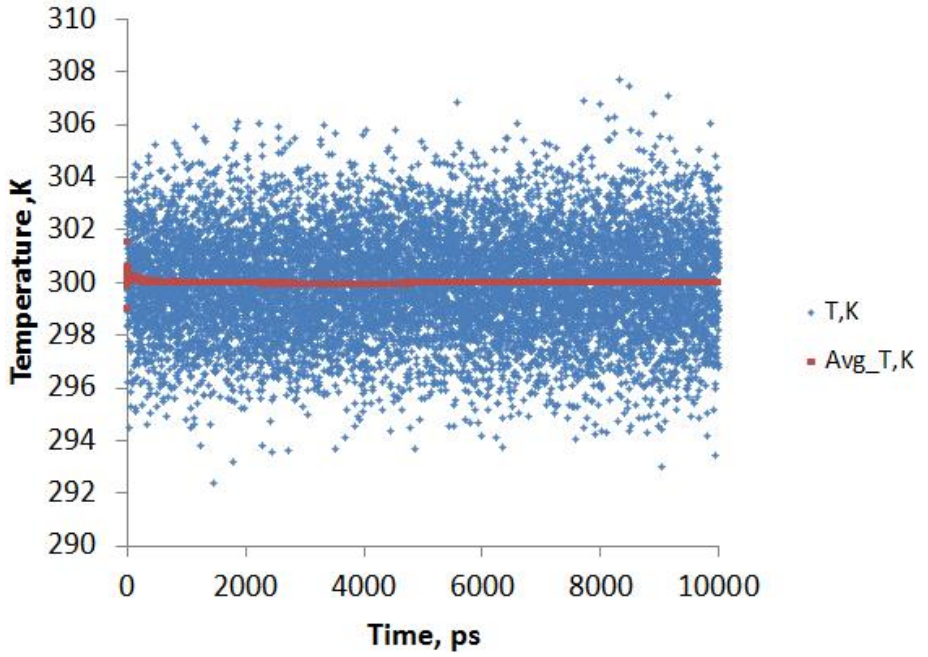

Figure A.3: Temperature versus simulation time for the case of pure water in the 1.2 nm activated kerogen pore

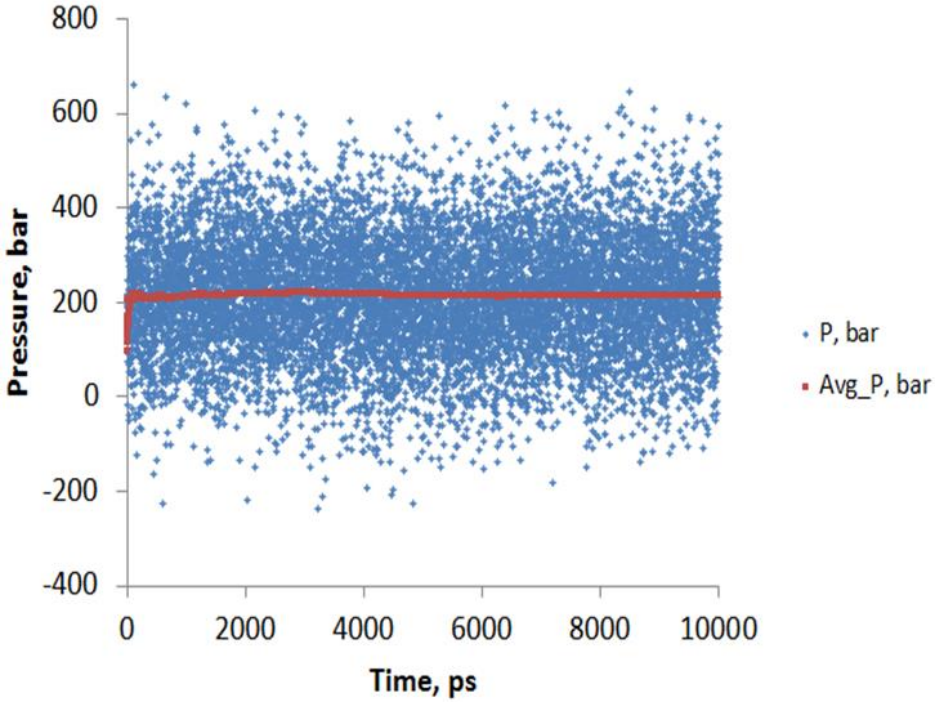

Figure A.4: Pressure versus simulation time for the case of pure water in the 1.2 nm activated kerogen pore

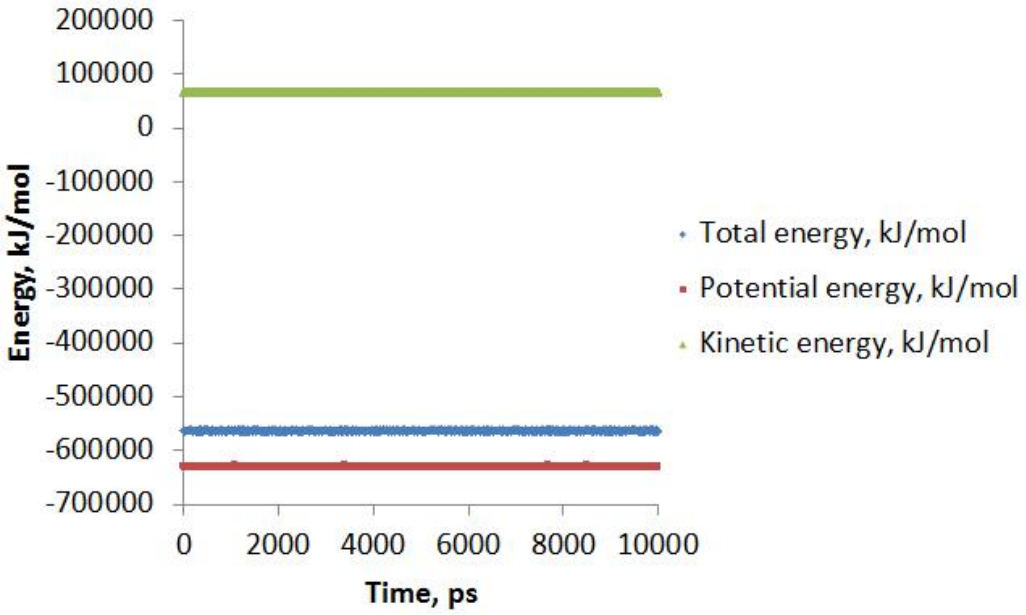

Figure A.5: Energy versus simulation time for the case of pure water in the 1.2 nm activated kerogen pore

Table A.1: Numbers of molecules in the last consecutive 30 ns

	Water in Pore	Water in top Kerogen	Water in bottom Kerogen
10 ns	555.71	94.60	93.80
10 ns	553.97	95.16	94.31
10 ns	554.29	93.22	92.10

APPENDIX B

USING ELLIPSE FITTING TO DETERMINE CONTACT ANGLE

In this appendix B, instead of using circular function to fit the data, ellipse is utilized for curve fitting. The ellipse equation is $\frac{(x-p)^2}{a^2} + \frac{(y-q)^2}{b^2} = 1$, where a and b are the radius along the x and y axes respectively, and the coordinate (p, q) is the ellipse's center. For our problem, the center of the ellipse is located either in the x or y axis.

There may be many ellipses that all fit the original data, as the solutions may be generated from locally optimized objective functions. So instead of plotting the ellipse and the original data, a plot of $(x-p)^2$ versus $(y-q)^2$ provides a better visualization for the accuracy of the ellipse fitting. If these squared points fit a linear trend with a R^2 value close to 1, the optimized parameters are desirable for this problem. Figure B.1 is the plot of $(x-p)^2$ versus $(y-q)^2$ for the study of pure water droplet on graphene surface and the fitting performance is satisfactory. The next issue is to determine the location of the tangent line. As Figure 4.5a demonstrated, there is a space gap between the surface and the liquid, because of the molecular expulsion. To determine the location of the tangent line, two points are selected in the density isochore profile and contact angles are reported for each. Figure B.2 shows the selection of these two points where tangent lines are determined correspondingly. Point A is the intersection of the fitting ellipse and the solid surface. Point B is located at z = 3 Å in the fitted ellipse, as z = 3 Å is the bottommost value of the liquid in Figure 4.5a. The calculated contact angles corresponding to each tangent line are reported in Table B.1. From this table, point B generates more reasonable value, compared to the values in literatures.

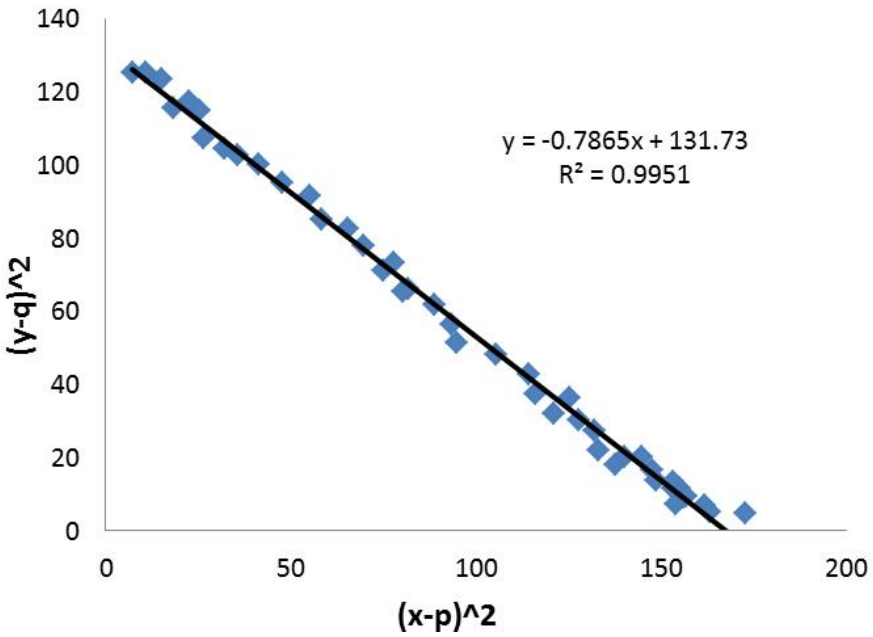

Figure B.1: Plot of $(x-p)^2$ versus $(y-q)^2$ for the study of pure water droplet on graphene surface

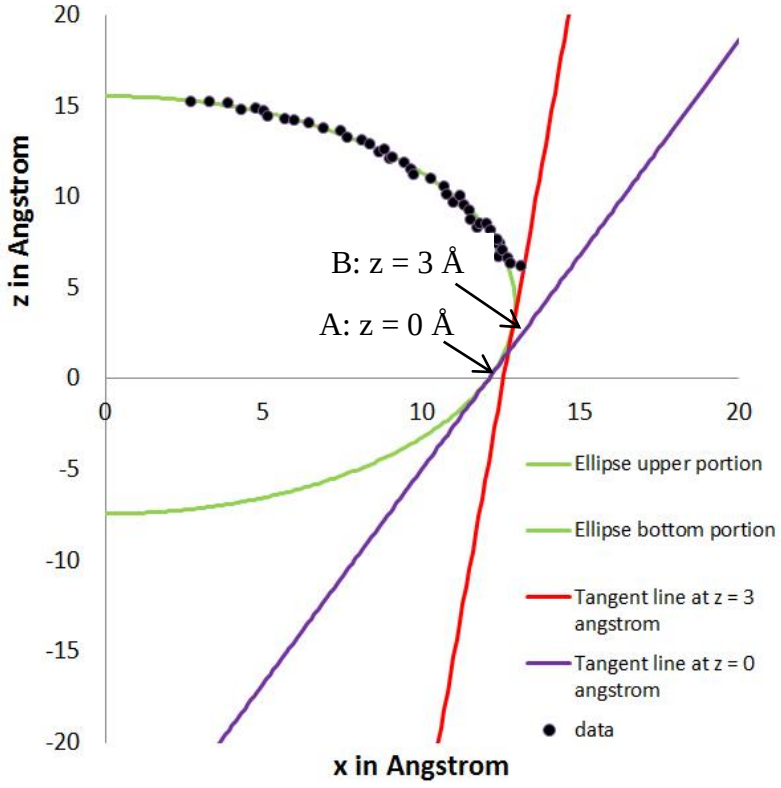

Figure B.2: Selections of tangent lines for the study of pure water droplet on graphene surface

Table B.1: Contact angles corresponding to tangent lines for the study of pure water droplet on graphene surface using ellipse fitting

	Point A	Point B
Contact angle θ, degree	113.01	95.89

Other data points from studies of an octane and water mixture on various kerogen surfaces in Section 4.4 are also fitted using ellipse function and contact angles are recalculated. Figure B.3 is the plot of $(x-p)^2$ versus $(y-q)^2$ and the parameters a, b, p, and q are optimized. The contact angle for each simulation study is provided in Table B.2. Even though for some cases, the values of contact angle are influenced by the selecting of the fitting curve, the general conclusion in Chapter 4 still holds, as we observe the decrease of contact angles with the increase of the amount of surface activated sites.

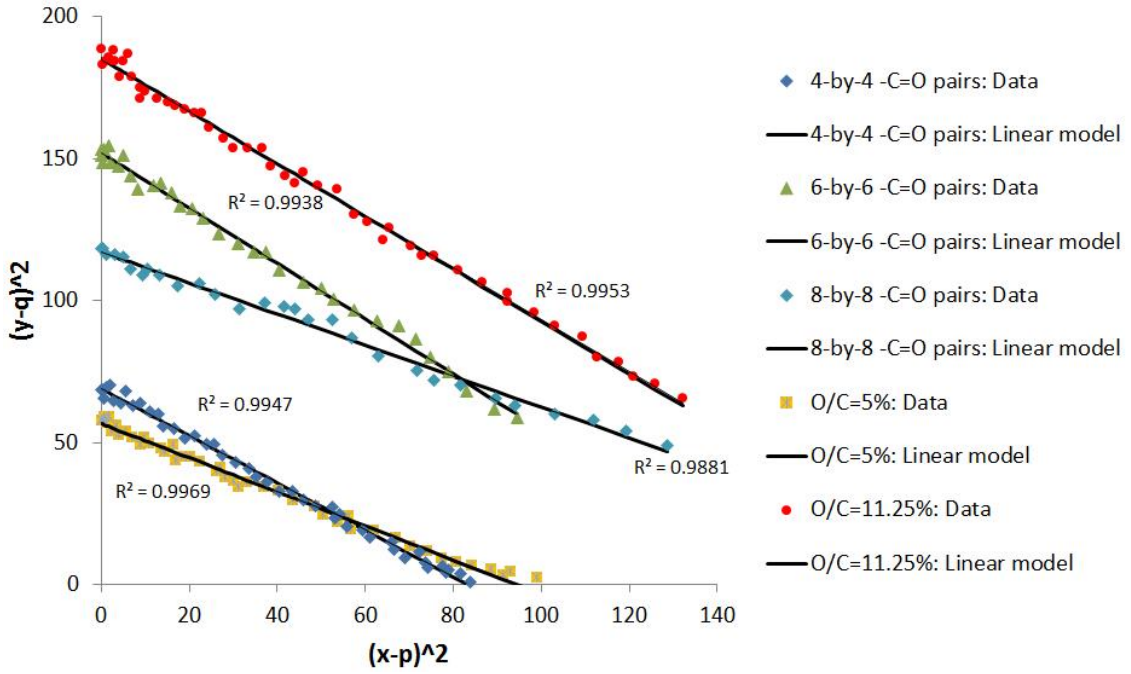

Figure B.3: Plot of $(x-p)^2$ versus $(y-q)^2$ for studies of a mixture of octane and water on various kerogen surfaces

Table B.2: Contact angles determined by ellipse fitting for studies of a mixture of octane and water on various kerogen surfaces

	Kerogen models with uniformly distributed carbonyl pairs			Kerogen models with heterogeneous distributed carbonyl pairs		
	4-by-4 -C=O pairs	6-by-6 -C=O pairs	8-by-8 -C=O pairs	O/C = 5%	O/C = 11.25%	O/C = 20%
O/C ratios, %	5%	11.25%	20%	5%	11.25%	20%
Contact angle θ, degree	149.99°	82.58°	68.66°	145.2°	76.79°	0°

APPENDIX C

THE INFLUENCE OF TEMPERATURE ON CONTACT ANGLE

The contact angles have been reported to be influenced by temperature (Osborne 2009). In this appendix, the study of an octane and water mixture on the uniformly distributed kerogen surfaces is extended. The initial system setup and simulation procedures are the same as described in Section 4.4.1, except that the temperature here is maintained at 350 K. The studied surface included 4-by-4, 6-by-6, and 8-by-8 –C=O pairs kerogen models. The final configurations are similar to Figure 4.8c-e. The contact angles are calculated based on circular fitting. Contact angles obtained from T=350 K are compared with results in T = 300 K in Section 4.4.2, and are summarized in Table C.1. For the kerogen surface with 4-by-4 –C=O pairs, the increase of temperature leads to a decreased contact angle. For the other two cases where the amounts of surface oxygenated groups are larger, there are no significant changes to the wettability. This issue needs further investigation to make a conclusion.

Table C.1: Contact angles for T = 350 K and T = 300 K for the study of a mixture of water and octane on uniformly distributed –C=O kerogen surfaces

	T=300K	T=350K
4-by-4 -C=O pairs	180°	141.35°
6-by-6 -C=O pairs	92.18°	90.06°
8-by-8 -C=O pairs	71.12°	70.53°